University Of Crete, Department of materials science & technology

Master's Thesis

A. Mimidis

Ultrashort-pulse laser fabrication of biomimetic metallic surfaces

Κατασκευή Βιομιμητικών επιφανειών με υπερβραχείς παλμούς laser

Supervisors: Dr. Stratakis Emmanuel, Prof. Kioseoglou George

December 2016

Abstract

The aim of this thesis is the experimental investigation of structuring metallic surfaces with linearly polarized Gaussian femtosecond laser pulses, in order to achieve controllable surface modification. Steel samples were irradiated with a focused ultra-short laser pulses and the morphology was studied as a function of fluence and number of pulses. Laser Induced Surface Structures (LIPSS) were structured on the sample surfaces following irradiation with tunable micro periodicity. A complete study was conducted investigating LIPPS periodicity as a function of wavelength, fluence angle of incidence and number of pulses. Furthermore large areas were fabricated with laser scanning method achieving each type of morphology observed for every type of steel. This work was conducted by irradiating samples a) in air and b) immersed in water, comparing results. Finally, wetting properties of the surfaces were investigated with i) water droplets ii) oil droplets and compared to the flat surface showing an increase in both water repellency and slight oil repellency.

Table Of Contents

Introduction

Over the past several years, there have been many reports of laser generated self-assembled structures on metals [1–4], semiconductors [5, 1–3], dielectrics [93–95], polymers [6, 7] and ceramics [92], hence the characterization of these structures as a universal phenomenon is valid. Although, the generation and evolution of these structures is still vividly and controversially discussed, the complete physical mechanism of this extraordinary phenomenon has yet to be completely elaborated.

Surface texturing in metals has been reported using nano second Nd:YAG and excimer lasers [8, 9], and picosecond Nd:YAG and sub-picosecond excimer lasers [8]. However, the structures formed by these lasers do not exhibit well-defined features. Recently, femtosecond lasers have become an advanced tool for material processing and have advantages over nano second lasers in terms of high precision, reduced heat-affected zone, and minimum burr formation [10].

The formation of *laser-induced periodic surface structures*, (LIPSS) also known as *ripples,* with a period approximately equal to the laser wavelength and aligned vertically to the laser polarization is well understood [11]. A variety of timescale-dependent processes are triggered following ultra-short pulsed laser interaction with matter: **(a)** Carrier generation, **(b)** internal thermalization of free carriers, **(c)** carrier-lattice thermalization, **(d)** energy transport via carrier transport **(d)** thermal and surface modification. Repetitive irradiation of the target can generate self-assembled microstructures (grooves, spikes) [12] which can be attributed to non-uniform thermalization after irradiation [13, 14] or hydrodynamic instabilities of molten material that follows irradiation [15].

Material laser processing in the presence of water is often the preferred method of laser fabrication to the otherwise dry treatment in order to fulfill very specific technological applications [16, 17]. In most cases, the presence of water results in cleaner and more precise laser micromachining by removing ablation debris and hindering its redisposition back to the surface irradiated. Ultimately, the surface obtained during irradiation with the presence of water differs from that of dry treatment. Water as a propagation medium can give rise to phenomena like super-continuum generation, filamentation and optical breakdown, depending on the laser beam fluence, which have a shielding effect reducing the amount of energy reaching the target [18–20]. All these contribute to the different morphologies observed compared to the dry experiment.

Texturing surfaces to create micro/nano scale surface structures has remarkable technological importance [21–37, 8, 9]. These induced surface structures augment various properties essential to many areas of research and development, for instance:(a)Biomedical: improving cell growth and proliferation [21–27, 8, 9]; (b)Optical: improving light trapping properties [28]; (c)Surface characteristics: controlling surface wetting behavior for self-cleaning applications [29–31]; (d) Solar cells and light detection: broadening the spectrum of efficient light trapping and improving photo-responsivity [32–35]; (e) Field emission effect: improved electron emission due to high field at the tips of the microstructures [36]; (f)Tribology: fabricating surfaces with the desired tribological properties [37].

Wettability describes the spreading of a liquid on a surface. Wettability engineering is important in e.g. the automotive industry for water repellent windshields and paints [81], preventing fouling [82], and reducing friction in moving parts [83]. In the marine industry wettability engineering is applied to prevent fouling [84], in the electric power industry to prevent fouling on solar cells [85] Also, it is important in biology to prevent bacterial contamination [86, 87] and in the electronic [88] and chemical industries [89].

In this thesis we report the formation of micro/nanostructures in various types of steel of industrial importance. I have investigated in detail the dependence of micro/nanostructures on beam fluence, number of laser shots per spot and wavelength. This study was conducted by irradiating the samples a) in ambient air, b) submerged in deionized water. In both cases *laser-induced periodic surface structures* were observed in slightly different conditions. The formation mechanism of LIPPS is discussed for both air and water. Furthermore, large surfaces covered with LIPPS were fabricated with laser scanning technique and their wetting properties were characterized showing an increase in hydrophobicity and a slight increase in oleophobicity.

Chapter 1: Basic principles of laserlight-matter interactions

The moment a metallic surface is exposed to an ultrashort laser pulse, a sequence of processes take place [38]. The laser pulse is absorbed by electrons, leading to a rapid increase in their temperature during the laser pulse irradiation, while the lattice remains at the initial temperature prior to irradiation. The system is thus driven out of thermal equilibrium and is consisted now of two subsystems each at its individual temperature: electrons at the temperature of the order of one electron volt (~11000 T) and the lattice at the room temperature. The thermal equilibrium between the lattice and electrons is established on the picosecond time scale. If the energy of the laser pulse is sufficient, the surface melts and remains in the melted state for up to a nanosecond. After the resolidification, the self-organized patterns are frozen into the surface and can be observed. Although the basic physical processes at the laser ablation are well understood and moreover, the effect of the LIPSS formation is interesting as well for fundamental physics as for practical applications, the mechanisms of the pattern formation are still not completely clear.

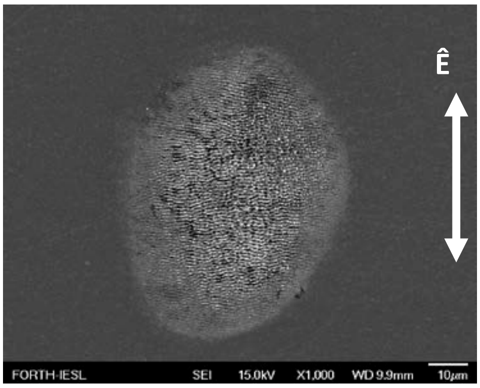

Figure 1: LIPPS (ripples) formed on the surface of stainless steel after irradiation with 5 fs pulses. Their orientation is perpendicular to the beam polarization.

There are two theoretical approaches, which try to explain the laser-induced periodic structures: (1) theories based on interference, i.e., a purely optical approach; (2) theories involving hydrodynamic instabilities, which result in self-organization effects. Patterns explained in frames of the optical theories are referred to as *coherent structures*, whereas patterns explained by hydrodynamic-like theories are referred to as *non-coherent structures* [39].

1.1.1 Electrodynamics

Emmony *et al.* suggested in 1973 that LIPSS were a consequence of interference between the incident laser beam and surface-scattered waves [40]. An interference model of the incident and the scattered surface waves, caused by surface roughness can explain the formation of LIPSS. The ripple wavelength Λ due to the proposed mechanism was assumed to be equal to:

$$\Lambda = \frac{\lambda}{1 \pm sin\theta} \tag{1}$$

Where, λ the laser wavelength and ϑ is the angle of the incidence laser beam. The ± accounts for the scattered wave co and counter propagating to the surface projection of the incident wave. For normal incidence, Eq.1 gives Λ ~ λ therefore such ripples are called wavelength, or ''Low-Spatial-Frequency-Ripples (LSFR)''.

Following this idea, Sipe *et al.* created the efficacy factor theory to account for LIPSS formation [11]. According to this theory surface roughness gives rise to a surface scattered wave which interferes with the laser beam. As a consequence, this leads to inhomogeneous absorption of energy on the target surface. Ripple formation is realized assuming that damage occurs first in regions where inhomogeneous absorption is largest. This can be quantified with the relation

$$A(\vec{k}) \propto \eta\left(\vec{k},\vec{k_\iota}\right)\left|b(\vec{k})\right| \tag{2}$$

Where η is called the efficacy factor and quantifies the efficacy with which the roughness leads to an inhomogeneous absorption at $\vec{k}$, while $b\left(\vec{k}\right)$ is the Fourier component of the roughness. Hence $\eta\left(\vec{k}\right)$ and $b\left(\vec{k}\right)$ are governing the formation of ripples. The efficacy factor theory has several drawbacks [41]. Inter-pulse changes in the $b\left(\vec{k}\right)$ function are not modeled, it is therefore impossible to use the efficacy factor theory on a pulse to pulse basis. Consequently, the only possible quantitative predictions are related to the steady state LIPSS, governed by the efficacy factor. Furthermore, this theory does not consider transient changes of the material properties during a laser pulse, and the influence of the pulse duration itself is not taken into account.

All approaches predicted ripple wavelengths in the order of the beam wavelength ($\Lambda \sim \lambda$). Although we can sufficiently explain the LSFR with the simple interference theory, it has been observed on a large number of experiments that ripple periodicity shows much smaller values than the initial laser wavelength ($\Lambda \ll \lambda$). These type of structures we call ''High Spatial Frequency Ripples (HSFR)'', while their formation is not considered in the frame of the η theory.

We present an improved and widely accepted mechanism that accounts for HSFR formation. The proposed mechanism is related with surface Plasmon waves, for the generation of ripples, as all metallic surfaces allow excitation of surface Plasmon waves. At the interface between a dielectric half space with positive real dielectric constant and an adjacent conducting half space of metallic character with a negative real dielectric constant, we can have wave solutions propagating confined at the interface of the two materials.

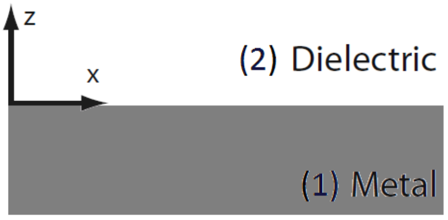

Figure 2: The interface between a conductor and a dielectric able to support SPP excitation.

Confinement implies an evanescent decay in the perpendicular direction. These waves are called surface Plasmon Polaritons (SPP) and are composed of electron density waves that oscillate on the metallic surface and the electric field in the dielectric. It can be exited during the material irradiation with incoming photons transferring their energy to SPP excitation. An SPP will propagate along the interface until its energy is lost either to absorption in the metal or scattering into other directions (such as into free space).

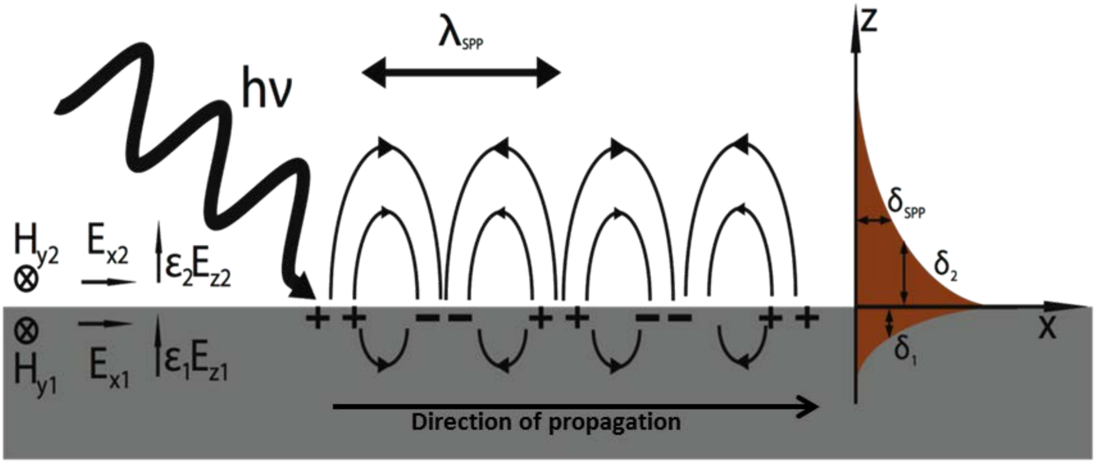

Figure 3: Illustration of the field components of an SPP supported by a metal–dielectric interface. Transverse magnetic electric field components are normal to the interface (z-axis) and along the propagation direction (x-axis). The mode profile (red) shows the exponentially dependent attenuation of the electromagnetic field intensity on the distance away from the interface is shown on the right.

The dispersion relation of the propagating SPP Is given by,

$$\lambda_s = \left(\frac{\varepsilon_1 + \varepsilon_2}{\varepsilon_1 \varepsilon_2}\right)^{1/2} \tag{3}$$

Where ε is the dielectric function (1 for metal, 2 for the dielectric).

It has to be noted that SPP propagation is allowed only for transverse magnetic (TM) polarization modes where only the field components E_x, E_z and H_y are non-zero.

According to this model SPP-laser interference occurs, giving rise to ripples with periodicity given by,

$$\Lambda = \frac{\lambda}{\frac{\lambda}{\lambda_s} \pm sin\theta} \tag{4}$$

Comparing this relation with Eq. 1, the formation of ripples with significantly higher periodicity can be predicted. Furthermore, the transverse magnetic characteristic of

SPP waves determines the polarization dependence of ripples we observe on the target.

Although it is known that a flat surface cannot excite SPP waves since there is a mismatch in wave vectors of SPP and incoming photons, we can have SPP excitation on corrugated surfaces produced after light-matter interaction via a mechanism known as *grating coupling*.

1.1.2 Excitation via Surface Morphology

In 1902 R. W. Wood observed drops in the optical spectrum produced by the diffraction grating, which he could not explain [42]. The positions of these drops depend on the incidence angle. This observation proves that Plasmons can be excited on a periodically patterned surface [43], e.g., on a diffraction grating. A coupling between the surface Plasmon wave and the incident light may also happen due to surface roughness (corrugation), when it's spectrum contains frequencies, at which the coupling is effective [39, 11, 44].

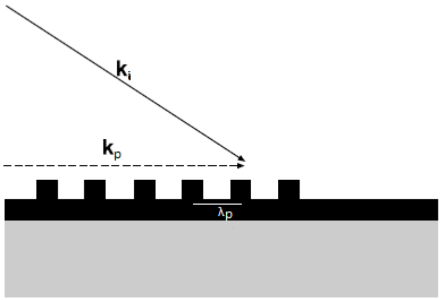

Figure 4: Grating coupling between incident laser beam with k-vectork_i *with in- plane k-vector* k_p*. Grating constant period is denoted as* λ_p*.*

This mismatch in wave vector between the in-plane (x direction) momentum $k_x = k \sin \theta$ of impinging photons and $k_s = \frac{2\pi}{\lambda_s}$ can also be overcome by patterning the metal surface with a shallow grating of grooves or holes with lattice constant λ_p. This simple one-dimensional grating of grooves induces phase matching if the condition $k_s = k_x + n\frac{2\pi}{\lambda_p}$ is fulfilled. Where $n = 1,2$ ....

1.2.1 Thermodynamics (two temperature model)

One of the most popular theoretical models to predict how heat flows from the exited electrons to the lattice, when it comes to ultrafast laser processing on a solid surface, is the *two temperature model* (TTM). TTM has been widely used with a lot of variations depending on the materials and the irradiation conditions to calculate the temperature variations between the electron and lattice subsystems [10, 45]. Due to the fact that the beam spot diameter typically varies from 10-100 µm, much greater than the optical-electron penetration depth (tens of nanometers) the energy transport into a metal can be described by the following one-dimensional two temperature diffusion model. Hence assuming that the electron thermalization is very fast and that the electron-lattice temperatures can be described by T_e and T_l.

Evolution of electron temperature in time

$$C_e \frac{\partial T_e}{\partial t} = -\frac{\partial Q(z)}{\partial z} - \gamma(T_e - T_l) + S \tag{5}$$

Evolution of lattice temperature in time

$$C_l \frac{\partial T_l}{\partial t} = \gamma(T_e - T_l) \tag{6}$$

Heat flux

$$Q(z) = -k_e \frac{\partial T_e}{\partial z} \tag{7}$$

Laser heating source

$$S = I(t)Aae^{-az} \tag{8}$$

Where z axis is always perpendicular to the target surface, $Q(z)$ the heat flux, S is the laser heating source. $I(t)$ Is the laser intensity, $A = 1 - R$ and a are the surface transmissivity and the materials absorption coefficient. C_e , C_l are the heat capacities $[Jcm^{-3}K^{-1}]$ for the electron and lattice subsystems and γ is the electron phonon coupling parameter which can be expressed as $\gamma = \frac{C}{\tau}$, where τ stands for the electron, lattice characteristic heating phases, for every case.

1.2.2 TTM in the case of femtosecond pulses

Following the equations 5-7 which have three characteristic timescales τ_e, τ_l and τ_p where $\tau_e = C_e/\gamma$ the electron cooling time, $\tau_l = C_l/\gamma$ and τ_p the laser pulse duration. In our case the pulse duration is shorter than the electron cooling time $\tau_p \ll \tau_e$ as we irradiate with femtosecond pulses. So this means that for $t \ll \tau_e$, *the* $C_e/T_e \gg \gamma T_e$, the electron-lattice coupling can be neglected. So the electron temperature can be calculated as following:

$$C'_e \frac{\partial {T_e}^2}{\partial t} = 2(1 - R)I(t)ae^{-az} \tag{9}$$

Assuming that the laser intensity *I* and the material reflectivity R are constant in time, we end up with:

$$T_e(t) = \sqrt{(T_0{}^2 + \frac{2I_a a}{C_e{}'} t e^{-az})} \qquad (10)$$

Were $I_a=I_o$ A with I_0 constant, and $T_0=T_e(0)$ as the initial temperature. Finally at the end of the laser pulse we have:

$$T_e(\tau_p) \cong \sqrt{(\frac{2I_a \tau_p a}{C_e{}'})(e^{-az})} \qquad (11)$$

We ignore T_0 as the electron temperature is much higher than the initial temperature $T_0<<T_e$.

1.3.1 Hydrodynamics

Irradiating a target material surface with laser pulses causes local melting on the material surface provides that the pulse energy is sufficient to induce phase change. This phase transition is of much significance to the final shape and geometry of the produced structures. On a previous subchapter we examined how the heat flow progresses through time on the material surface. But we didn't consider what happens, when the liquid phase of the material moves and the possible hydrodynamic instabilities that occur, due to the temperature gradient that forms as a consequence of the inhomogeneous energy deposition. The melted material hydrodynamics has to be considered in this thesis as the fluid dynamics are more fit to explain some experimental results.

1.3.2 Navier-Stokes equation

The Navier–Stokes equations are used to describe the motion of fluid substances. These equations arise from applying Newton's second law to fluid motion, together with the assumption that the fluid stress is the sum of a diffusing viscous term (proportional to the gradient of velocity), plus a pressure term. A simplification of the Navier–Stokes equations flow equations is obtained when considering an incompressible flow (material density is constant within an infinitesimal volume that moves with the velocity of the fluid) of a Newtonian fluid. The assumption of incompressibility rules out the possibility of sound or shock waves to occur. In this sense the Navier–Stokes equations will read, in **vector** form (bold characters):

$$\frac{\partial \boldsymbol{u}}{\partial t} + (\boldsymbol{u} \cdot \nabla)\boldsymbol{u} - \nu\nabla^2 = -\nabla w + \boldsymbol{g} \qquad \text{(convective form)} \tag{121}$$

Where w is the specific (per mass unit) thermodynamic work, $\nu = \mu/\rho_0$ is the kinematic viscosity (ρ is the uniform density), **u** is the flow velocity, **g** specific body accelerations acting on the continuum (gravity). In the convective form the equation assumes the presence of convective acceleration: the effect of time-independent acceleration of a flow with respect to space. While individual fluid particles indeed experience time-dependent acceleration, the convective acceleration of the flow field is a spatial effect, one example being fluid speeding up in a nozzle. Depending on the parameters used, the Navier-Stokes equations can be solved and provide an estimation of the local pressure values that may lead the melted material to form convectional structure formations.

1.4 Formation of Laser induced periodic surface structures

Following irradiation with ultrashort pulses a plethora of self-assembled structures can be realized as the number of pulses applied increases. At first, the formation of ripples perpendicular to the laser beam occurs. Applying a greater number of pulses leads to the formation of microgrooves that form perpendicular to the ripples. If the number of pulses is even greater a quasi-periodic array of micro-spikes is shaped on the surface. The physical mechanism that bridges the inhomogeneous absorption of energy with the formation of LIPPS is vividly explored [46–54] though still open and debated.

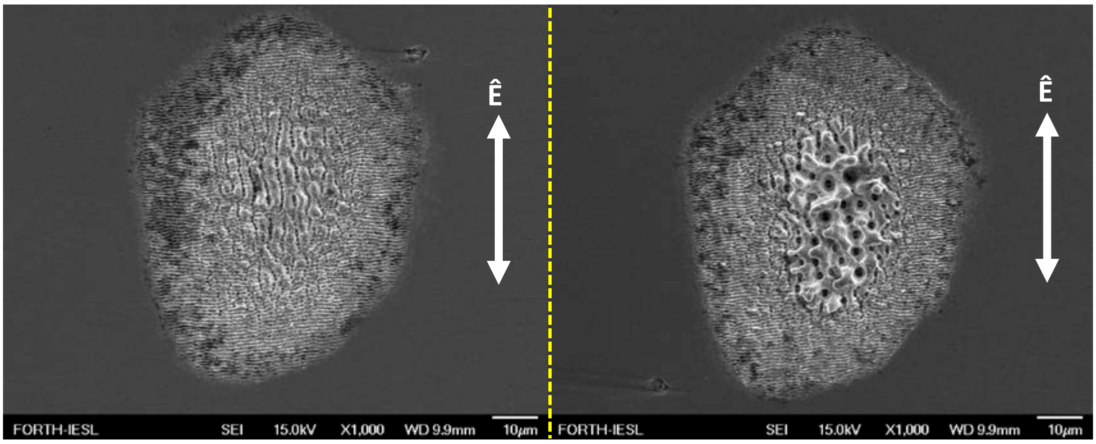

Figure 5: Illustration of microgrooves formed parallel to the beam polarization after irradiation with 40 pulses (left), spikes after irradiation with 80 pulses (right).

In particular, mass removal occurs due to the excessive temperatures that are reached, while the inhomogeneous deposition of energy induces recoil pressure from ablated regions, temperature gradient and surface tension variance along the irradiated area. These effects give rise to a Marangoni-driven flow and capillary waves that eventually lead to the formation of a rippled landscape upon resolidification. Upon increasingly irradiating the material with more pulses, leads to a rapid decrease of the efficacy factor [54], as consequence inhomogeneous deposition of energy diminishes leading to a gradual suppression of ripples. This implies that groove as well as spike formation cannot be ascribed to electrodynamics and SPP excitation as in the case of ripples. Investigating the transient evolution of lattice temperature indicates that hydro-dynamical effects control groove formation.

1.5 Processing in liquid environment

Laser processing has been implemented in various conditions sounding the target material beyond ambient air, such as vacuum, gas or liquid environment. Altering the environment of the experiment effectively alters the surface structures observed. In particular by immersing the target in water LIPSS with significantly reduced period [55–57] are observed by contrast to those observed during dry treatment while maintaining the same direction as in air. This suggests that there is a common formation mechanism. Moreover lower ablation threshold has been reported [58, 59] with irregular damage patterns which indicate Kerr-effect. Since water has a nonlinear refractive index (n_2) ~three orders of magnitude greater than that of air, specifically $n_{2_{water}} \approx 2.8 \times 10^{-16}\ cm^2/W$ while $n_{2_{air}} \approx 2.1 \times 10^{-19}\ cm^2/W$, the occurrence of laser-induced effects such as super-continuum generation, filamentation and optical breakdown is expected. All these effects can alter the Gaussian distribution of the laser beam.

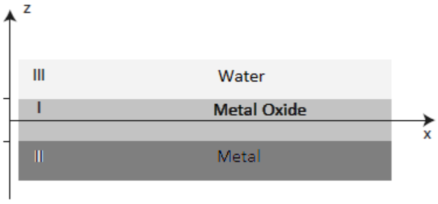

Figure 6: Multilayer system formed by the existence of the oxide layer between water and metal.

It has been shown that in the case of water an oxide film forms at the metal/water interface [60, 58]. This thin oxide layer that exists between the water continuum and the metal target effectively creates a multilayer system ultimately affecting SPP characteristics. This can explain both the physical mechanism of LIPSS formation under water confinement by modifying the SPP excitation mechanism, and the differentiation in LIPSS periodicity.

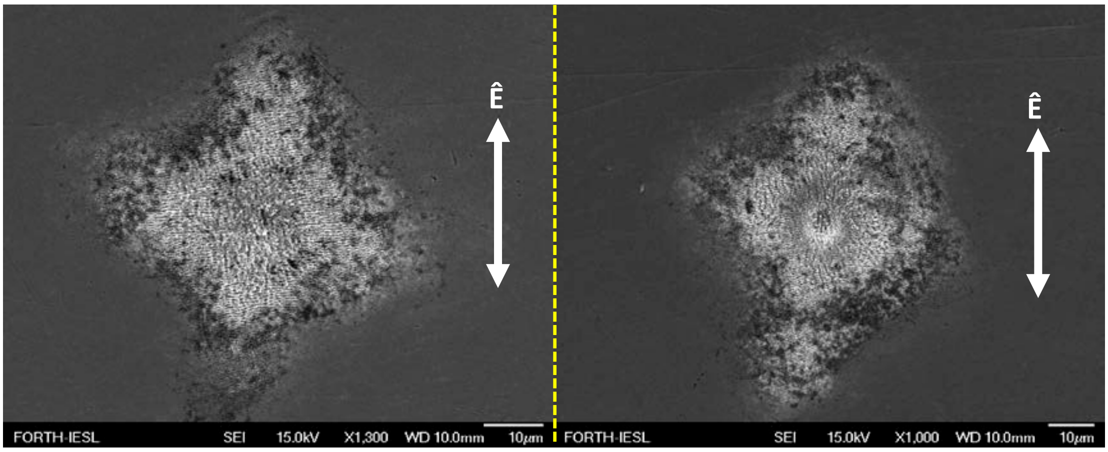

Figure 7: LIPPS formed by irradiation under water. Ripples (left) after 20 pulses, Grooves (right) after 80 pulses. Irregular damage pattern is observed, especially in the right figure where the crater suggests autofocusing effects. Period of LIPSS is reduced though the same alignment of the structures in relation to the beam polarization is the same as the dry experiment.

Chapter 2: Experimental setup & Data acquisition methods

At first, rough samples where polished with a rotary polishing tool after applying special polishing cream on the surface, then samples where thoroughly cleaned with soap to remove particles produced during polishing. Finally, samples where cleaned with a solution of acetone before and after irradiation. After laser treatment, structures were observed under field emission scanning electron microscope (FE-SEM). Finally, Wettability measurements were conducted after letting the samples in ambient air for ~15 days.

2.1 Laser system

All experiments in this thesis were performed on the ultrafast micro and nano processing (ULMNP) lab at FORTH-IESL, with the use of a Pharos laser system from Light Conversion. Pharos is a compact, solid state, single-unit, integrated, femtosecond laser system. It’s active medium is an ytterbium crystal doped with potassium, gadolinium and tungsten (Yb:KGW). It emits at a central wavelength of 1026nm and it supports second harmonic generation (SHG) of the fundamental at 513nm. PHAROS is built upon the conventional chirped pulse amplification technique. The maximum pulse energy is 1.5mJ and the repetition rate ranges from

1kHz up to 200kHz (60kHz-200kHz for second harmonic). The pulse width can vary from 170fs to 10ps controlled via pulse stretcher / compressor modules. It's also equipped with a built-in pulse picker which allows pulse-on-demand mode.

All experiments were conducted with minimum pulse duration ~170fs.

2.2 Experimental Setup

The experimental setup is illustrated on Fig. 8 with a sketch of the optical path from the laser system all the way to the sample target. Beam propagates from the laser guided by high reflective dielectric mirrors to a Glan-Thomson linear polarized with high extinction ratio up to 100.000:1 before passing through a zero-order half-wave plate. Pulses where focused with a spherical N-BK7 lens (60mm focal length) and the initial Gaussian spot diameter was 32μm measured on the focal plane by a CCD camera at $1/e^2$. The aperture of a laser-induced crater ($\sim 1/e^2$) at the original surface was taken as ablation area for more precise fluence calculation. Samples where positioned perpendicular to the incident beam and all irradiations were performed to air/metal or water/metal environment on a 3-axis motorized stage controlled from a computer. An internal laser shutter was used to define irradiation time and thus the number of pulses receptive to the sample or the built-in pulse picker when a small number of pulses were applied. For the dynamic processing procedures large areas where fabricated. Firstly, line scans were produced on the surfaces at variable velocity and then these line scans were brought together with variable line separation values affecting overlap between neighboring line scans. To estimate the number of pulses that effectively irradiates each area equal to the beam spot size we define the *one dimensional effective number of pulses* $N_{eff,1D}$ when line laser scanning and *two dimensional effective number of pulses* $N_{eff,2D}$ when 2D surfaces are fabricated.

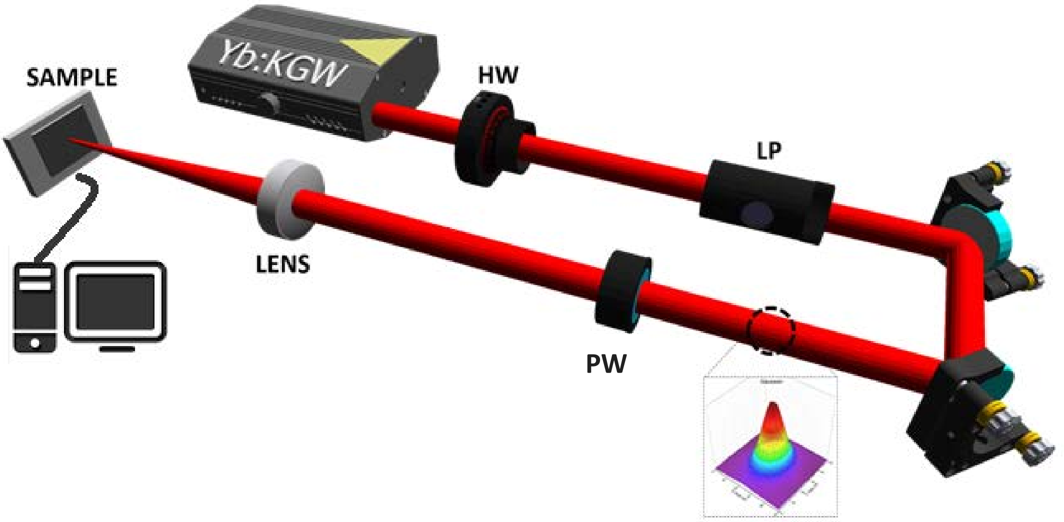

Figure 8: Experimental Setup. As it is showed beam power is controlled with a λ/2 waveplate (HW) which is used for rotating the initial S-polarization from the laser and a liner polarizer (LP) for detaining the electric field on y-axis. A Power meter (PW) is put in the beams path to measure its intensity.

The dynamic processing procedure is shown schematically in Fig.7. The observed morphology is much dependent on the parameters discussed during the formulation of the effective number of pulses.

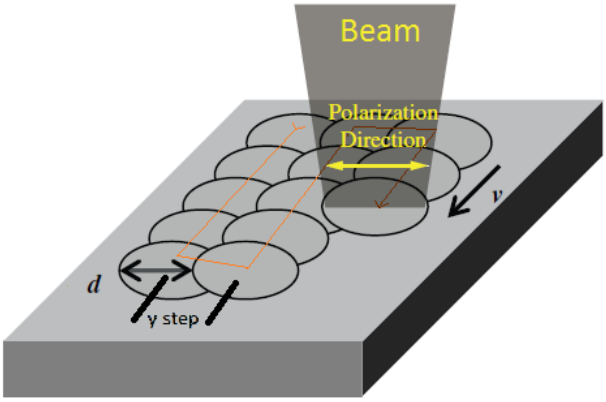

Figure 9: Dynamic laser scan processing procedure. First the beam scans a line with scan speed velocity v at the end of the line, the laser beam moves a predefined distance in the perpendicular direction y to start a new line scan. Progressively a large area is being fabricated.

The effective number of pulses plays a crucial role and defines not only the surface morphology covering an area but also the homogeneity of a 2D surface. $N_{eff,1D}$ and $N_{eff,2D}$ are calculated from formulas 13, 14.

$$N_{eff,1D} = \frac{r \times f}{v} \tag{13}$$

$$N_{eff,2D} = \frac{\pi \times r^2 \times f}{v \times y} \tag{14}$$

Where y is the consecutive scan line separation, r is the spot radius, f is Repetition rate and v is the laser scan velocity.

Images of the treated surfaces were taken by field emission, scanning electron microscopy (JEOL JSM-7500F).

2.3 Period measurement (Fourier analysis)

In order to characterize the structures besides the geometry and shape we had to find a way to automatically measure the frequency that LIPSS are appearing on the surface after the irradiation. Therefore to make accurate measurements of the ripple periodicity and its dispersion, the obtained SEM Images were transformed into Fourier-space images. The exact procedure of the transformation and analysis is presented in the following paragraph.

For being able to extract spatial frequency information as well as to conduct valid measurements and estimate the standard deviation of each measurement, 2D fast Fourier transform (2D-FFT) transform was utilized. High resolution (1280x1024) SEM images were 2D-FFT transformed on a new reverse-space image. The transformation changes the images dimensions. The new dimensions of the generated Fourier images are inversely proportional to *x* and *y* dimensions of the initial image. The orange axis represents the direction vertical to the ripple nanostructure. Along this axis the Fourier transformation detects a periodical fluctuation of the images color intensity (pixel color). This fluctuation has an average special frequency and dispersion. The length of this frequency is inversely proportional to the average ripple period. In image one can note the major symmetry axis of the image present in the 2D Fourier Transformed image. Fig. 10 presents as an example, SEM images of an irradiated laser spot featuring ripples (a), higher magnification of the enclosed area in the red dotted box (b). Fig. 10 (c), (d) show the Fourier space image of the image Fig. 10 (b). Consequently to calculate the periodicity of the structures, the profile of the image was taken as cross section, yellow dotted line tin Fig. 10 (d), which is shown in Fig.10 (e). The distance between the centre of Fig. 10 (f) with the first peak represents the characteristic frequency f of the periodic structure. In order to calculate the periodicity Λ, of the structures first we calculate the average frequency of the two peaks (as shown in Fig. 10 (e)) for a vertical as well as a horizontal image cross section, and so the average period is $< \Lambda >= 1/f$, where Λ is the period of the formations, and f is the *spatial frequency, periodicity*.

For the estimation of the amount, or range of frequencies that’s the 2D-FFT images show i.e. the standard deviation, we apply a Lorenzian fit on both peaks of the cross section and the error of every measurement is calculated as follows:

$$\boldsymbol{\Delta\Lambda} = \left|-\frac{\mathbf{1}}{\boldsymbol{f}^{2}}\right| \boldsymbol{\Delta f}$$

Where Δf is the mean of the widths for the two Lorenzian fit curves from the 2D-FFT image profile peaks.

The characterization of ripples period was determined with two dimensional fast Fourier transform (2D-FFT) on high analysis and high magnification Field emission-SEM images, using *Gwyddion* software.

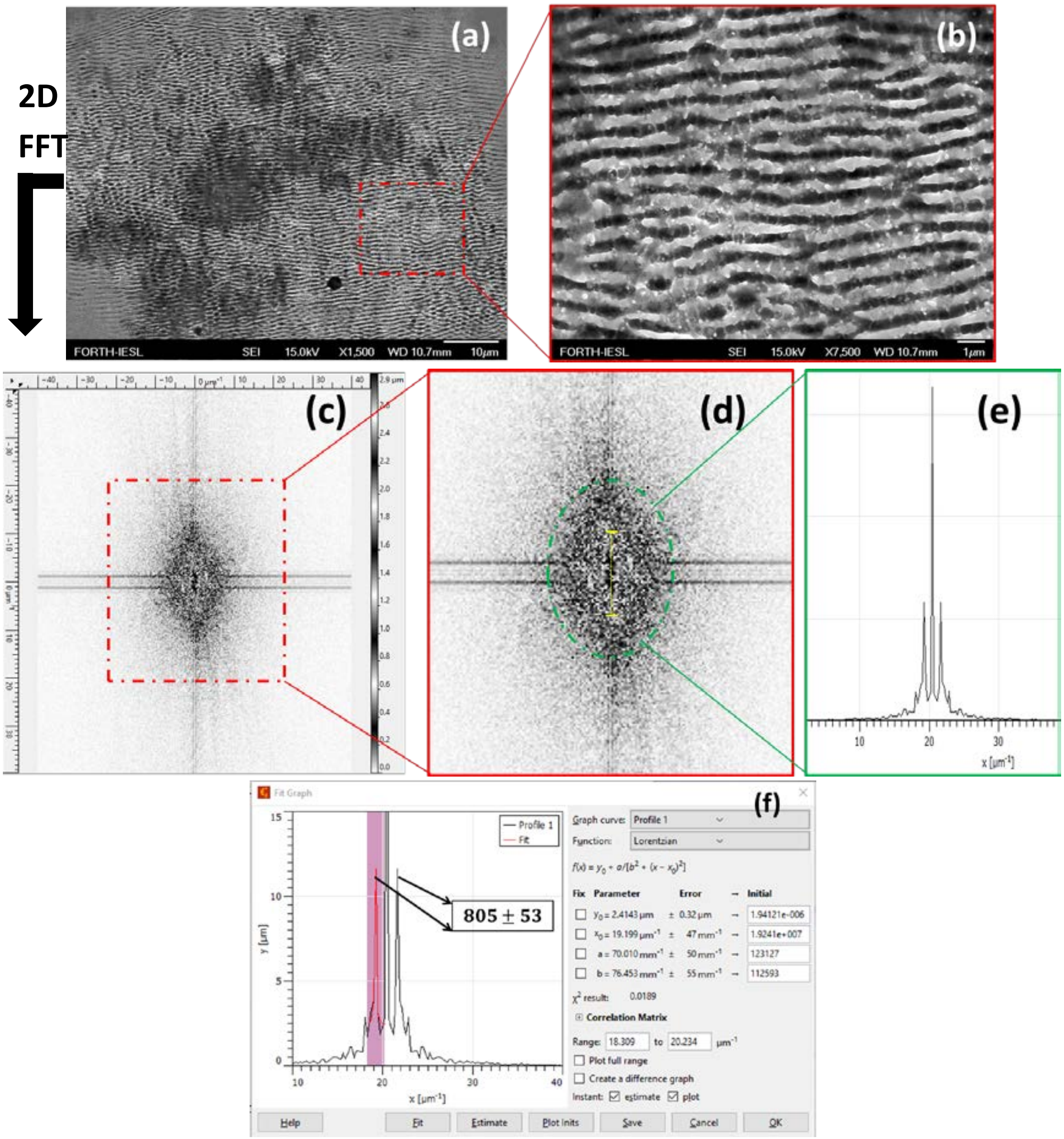

Graph curve: Profile 1

Function: Lorentzian

$f(x) = y_0 + a/[b^2 + (x - x_0)^2]$

Fix	Parameter	Error	→	Initial
☐	y_0 = 2.4143 μm	± 0.32 μm	→	1.94121e-006
☐	x_0 = 19.199 μm⁻¹	± 47 mm⁻¹	→	1.9241e+007
☐	a = 70.010 mm⁻¹	± 50 mm⁻¹	→	123127
☐	b = 76.453 mm⁻¹	± 55 mm⁻¹	→	112593

χ^2 result: 0.0189

⊞ Correlation Matrix

Range: 18.309 to 20.234 μm⁻¹

☐ Plot full range

☐ Create a difference graph

Instant: ☑ estimate ☑ plot

Figure 10: SEM image of irradiated spot featuring ripples (a), higher magnification (b), 2D-FFT transformation of (b) in grayscale (c), higher magnification showing the profile feed (yellow line), extracted intensity profile showing two symmetric peaks around a central peak (e), Lorentzian fit of the left peak and periodicity value extraction with standard deviation in nanometers unit.

2.4 Energy surface density (Peak Fluence) calculation

Peak Fluence is the surface energy density calculated from the laser beam intensity at its peak and the beam radius. Pulse energy is not sufficient to describe the experiment conditions since focal conditions and thus beam radius play a crucial role.

Firstly, we calculate the *pulse energy* (J), by measuring the *Average power* $(W = J/s)$ and dividing it by the *Repetition rate* (s^{-1}).

$$Pulse\ energy\ (J) = \frac{Power\ (Watt)}{Repetition\ rate\ \left(\frac{1}{s}\right)}$$

The spot radius can be found with two different methods: (I) by directly measuring the beam spot using a CCD camera located at the desired focal conditions that are used during irradiation of the samples, or (II) by measuring the imprint on the target surface after impinging it with the laser. In every case the spot size is calculated at $\frac{1}{\mathrm{e}^2}$ which is considered the *beam radius peak*, since the laser beam intensity profile is Gaussian (method I), and the damage profile of the imprint on the material will be Gaussian (method II).

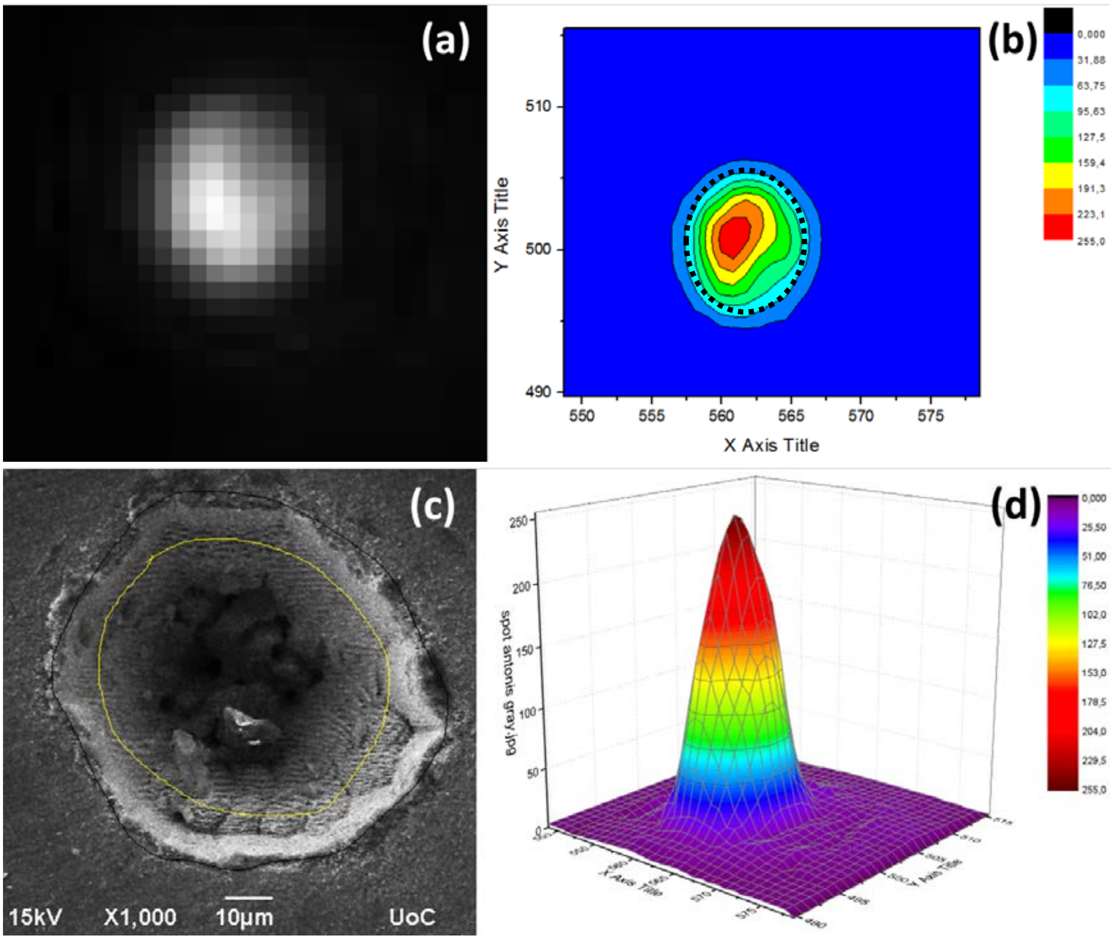

Figure 11a: Laser spot image captured from a CCD camera converted to grayscale (a), intensity profile of the laser spot with a Gaussian spatial filter (b), the laser spot area is encircled in black bold line, laser spot imprint on material surface, the full spot is encircled with black, $1/e^2$ beam area is encircled with yellow color (c), beam spot intensity in 3D chart demonstrating Gaussian profile (d).

Fig. 11a demonstrates method (I) steps: Beam spot captured with a CCD camera (a) demonstrating a Gaussian intensity profile in pixel color. This picture is converted to a 2D-color chart (b) and 3D-color chart (d), after applying spatial Gaussian filters. Beam radius can be calculated from (b) by converting distance in pixels, to true distance by taking into account the pixel size of the camera. Pixel size for the CCD camera used is 3,6 $\mu m/pixel$.

The conversion is given by the formula:

$$Beam\ radius = \frac{distance\ in\ pixels\ (pixel)}{pixel\ size\ (\frac{\mu m}{pixel})}$$

Fig. 11a (c) presents the imprint of the laser on a target. Beam radius can be calculated from the SEM image directly.

2.5 Electronic-Optical properties

As strong absorbing materials steel kinds' dielectric functions can be described by the Drude model [61], which reads:

$$\varepsilon_r(\omega) = \varepsilon_\infty - \frac{\omega_p^2}{\omega(\omega + i\Gamma)}$$

Where ω is the laser frequency, $\omega_P = (\frac{1}{2\pi c})(4\pi N e^2/m^* \varepsilon_\infty)^2$ is the plasma frequency, N is the free electron density which is a function of the electric field and Γ is the electron collision frequency, m^* is the effective optical mass of the laser-excited electrons. During irradiation in water confinement, the water medium can be highly exited reaching metallic state which can also be described by the Drude model [58, 18, 62].

We have to take into account the index matching that occurs during the water experiment which leads to a lower reflectivity and thus lower Fresnel reflection losses on the steel surface because of the presence of water. Before irradiation the laser beam has an initial intensity I_0 which impinges the sample. For **normal incidence** and by the assumption that all transmission mediums are **non-absorbing**, the Fresnel equation for the *reflectivity* (R) at the interface reads [61]:

$$R_{12} = \left|\frac{\tilde{n}_1 - \tilde{n}_2}{\tilde{n}_1 + \tilde{n}_2}\right|^2$$

The percentage of intensity finally reaching the target will be the fraction of the intensity that is transmitted. The *optical transmission* (T) through each interface can be calculated according to:

$$T_{12} = 1 - R_{12}$$

Where $\tilde{n}$ is the complex refractive index, the indices 1, 2 represent the different materials of the interface. The total intensity I_{tot} impinging the target will be multiplied by a factor which accounts for reflection losses at all interfaces along the optical path.

During **dry treatment** the only interface along the optical path is the air/steel interface, thus $\boldsymbol{I_{tot} = I_0 \times T_{as} = I_0 \times (1 - R_{as})}$, where a indicates air medium and s steel target. During **underwater treatment** there are two interfaces in the beam path, firstly air/water and secondly water/steel. I_{tot} Now becomes $\boldsymbol{I_{tot} = I_0 \times T_{aw} \times T_{ws} = I_0 \times (1 - R_{aw}) \times (1 - R_{ws})}$ where w subscript is indicative of the water medium.

Medium	n	k	Ref
Air	1.00	0	63
Water	1.33	0	64
Steel	3.03	3.68	65

Table 1: *Optical constants of media presented along the optical path,* $\tilde{n} = n + ik$.

Since these calculations were conducted for qualitative reasons, and since optical indexes vary for different steel types because of the great variance in composition of various elements that comprise each steel type, a single value was selected for the dielectric constant found in ref. 65 for stainless steel $\varepsilon_{r,steel} = -4.4 + 22.3$. Where $\varepsilon_r = \bar{\varepsilon}_r + i\tilde{\varepsilon}_r$, $\bar{\varepsilon}_r$ is the real part and $\tilde{\varepsilon}_r$ is the imaginary part of the dielectric constant. Using the dielectric constant, the optical constants can be calculated using following formulas:

$$|\varepsilon_r| = \sqrt{\bar{\varepsilon}_r^2 + \tilde{\varepsilon}_r^2}, \qquad n = \sqrt{\frac{|\varepsilon_r| + \bar{\varepsilon}_r}{2}}, \qquad k = \sqrt{\frac{|\varepsilon_r| - \bar{\varepsilon}_r}{2}}$$

Calculated values for steel are: $n = 3.03,\ k = 3.68$.

Using these values, we calculate $R_{as} = \left|\frac{1-3.03}{1+3.03}\right|^2 = 0.254,\ R_{aw} = \left|\frac{1-1.33}{1+1.33}\right|^2 = 0.02,$ $R_{as} = \left|\frac{1.33-3.03}{1.33+3.03}\right|^2 = 0.152.$

Finally, we calculate $\boldsymbol{I_{t,air} = 0.75 I_0}$ **for Air treatment**, and $\boldsymbol{I_{t,water} = 0.83 I_0}$ **for Water treatment**. This effect can partly explain the difference in damage thresholds observed.

2.6 Wettability Measurement (Contact angle)

Wettability measurements were taken for large fabricated areas covered with observed self-assembled structures using a motorized automated contact angle apparatus with the sessile drop technique. For water measurements, deionized water was loaded on a mechanically controlled syringe which produced $4\,\mu L$ droplets. Then the sample was carefully elevated until the water droplet touched the surface. Finally, the sample was drawn down steadily until the droplet detached from the edge of the syringe and stayed on the surface. A picture of the droplet was taken and Contact angle was measured automatically.

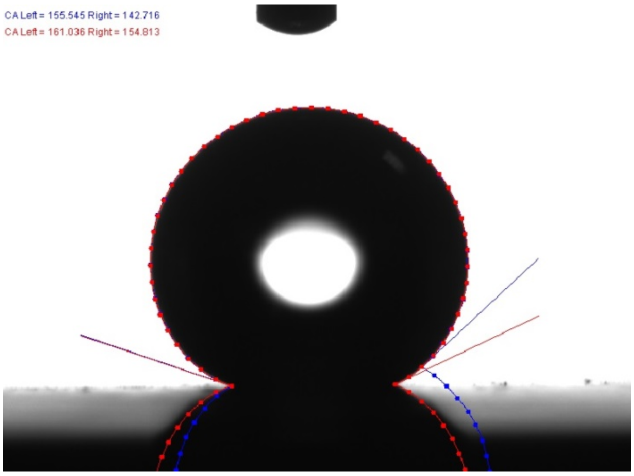

Figure 11b: Sessile drop technique demonstration. Water droplet is shown into the surface of stainless steel. Red dotted line covers the droplet shape to evaluate the droplet shape. Red solid line measures the contact angle.

The algorithm measures the angle by measuring the contrast of the pixels near the droplet edges taking into account the droplet shape. For oil measurements Shell© Rimula R3 10W (CF) energized lubricant oil was used

Measurement error represents standard deviation of contact angle measurement.

Chapter 3: Results & Discussion

Firstly, materials were treated with a defined number of pulses range at various fluences. Then the samples were examined and the observed morphologies were evaluated. Graphs were created exhibiting the observed morphology as a function of beam fluence and number of pulses. This procedure is called *Mapping.* Finally, large areas were fabricated one with each of the observed morphologies during the mapping process and their wetting behavior was examined ~14 days after irradiation. This procedure was conducted in ambient air and under water confinement.

3.1 Surface morphology mapping

Mapping procedure was conducted on various types of steel, in particular *1.4307 stainless steel*, 100CR6 *steel*, *1.7131 steel* and *1.7225 steel*. Results were similar for all kinds of steel.

3.1.1 Dry processing

By observing SEM images, various surface morphologies can be recognized.

Stainless steel

1026 nm

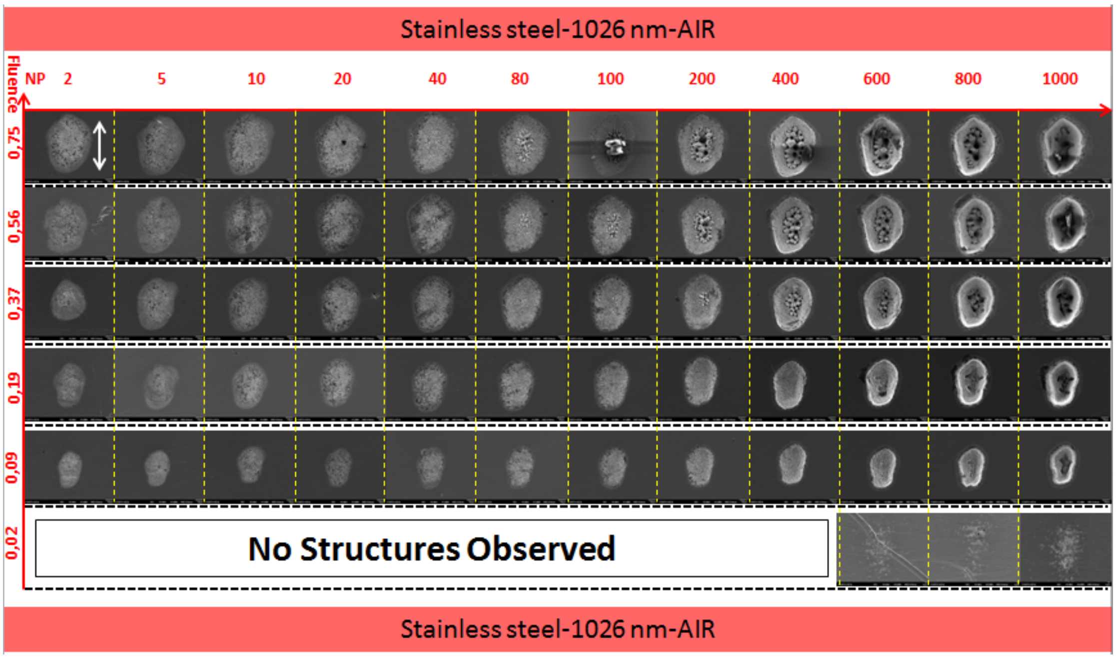

Figure 12: Laser spots on the surface of stainless steel after irradiation with 170fs pulses of 1026 nm. Various self-assembled structured are formed depending on the beam fluence and number of pulses.

At first, we observe the formation of ripples always perpendicular to the beam polarization. Ripples start to form even after the second pulse. For higher fluences microgrooves start to appear after NP=10. For intermediate fluences microgrooves start appearing after NP=40, while for the lowest fluences no grooves are observed as can be seen in Fig. 12. Spike formation follows for NP=80 for higher fluence while for intermediate fluences spike formation begins after 100 or more pulses. For a very high number of pulses (NP~1000) no structures can be observed since material removal is excessive leading to hole formation for all fluences.

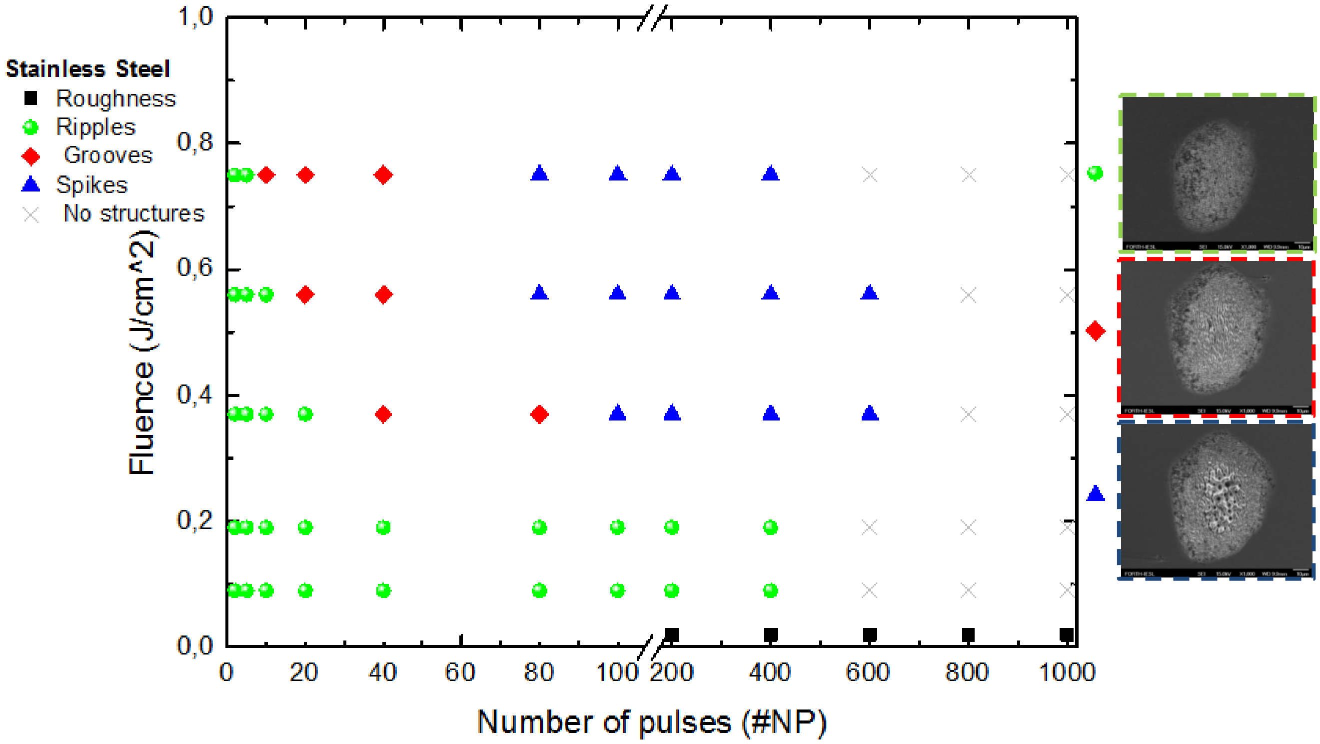

Figure 13: Morphological map for stainless steel showing all observed structures after irradiation with a preset number of pulses (NP) range for various fluences.

For the lowest fluence $(0{,}02\ j/cm^2)$ no irradiation spots can be observed for $NP < 600$ which is expected since we are much below single shot damage threshold and a great number of pulses is needed to induce surface damage.

513 nm

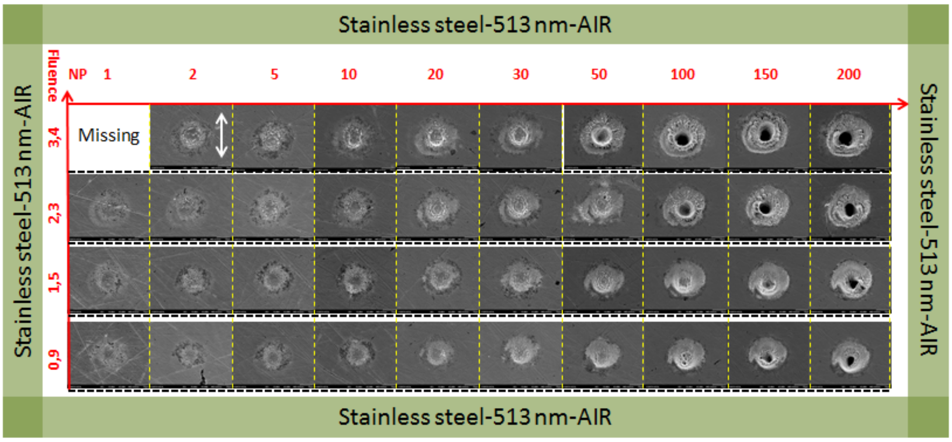

Figure 14: Laser spots on the surface of stainless steel after irradiation with 170fs pulses of 513 nm.

Fig. 14 shows laser spots obtained after irradiation of stainless steel samples with the second harmonic generated from the laser system, with central wavelength of 513 nm. As it is shown in Fig. 15 both ripples microgrooves and spikes are observed.

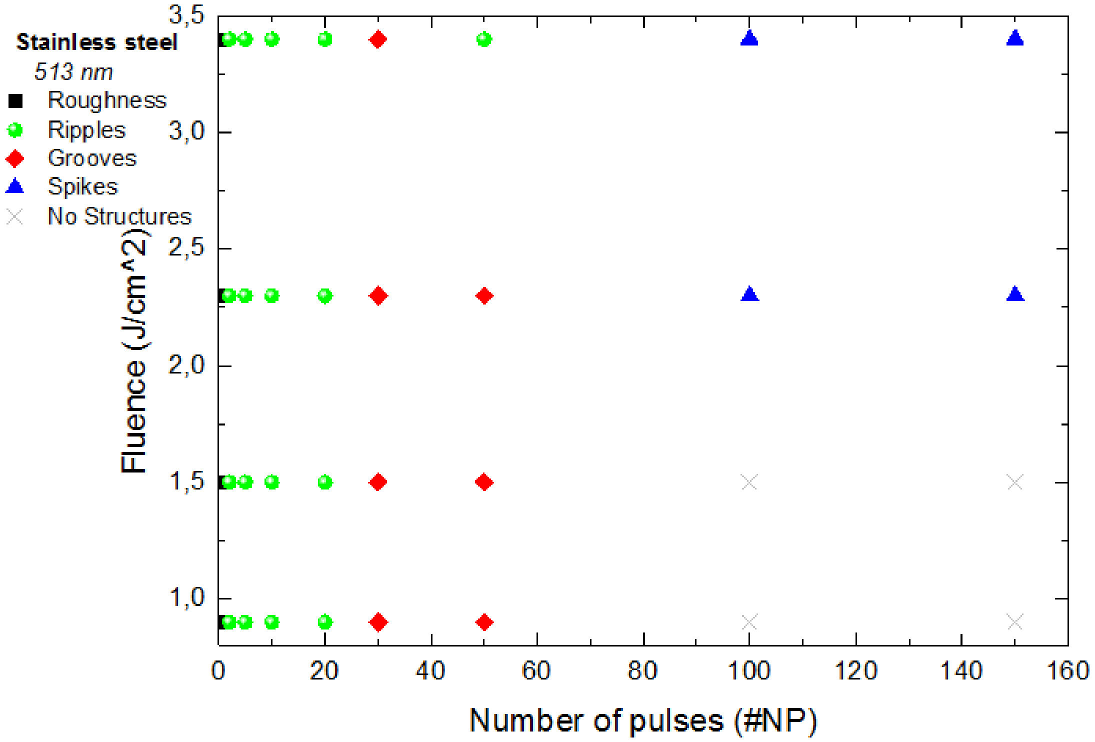

Figure 15: Morphological map for stainless steel showing all observed structures after irradiation with a preset number of pulses (NP) range for various fluences for 513 nm.

Surface structures observed follow the same trend concerning their formation order. Contrary to irradiation with 1026 nm, in this case mushroom like formations can be observed in the central region of the spots possibly due to the vastly greater fluences used.

A beam of central wavelength of 513 nm compared to 1026 nm has double the photon energy which can induce interband transitions [60, 77–80], which can be theoretically described by the same approach used for direct band transitions in semiconductors [78, 79], while 1026 nm induces intraband transitions [60]. This fundamental difference may have an effect on carrier excitation.

Furthermore, 513 nm has half the wavelength compared to 1026 nm, meaning that is has also double the k-vector. A change in k-vector leads to a modulation of the efficacy factor. As can be seen in Eq. 2 efficacy factor is a function of the incident k-vector, thus different wavelengths imply a different efficacy factor. The same holds for $b(\vec{k})$ meaning that each wavelength “sees” surface roughness in a different manner.

100CR6 steel

1026 nm

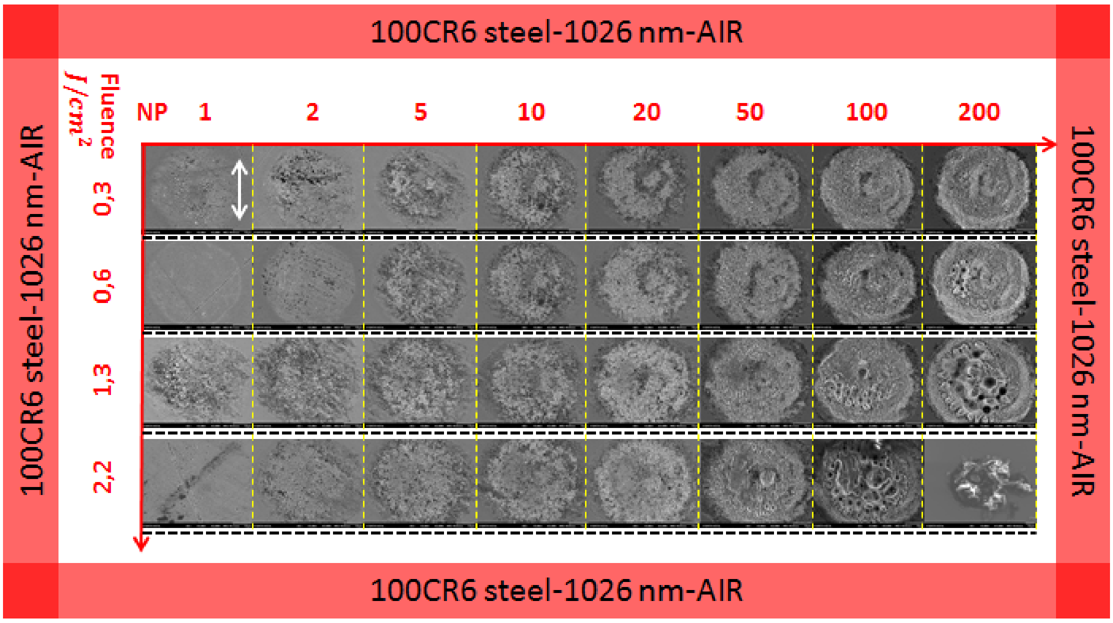

Figure 16: Laser spots on the surface of 100CR6 steel after irradiation with 170fs pulses of 1026 nm. Observed structures (ripples, microgrooves, spikes) are typical for steel samples.

Irradiation spots for 100CR6 steel resemble those on the surface of stainless steel.

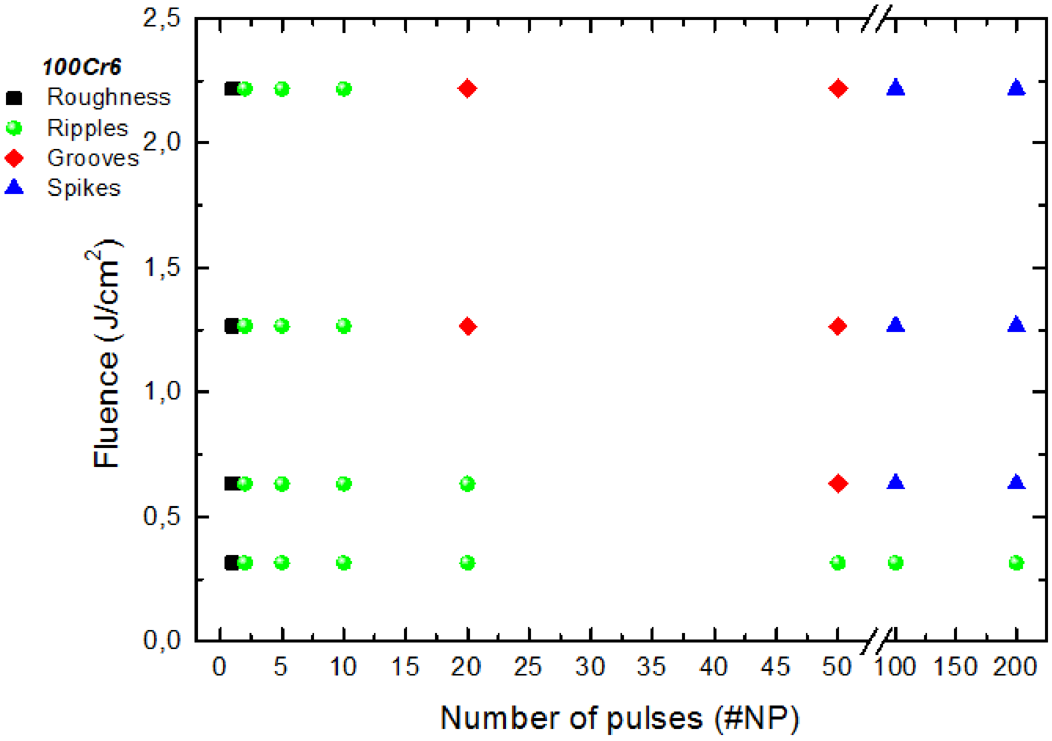

Figure 17: Morphological map for 100CR6 steel.

Ripples can be observed after the second pulse but not for the first pulse which roughens the target area. Microgroove and spike formation depends on the fluence as can be seen in fig. 13. For the lowest fluence not grooves or spikes can be observed even after NP = 200. At $1{,}3\,J/cm^2$ and $2{,}2\,J/cm^2$ microgrooves are formed after 20 pulses while for $0{,}6\,J/cm^2$ they appear only after the 50th pulse.

513 nm

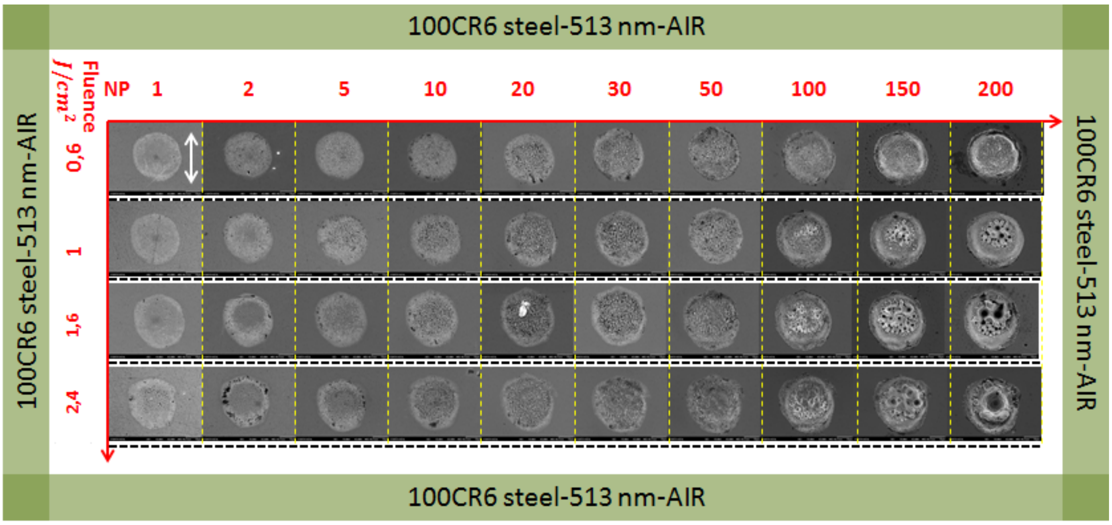

Figure 18: Laser spots on the surface of 100CR6 steel after irradiation with 170fs pulses of 513 nm.

Fig. 16 shows laser spots on the surface of 100CR6 steel after irradiation with 513 nm. As in the case of stainless steel, irradiation with 513 nm beam induces formation of mushroom-like structures on the center of the spot.

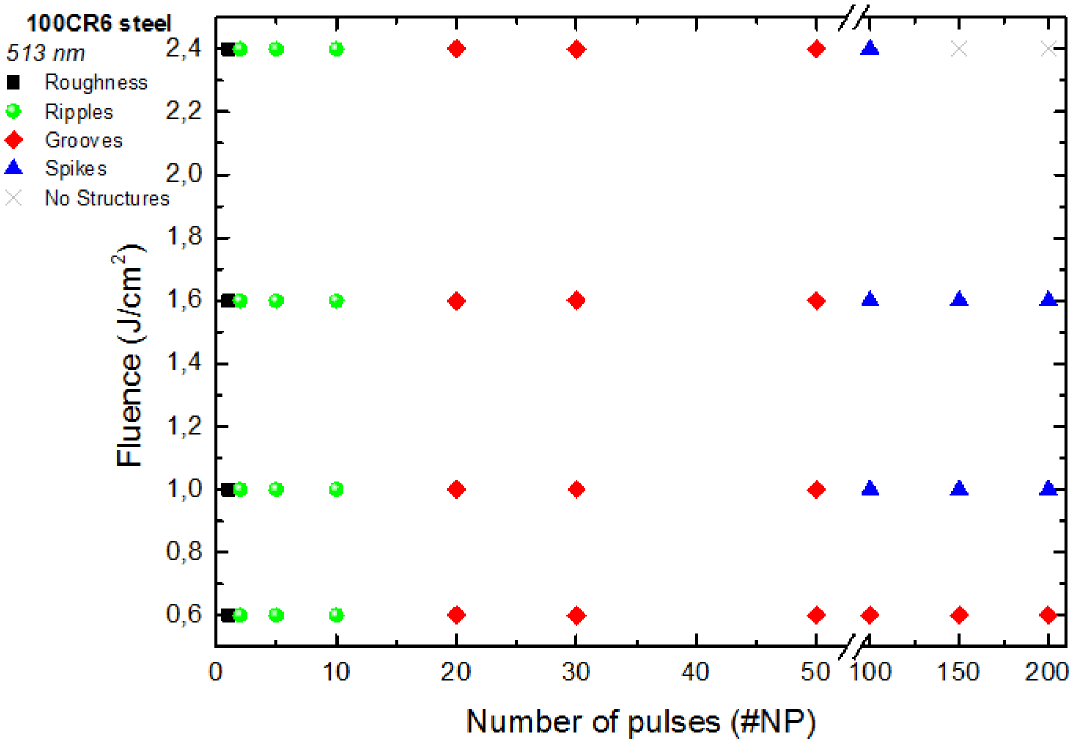

Figure 19: Morphological map for 100CR6 Steel after 513 nm irradiation.

Fig. 17 shows the formation conditions of Ripples, grooves and spikes. As for irradiation with 1026 nm, after just one pulse, no ripples can be observed.

1.7131 Steel (Dry processing)

Similarly by observing SEM images after illumination the morphological map for 1.7131 steel is formulated.

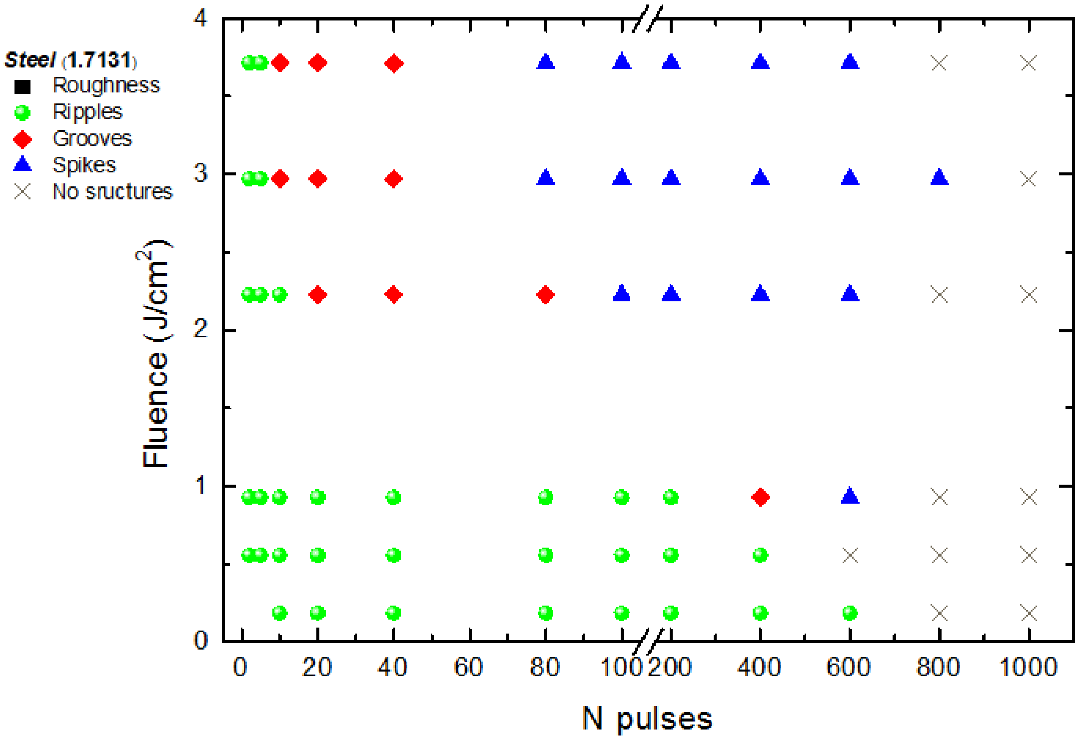

Figure 20: Morphological map for 1.7131 Steel after 1026 nm irradiation.

As can be seen by comparing morphological maps for different kinds of steel investigated, many similarities can be realized. In all kinds of steel ripples, grooves and spikes can be observed. Ripples form at low number of pulses, microgrooves at intermediate and spikes at high number of pulses. At even higher number of pulses, especially if fluence is high, no structures are observed since the surface is then ablated excessively. Finally, grooves and spikes have a strong dependence of the fluence of the laser beam since at low fluences no grooves/spikes are observed even at very high NP. Material removal dominates grooves/spike formation at this fluence regime, as can be seen in Fig. 13, Fig. 17 and Fig. 20 material removal is profound after ripples form but before grooves start to appear. Finally, we observe that the higher the beam fluence the lower the NP needed to induce groove/spike formation. This trend can be seen for 1026 nm irradiation while this is not the case for the second harmonic experiment suggesting that photon energy might play a role in groove/spike formation.

3.1.2 Processing in the presence of water

Processing in water confinement was conducted for Stainless steel and 1.7131 steel. Samples were placed in a glass petri dish filled with deionized water. Water volume was selected to cover each material ~3mm. During irradiation higher modification threshold was observed as LIPSS formed after relatively higher number of pulses. Morphological features also differed since mushroom-like formations were observed and debris redeposition was negligible. Ablated material was suspended in the water phase giving the water a milky aspect, while high NP induced cavitation bubbles formation.

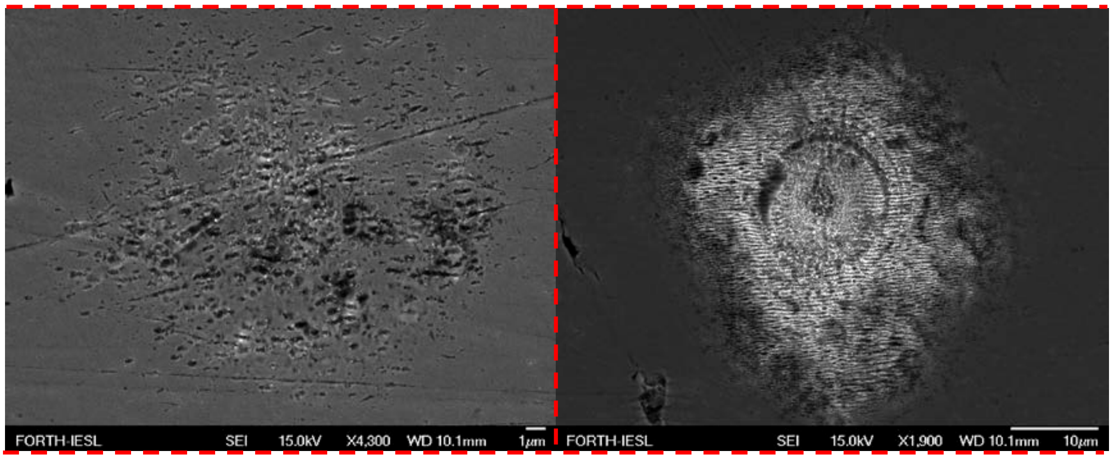

Figure 21: Laser spots under water confinement at low NP (NP=2) (left), high NP (NP=800) (right).

Furthermore underwater corrugated surfaces exhibited anomalous profile at low NP (Fig 21, left) and at high NP after bubble formation (Fig 21, right).

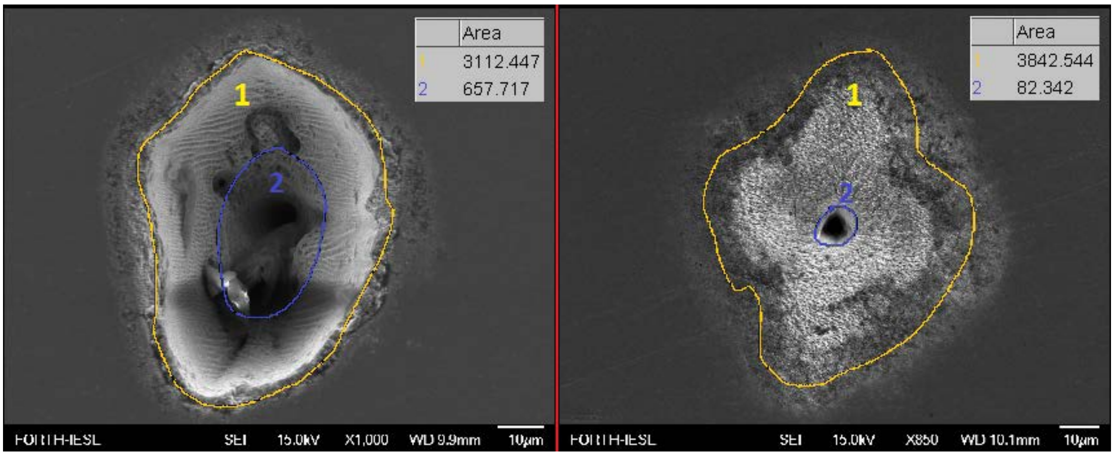

Figure 22: Damage profiles on Stainless Steel after 1000 NP in Air (left), Water (right). Fluences are $0{,}75\ J/cm^2$ for the dry experiment, and $0{,}87\ J/cm^2$ for the liquid experiment.

Profiles of underwater cavities obtained at high fluences and high number of pulses per spot, were consistent with a strong spatial deformation of the laser beam by comparison to the dry experiment. Fig. 22 demonstrates the cavities observed at the dry experiment in the left picture, and the one observed in the liquid experiment. As it can be seen in the air experiment the cavity has a profile consistent to a Gaussian distribution of laser intensity. The ablated material leaded to a gradually deeper cavity and most of the laser spot is ablated. In the right picture ablation was limited to a tiny central cavity while the surrounding irradiated spot is covered with LIPSS. This may be correlated with the occurrence of laser induced effects in the water layer in front of the target surface like fluence dependent self-focusing. This could explain the slit like crater observed in the region where laser intensity is at its peak. Total ablated region in the air experiment (area circled in blue curve) is 21% of the total area of the irradiated spot (are encircled in yellow) while in the water experiment is it only 2.1%. Furthermore, in the air spot material redeposition is evident near the spot edges.

Stainless steel

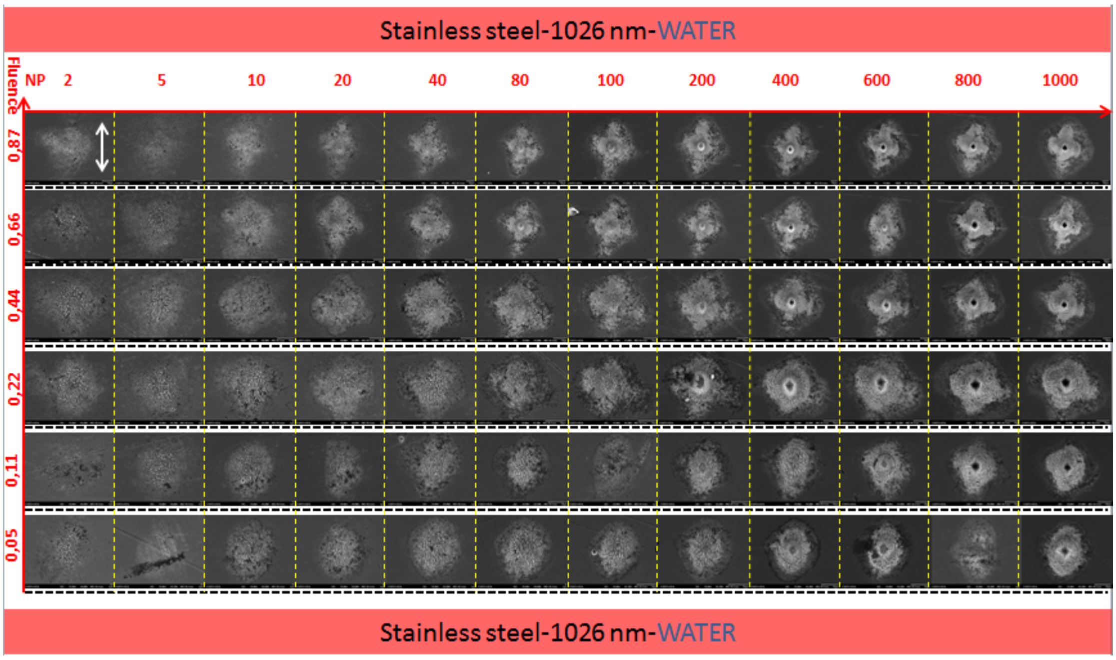

Figure 23: Laser spots SEM images on the surface of stainless steel after irradiation with 170fs pulses of 1026 nm under water confinement. Irregular surface damage for a Gaussian beam can be observed especially for low NP and low fluence, since several circle-like damage patterns form far from the beam center. Ripples and microgrooves can be observed at relatively higher NP compared to the dry experiment.

It is known that phenomena like supercontinuum generation, filamentation and optical breakdown of the water phase have a shielding effect, which reduces the amount of energy reaching the target. These effects coexist in water above certain threshold values [55]. For self-focusing and filamentation this value is $P_{crit} = 4.4 \times 10^{6}\ W$ and for optical breakdown $I_{crit} = 1.2 \times 10^{13}\ W/cm^{2}$. In the case of a ~170 fs pulse with a waist radius at the focal point of $\omega_0 = 23\ \mu m$ these values become $\Phi_{cr,fil} = 0{,}05\ J/cm^{2}$ and $\Phi_{cr,opt} = 2\ J/cm^{2}$. To avoid reaching such fluence values tight focusing of the laser beam was avoided, thus samples were placed in slightly defocused position (~600 μm) before the focal plane of the lens.

Fig. 23 demonstrates SEM imaged of the machined surface under water confinement. At low NP damage patterns lead to surface modification occurring in the form of solidified concentric waves surrounding a central region covered with mushroom like protrusions. These formations can be accounted to ablated particles that solidify before they completely detach from the illuminated surface. After irradiation with more than ~100 pulses, the water layer was mechanically perturbed to mix the suspended ablated particles in order to minimize scattering of the laser beam from regions with very high concentration of particles. The same procedure was conducted when bubbles where formed and remained in the water surface. Damage profile which resulted from beam scattering from bubbles formed after irradiation occurred frequent at high NP (Fig. 21 left).

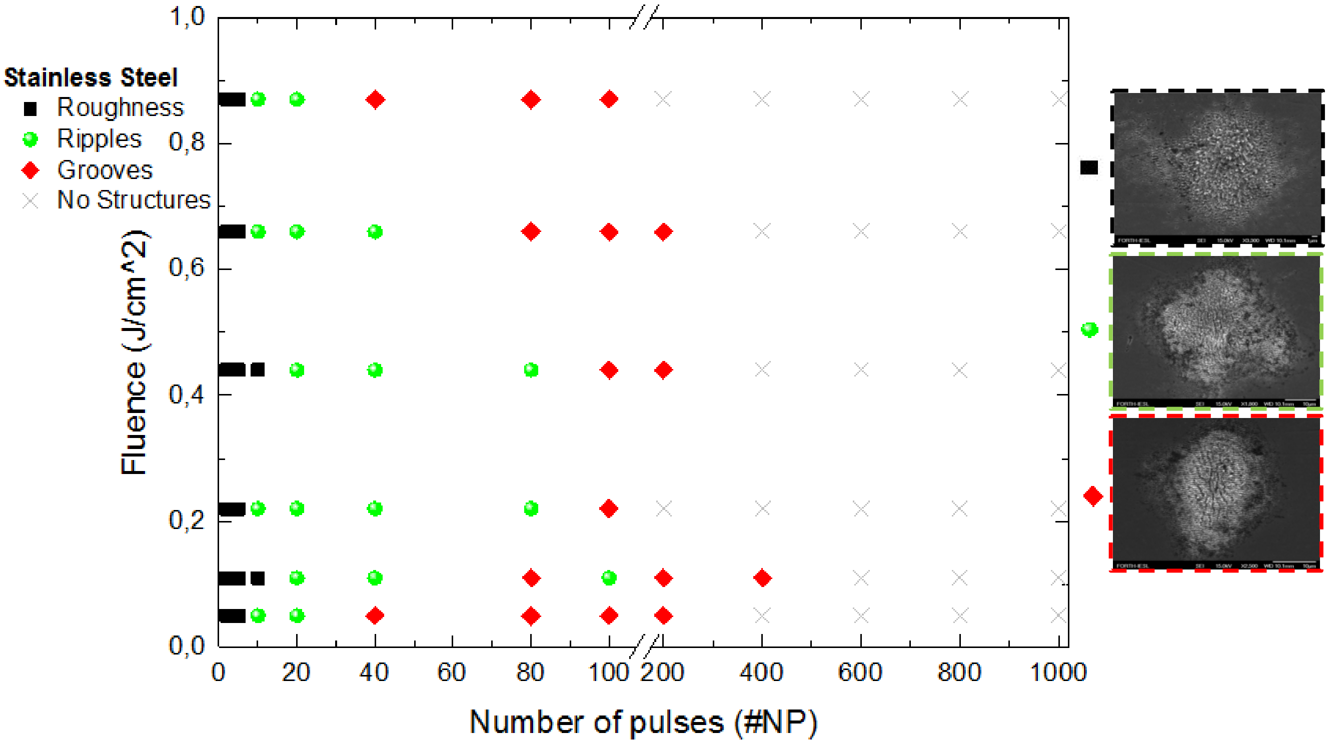

Figure 24: Morphological map for stainless steel after processing in water environment. Surfaces of high roughness have mushroom like formation. Ripples and grooves form at relatively higher NP. Spikes are not observed.

Morphologies realized during irradiation in water environment are presented in Fig. 24. Regions of high roughness bear resemblance to mushrooms in contrast to the dry experiment where initial damage patterns looked like solidified bubbles. Ripples and microgrooves form at relatively higher NP compared to surfaces treated in ambient air suggesting a higher modification threshold in the water experiment. Irradiation with even higher NP leads to the formation of a cavity in the center of the spot. No microspikes are observed.

100CR6 steel

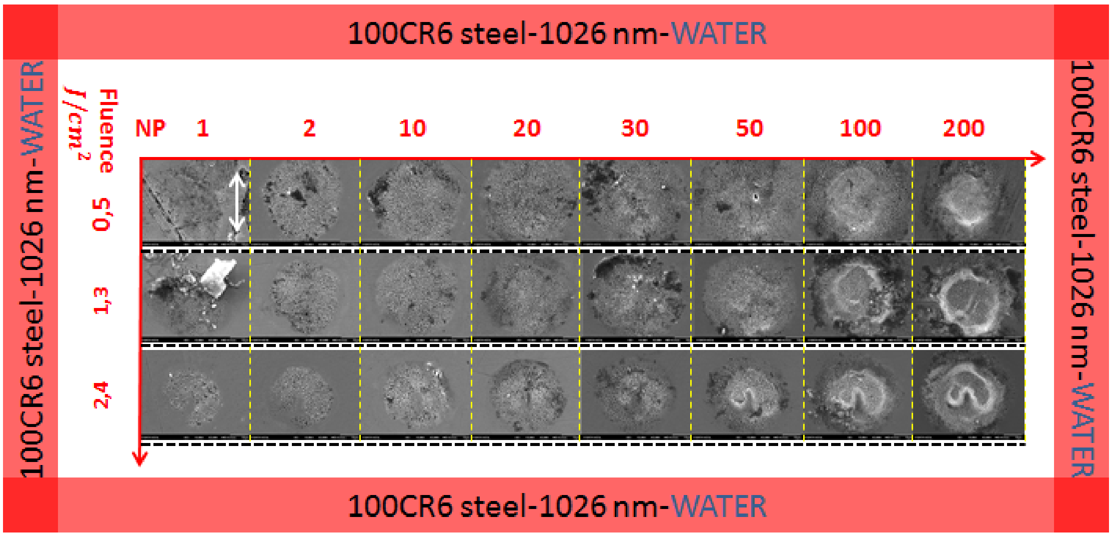

Figure 25: Laser spots SEM images on the surface of 100CR6 steel after irradiation with 170fs pulses of 1026 nm under water confinement. Similar morphological modification can be observed in the surfaces of this kind of steel as those observed on stainless steel.

In this type of steel, irradiation in water confinement has a similar behavior as irradiation of stainless steel.

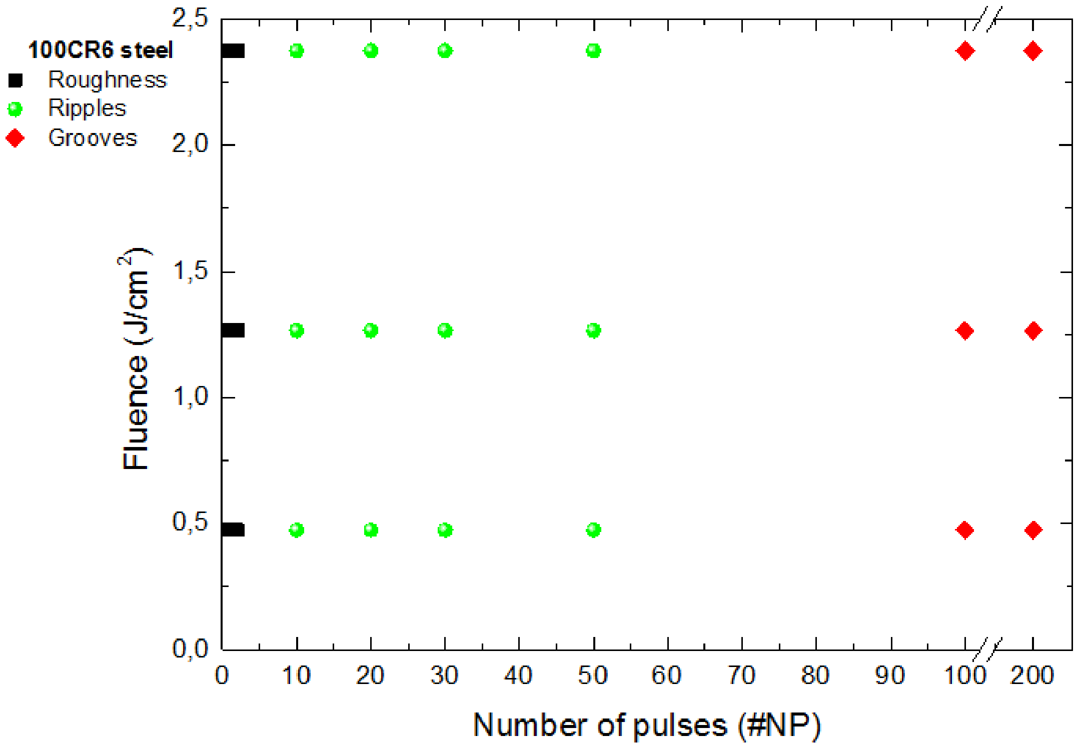

Figure 26: Morphological map for 100CR6 steel after processing in water environment. Ripples and microgrooves are formed.

At NP=1 damage profile consists of randomly arranged hole formations around a central region.

In the water experiment only ripples and microgrooves but no spikes are observed for this type of steel. The same observation was done for stainless steel suggesting that spike formation is inhibited in the presence of water regardless of the steel type.

3.2 LIPSS Periodicity Study

LIPSS periodicity is examined as a function of NP and fluence. Periodicity dependence helps unravel the physical mechanism governing their formation, and elucidate transient evolution of NP dependent dynamics. This study was conducted on two types of steel, stainless steel and 100CR6 steel.

3.2.1 LIPSS Periodicity study in dry experiment

LIPSS periodicity shows dependence on the number of pulses for both type of steel used in this study. The evolution of periodicity with the number of pulses is plotted and compared to the periodicity evolution with fluence. Fig 27 illustrates the evolution of ripples periodicity with fluence (Fig 27 (a), (c), (f)) and NP (Fig 27 (b), (d), (e)). It is shown that fluence does not modulate ripples periodicity for a given number of pulses. Periodicity variance appears to be minute and does not seem to follow a normal trend. On the contrary, ripples modulation with NP is evident for both materials (Fig 27 (b) for stainless steel, (e) for 100CR6 steel). It can be seen that ripples periodicity drops as the number of pulses increases rapidly at first but this increase slows up for NP~40. At first, NP=2 ripples period is calculated to be ~$0,9\lambda$ but after NP=250 the period drops to $0,7\lambda$ (Fig.27).

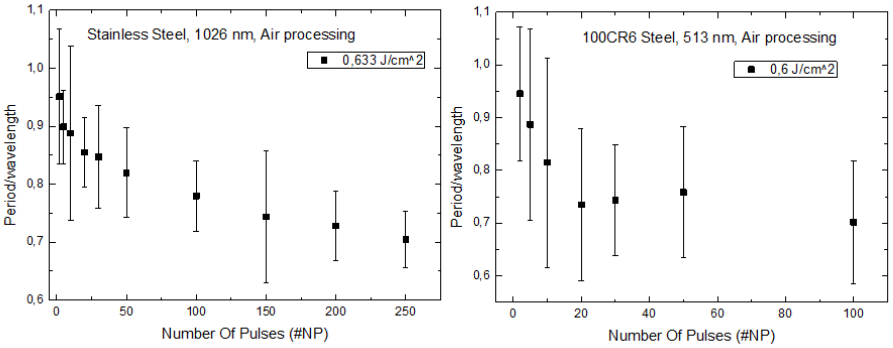

Figure 27: Ripples periodicity evolution with NP for two different wavelengths. Λ/λ as a function of NP shows a decrease from ~0,95 λ initially after NP=2, to 0,7λ for NP=250 and NP=100 respectively. 1026 nm (left), 513 nm (right).

This variation in ripples periodicity has been reported and attributed to the enlargement of the spot crater as NP increases [66].

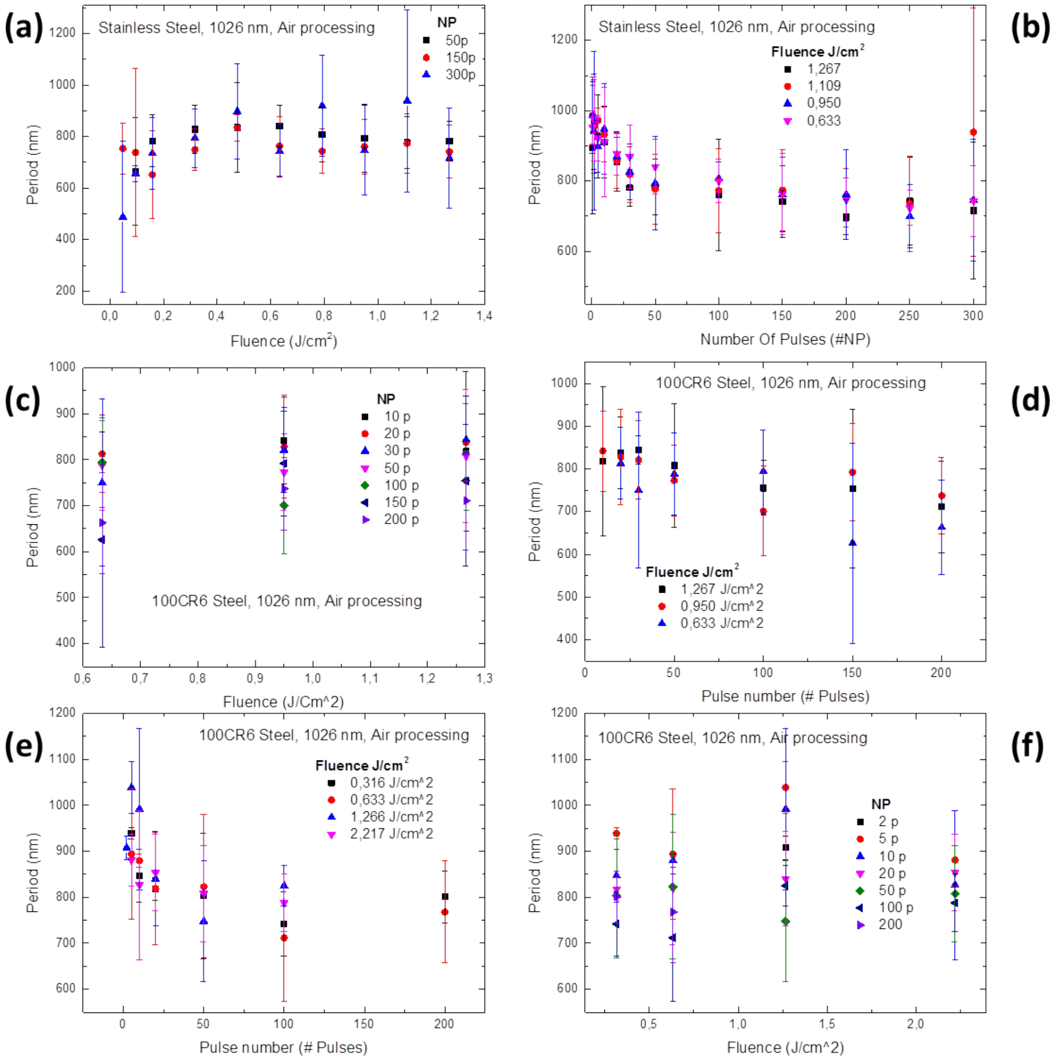

Figure 28: LIPSS periodicity as a function of fluence, for stainless steel (a), 100CR6 steel (c), (f), as a function of NP for stainless steel (b), 100CR6 steel (d), (e).

As the crater increases, fluence in the periphery of the spot declines. As a consequence, the number of excited electrons in the periphery decreases. As Eq. 17 predicts [66] as n decreases, ε_1 decreases. Ultimately, this leads to a decrease in λ_s and Λ. It can be noted by comparing Fig. 28 (b) and (e) that this trend is similar to both kinds of steel implying the universal nature of the ripples evolution mechanism. Furthermore, it has been shown that after the formation of initial gratings, the laser beam coupling with SPP is enhanced and the laser field localizes in the groove [66] making the grooves deeper and shaping ripples more regularly. It is also shown that ripples period decreases as their grooves become deeper [67]. Moreover, the ablated material rich plume that follows irradiation increases the dielectric constant of air near the target surface which can also reduce ripples period [66]. A combination of all these effects account for rapid period decrease with NP.

The aforementioned mechanism holds for materials processing using the second harmonic generated 513 nm beam. Fig. 29 demonstrates diagrams linking ripples periodicity with fluence (b), (c) and NP (a), (d). It is shown that fluence does not affect ripples periodicity in a normal manner. On the contrary, period decreases (periodicity i.e. spatial frequency increases) when NP increases as shown for 1026 irradiation. This is more evident in Fig. 29 (d) where more moderate fluences were used. In Fig. 29 (a) this trend is more evident for the lower fluences 0,9 J/cm^2 and 1,5 J/cm^2, this may be attributed to the much higher material ablation for the higher fluences which leads to a wider and deeper crater deforming ripples.

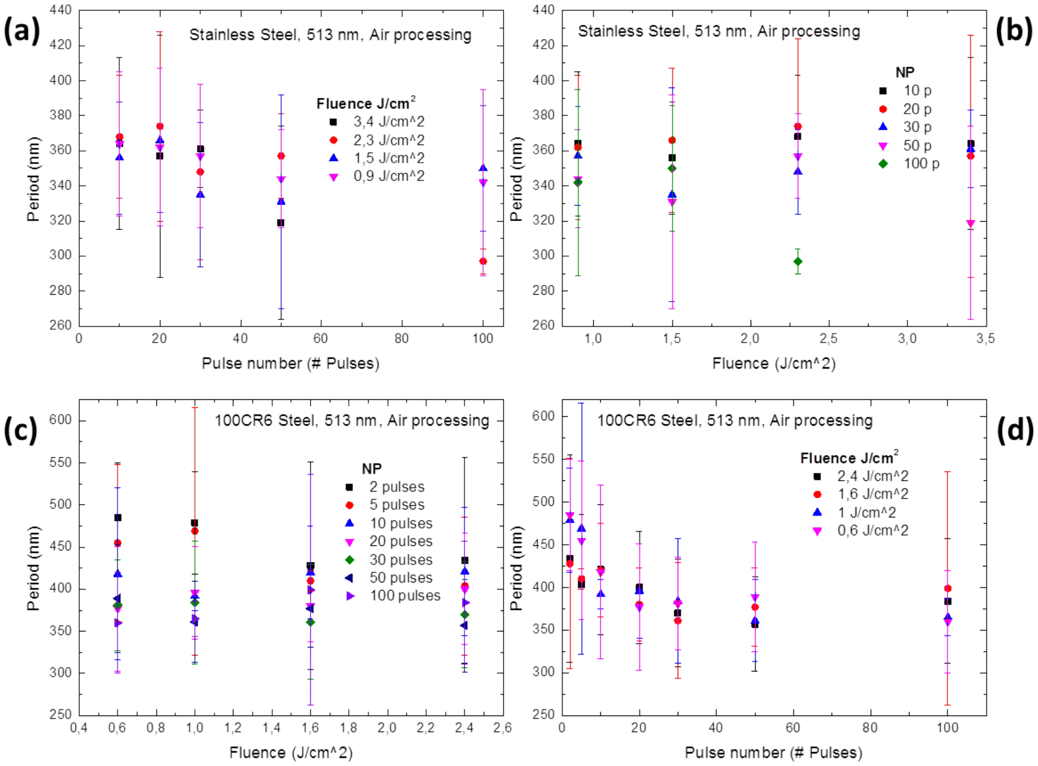

Figure 29: LIPSS periodicity as a function of fluence, for stainless steel (b), 100CR6 steel (c), (f), as a function of NP, stainless steel (a), 100CR6 steel (d) using the second harmonic 513 nm beam.

In the irradiated spots with higher fluences, a melted layer can be observed on the central region of the spot for low NP, before excessive ablation occurs. This molten layer further destabilizes rippled formations obscuring their topography near the edges. This is also observed in the wider error bars systematically seen for higher fluences.

It must me noted that Ripples periodicity shows variance along an individual spot. This variance qualitatively appears as a splitting of a single ripple into two which leads to more closely arranged formations. Fig. 30 demonstrates the aforementioned evolution of periodicity resulting from the splitting of a ripple into two. This was observed for selected spots near the edges for lower fluences. This phenomenon has been observed [68] on the surface of steel and its physical mechanism is attributed to electric field localization on the protuberance of the ripples that occurs when the coupling of SPP and incident wave is not very strong explaining the reason why ripples splitting is observed only for lower fluences.

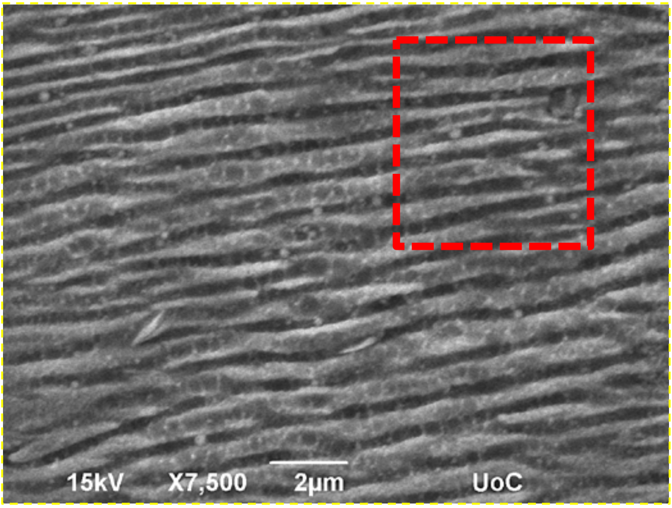

Figure 30: Ripples at the edge of a spot indicating ripple splitting in the region inside the red dotted box. Fluence is $0{,}095\ J/cm^2$*, NP=30.*

A special type of LIPPS observed is aligned parallel to the beam polarization and has a much lower period. This kind of LIPPS is observed for very low NP and their formation mechanism is obscure although they have been reported lately and discussed [14].

Fig. 31 depicts such LIPPS observed on the surface of 100CR6 steel after 10 pulses. The usual ripples discussed in this work have started to appear in the background.

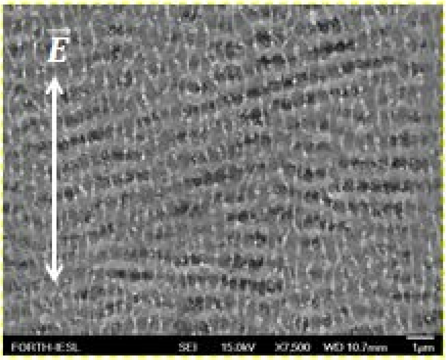

Figure 31: High spatial frequency LIPPS aligned parallel to the laser polarization, observed after 10 pulses with $1{,}267\ J/cm^2$*fluence on the surface of 100CR6 steel.*

The occurrence of this kind of very high periodicity LIPPS is relatively rare, and their existence frame in terms of NP is very low, as they tend to appear in a very narrow range of NP (between 1 and 10). Furthermore, their alignment parallel to the incident E-field as well as their frozen-droplet morphology suggests a completely different physical formation mechanism. For these reasons this type of LIPPS is beyond the scope of this work.

3.2.2 LIPSS Periodicity study in water experiment (1026 nm)

A similar analysis was conducted for processing in liquid environment impinging the target materials with the fundamental harmonic of 1026 nm.

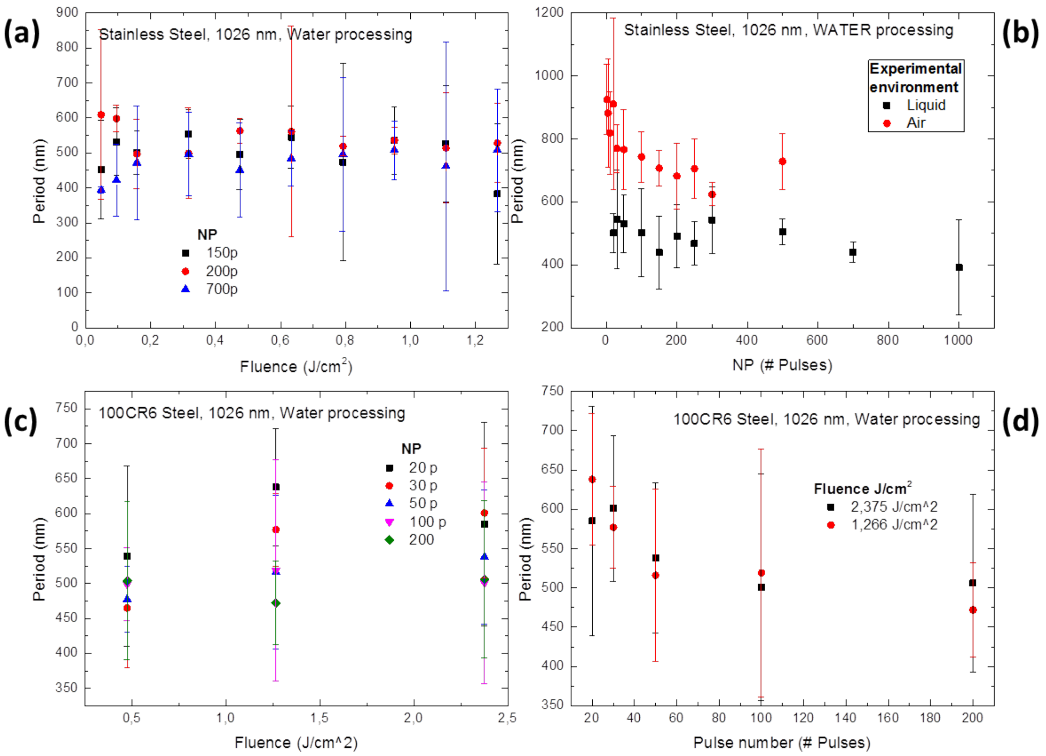

Figure 32: LIPSS periodicity in liquid processing. Ripples period decreases with NP while remains relatively unaffected with fluence.

As in the dry experiment the same trend can be noticed in the liquid experiment as it is shown in Fig. 32. In Fig. 32 (b) LIPSS period is compared between the two different experimental conditions. The same trend can be realized as indicated in the drop in ripples period. It is also shown that period values differ which is expected as discussed in the theoretical chapter (Chap 1.5). Fig. 33 demonstrates the evolution of Λ/λ as a function of NP. Ripples start to appear after NP=20 as discussed previously

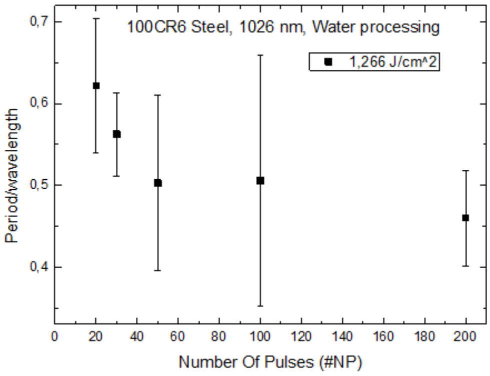

Figure 33: LIPSS periodicity in water. The much lower Λ/λ can be partly explained by the modulation of the wavelength in the presence of water.

with a period $\sim 0{,}6\lambda$ while period drops to $\sim 0{,}45\lambda$ after NP=200. By applying the scaling law that Siegman and Fauchet provided [69], $\Lambda = \lambda / n_{water}$, where $n_{water} = 1.33$ [REF VIVL]. Thus expected LIPPS period is $\Lambda = 770\ nm$, or Λ/λ now becomes $1.33 \times \frac{\Lambda}{\lambda} = 0{,}79$, and are found to be in the expected range as those seen in Fig. 33 by comparison to Fig. 27.

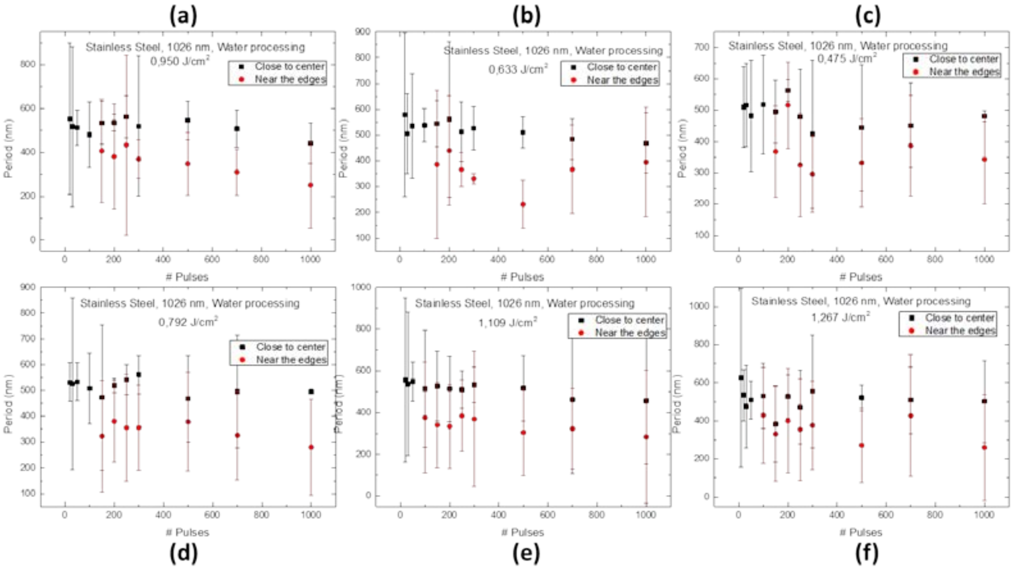

Figure 34: LIPSS periodicity as a function of NP in water environment for various fluences. Ripples with different period can me observed close to the center of the spot and near the spot edges. Ripples at the edges of the spot typically have a much lower period.

During liquid experiment ripple period modulation was observed, as in the case of the dry experiment, but this time it was observed for all fluences used. Fig. 34 demonstrates the different spacing of ripples observed close to the central region of the spot (black boxes) and near the spot edges (red dots). This is discussed in the literature [65] recently suggesting that ripples with period $\sim 0.45\lambda$ as those seen in Fig. 33 for NP=250 undergo double-splitting and ripples form with period $\sim 0.2\lambda = 200\ nm$ for 1026 nm beam, in a similar manner as the one discussed for splitting of ripples due to E-field localized effect in the dry experiment. Fig. 34 accounts for the formation of ripples with period $\sim 0.2\lambda$ for the higher NP presented.

3.3 Fabrication of large surfaces - Biomimetics

Laser irradiation can create different kind of morphologies as it has been discussed previously, depending on the accumulated number of pulses that fall upon a spot. Similarly, during laser scanning large surfaces we can calculate the effective number of pulses that irradiate a surface equal to a beam spot surface. By controlling laser scan parameters all morphological structures observed during spot by spot irradiation and presented in the morphological maps, can be produced in large surfaces.

3.3.1 Laser scan in dry environment

During irradiation in ambient air three types of morphology were realized, Ripples, microgrooves, and spikes on the surfaces of every kind of steel irradiated.

1.7131 Steel

Ripples are formed on the surface after irradiating with an effective number of pulses equal to 211 shots with a beam fluence of $1.90\,J/cm^2$, at $1.4\,mm/s$ scan speed velocity using, a line separation of $35\,\mu m$ (Fig 35, left). When the scan speed was reduced to $0.8\,mm/s$ while keeping the same line separation the effective number of pulses is 370 which results in the formation of grooves (fig. 35, right). Further reduction in the scan speed to $0.4\,mm/s$ gives rise to spike formations (Fig. 36, b). It is evident that by decreasing the Laser scan speed velocity (thus increasing the number of laser shots irradiating each area equal to the laser spot area) we can control the microstructures being formed at will in the same manner that the morphological map dictates. The effective number of pulses can also be controlled with a balanced increase/decrease of the line separation along with an adequate decrease/increase of the laser scan velocity. In this case horizontal beam overlap (directed by scan velocity) can be balanced with vertical beam overlap (directed by line separation).

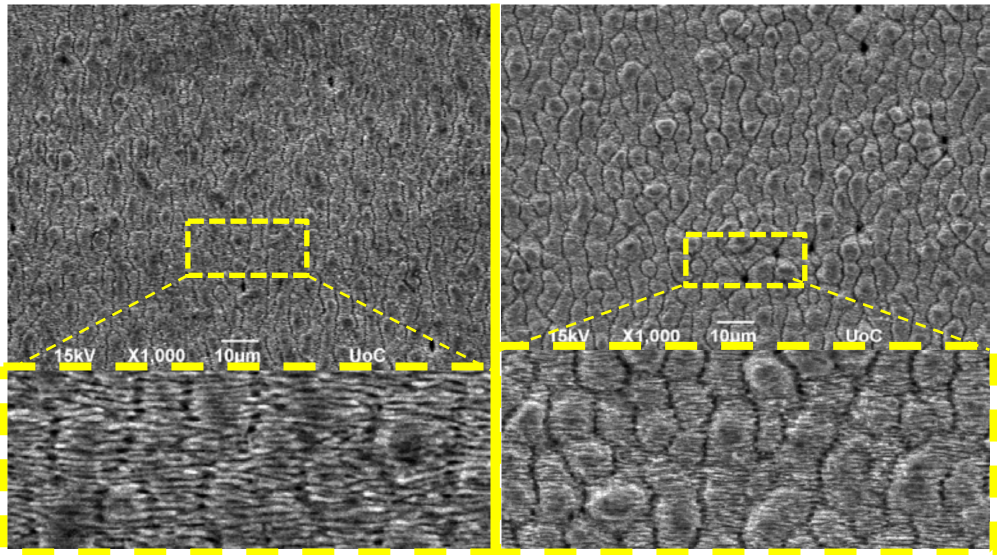

Figure 35: Large surfaces on 1.7131 Steel. Ripples (left) are fabricated with $1.90\ J/cm^2$*, at* $1.4\ mm/s$ *scan speed, line separation is* $35\ \mu m$*.* $N_{eff,2D} = 211$ *Shots. Grooves (right),* $1.90\ J/cm^2$*,* $0.8\ mm/s$ *scan speed, line separation is* $35\ \mu m$*,* $N_{eff,2D} = 370$*.*

Slight different laser scan conditions resulted in more cone shaped spikes (Fig. 36) indicating that spike dimension, shape, and spacing can be tuned. This controllability

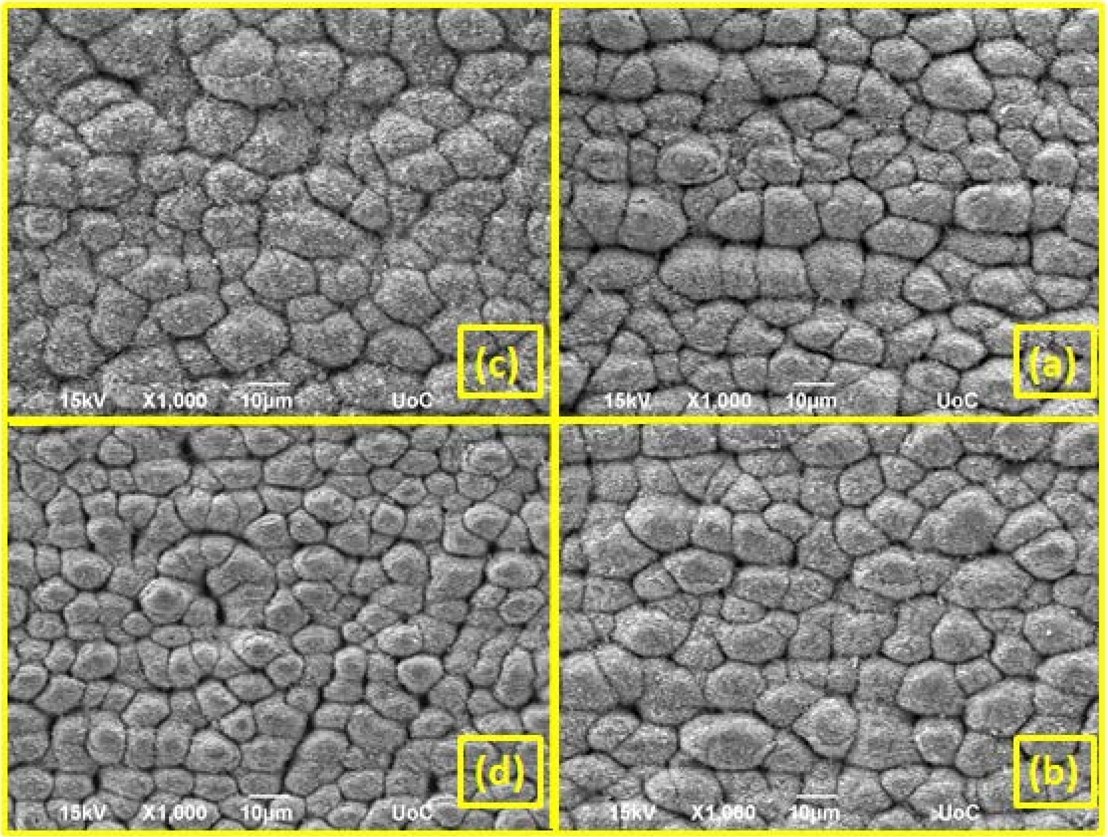

Figure 36: Large spiked surfaces on 1.7131 Steel showing a variety in micro topography. $1.90\ J/cm^2$ *(a) line step* $40\mu m$*,* $v = 0.2\ mm/s$*,* $N_{eff} = 1300$*, (b) line step* $35\mu m$*,* $v = 0.2\ mm/s$*,* $N_{eff} = 1480$*, (c) line step* $35\mu m$*,* $v = 0.15\ mm/s$*,* $N_{eff} = 1977$*, (d) line step* $35\mu m$*,* $v = 0.4\ mm/s$*,* $N_{eff} = 741$*.*

In spike formation will be discussed in a later chapter in more detail. It is worth-noting that there is a significant discrepancy in the number of pulses needed to induce formation of various structures between spot by spot fabrication and raster scan (dynamic) fabrication. This can be seen by comparing the number of pulses demonstrated in the morphological maps with $N_{eff,2D}$ for each of the observed structures. This might be linked to the vertical overlap of consecutive laser scan lines, since if the overlap is high enough, the energy might be adequately high to induce melting and modification the structures formed in the previous line. This effect becomes much more important when the aim is to fabricate surfaces with very high uniformity. This dictates that laser parameters have to be carefully fine-tuned.

<u>1.7225 Steel</u>

Large surfaces were structured on steel type 1.7225 showing all three possible morphologies, ripples, microgrooves and spikes.

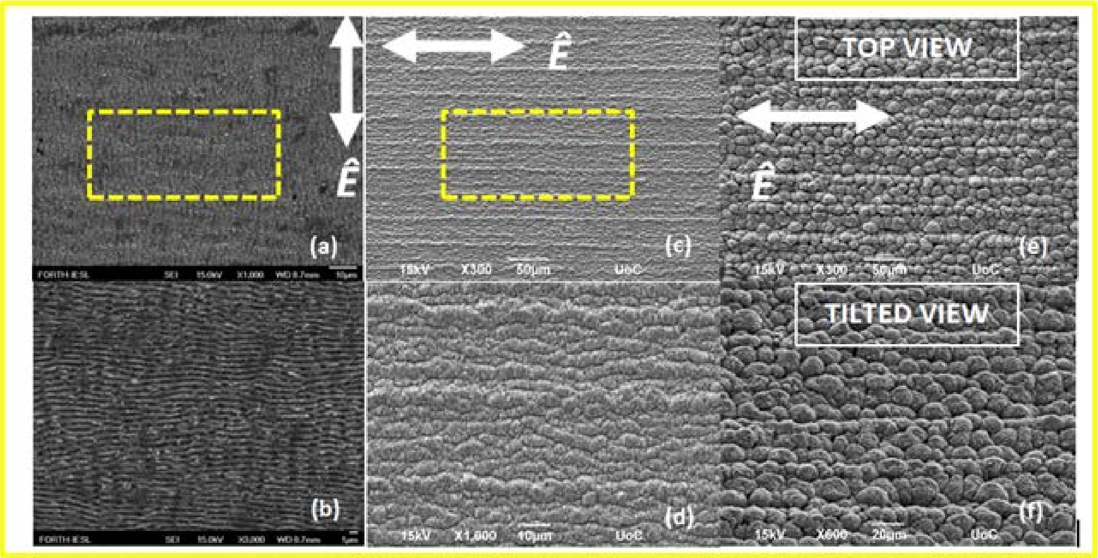

Figure 37: Different types of microstructures observed on the surface of steel type 1.7225 after laser irradiation. (a) Ripples formed after irradiation with a beam fluence of $\mathbf{0.74\ J/cm^2}$*, line separation* $\mathbf{50\ \mu m}$*, scan speed* $\mathbf{1\ mm/s}$ *,* $\mathbf{N_{eff,2D} = 77}$*, (b) higher magnification. (c) Grooves formed with a beam fluence of* $\mathbf{2.35\ J/cm^2}$ *line separation* $\mathbf{15\ \mu m}$ *and scan speed* $\mathbf{0.5\ mm/s}$*,* $\mathbf{N_{eff,2D} = 512}$ *,(d) higher magnification. (e) Top view of Spikes formed after irradiation with a* $\mathbf{2.78\ J/cm^2}$ *laser beam fluence, line separation* $\mathbf{35\ \mu m}$ *and scan speed* $\mathbf{0.2\ mm/s}$*,* $\mathbf{N_{eff,2D} = 550}$*, (f) Tilted view.*

Evidently morphological features between these two types of steel are similar. Moreover, the calculated $N_{eff,2D}$ appear to be similar. Because of the discrepancy between the numbers of pulses in spot by spot irradiation and laser scanning and since $N_{eff,2D}$ can be correlated with the formation of various structures on the surface of different kinds of steel examined, a morphological map for dynamic processing is formulated. Fig. 38 shows the induced structures as a function of fluence and $N_{eff,2D}$.

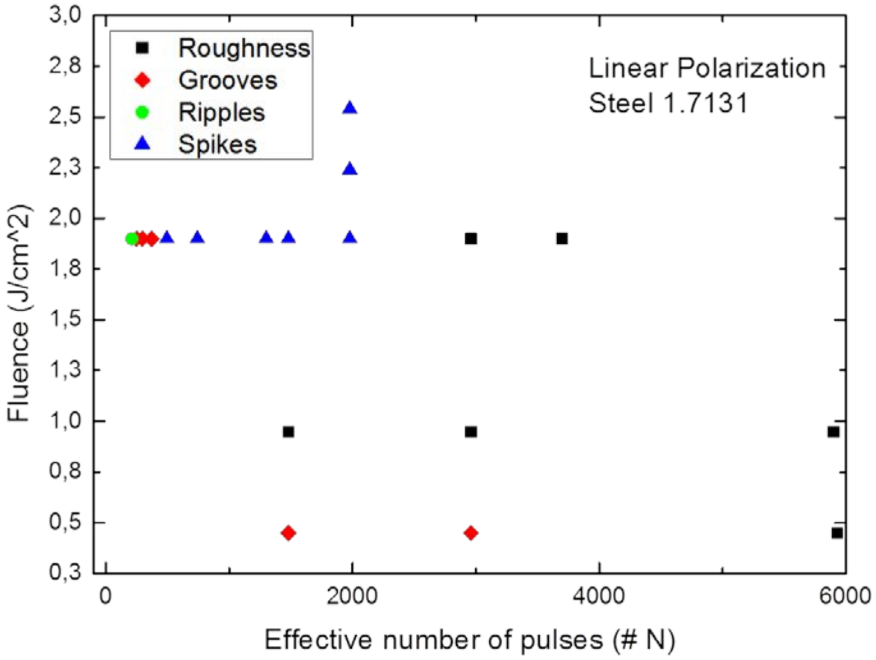

Figure 38: Morphological map of 1.7131 steel produced with laser scanning.

Stainless Steel

As for the other types of steel, using the morphological map, large surfaces were created with each of the morphological structural features observed on stainless steel.

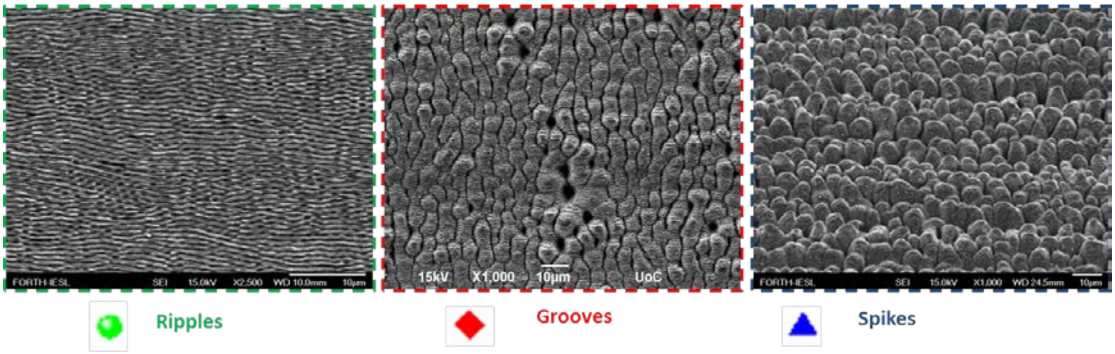

Figure 39: Large surfaces fabricated on the surface of stainless steel. Ripples (left), microgrooves (center), Spikes (right).

It has been shown that all morphological structures observed can be produced in large surfaces on all steel types experimented with in dry environment.

3.3.2 Laser scan in water environment

Stainless steel was used for large surface fabrication in water environment due to its stainless nature.

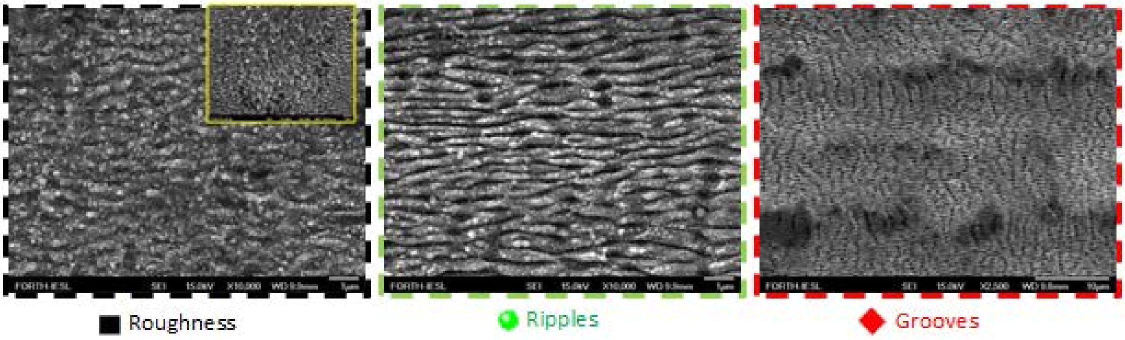

Figure 40: Large surfaces fabricated on the surface of stainless steel in water environment. Structures fabricated: High-Roughness (mushrooms) (left), ripples (center), microgrooves (right).

As during spot by spot irradiation, a much greater number of pulses was required to induce the formation of ripples and grooves under water. $N_{eff,2D}$ In the presence of water was much greater as expected.

3.4 Large surface wetting properties-Functionality

After laser treatment large surfaces created were found to have an enhanced hydrophobic behavior compared to the untreated, flat surface.

Wettability of corrugated surfaces Young's model had to be extended. Wenzel [70] and Cassie and Baxter [71] described how surface texture influences wettability. Wenzel assumed that the droplet completely wets the rough surface whereas Cassie and Baxter stated that air was trapped in the rough solid-liquid interface. Later [72], it was shown that both states could be obtained, depending on the scale of the roughness. Wetting states intermediate between the Cassie- Baxter and Wenzel states have also been reported [73–75]. The apparent contact angle (θ^*) of a liquid droplet in a Wenzel wetting state can be defined as:

$$\cos\theta^* = r cos\theta_E$$

With *r* being the roughness, defined as the ratio of the true surface area to the projected surface area and θ_E is the Young's contact angle.

In general, roughness tends to increase θ^* on a hydrophobic surface and the likelihood of a superhydrophobic wetting state. Reciprocally, the superhydrophilic wetting state is also observed by roughening an originally hydrophilic substrate [76].

Stainless Steel

Large surfaces ($5mm \times 5mm$) were fabricated both in air and under water. Fig. 41 demonstrates wetting properties of various surface morphological structures investigated using water droplet (left), lubricant oil (right).

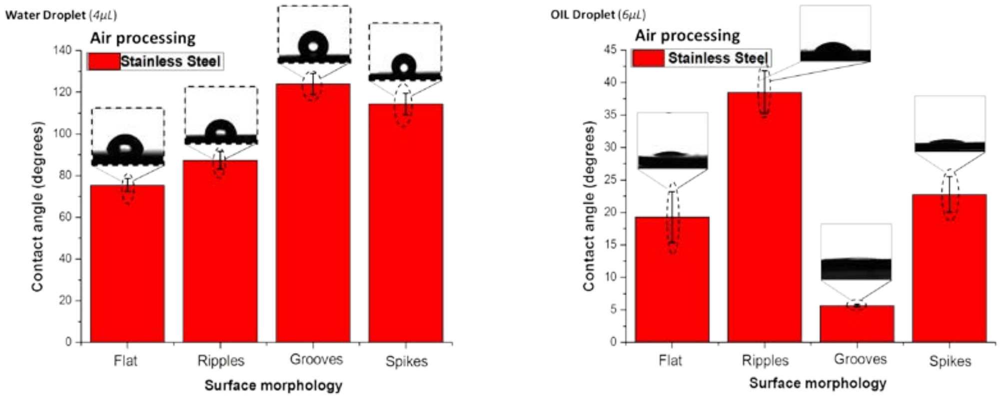

Figure 41: Contact angle measurements on the surface of stainless steel featuring various structures after dry treatment. Angles measured after applying a water droplet (left), oil droplet (right).

It can be seen that inducing morphological changes on the surface leads to an increased hydrophobic behavior of the surface. The untreated surface has a slight hydrophilic character, $C.A\ (water, flat, dry) = (75{,}46 \pm 3{,}12°)$. Rippled surface exhibits slightly more hydrophobic properties with a contact angle increase of $12°. C.A\ (water,\ ripples,\ dry) = (87{,}41 \pm 4{,}31)°$. Formation of grooves and spikes show a remarkable augmentation of hydrophobicity. $C.A\ (water, grooves, dry) = 124{,}0 \pm 5{,}0°. C.A\ (water, spikes, dry) = (114{,}35 \pm 5{,}16)°$. It has to be noticed that grooved structures appear to be slightly more hydrophobic than spikes. It can be observed that laser induced microstructures lead to an increased hydrophobicity of the irradiated surface **at the time of measurement (14 days after irradiation).**

Oil measurements show a strong oleophilic character which exhibits moderate tunability. Flat surface has superoleophilic wettability, $C.A\ (flat, oil, dry) = (19{,}3 \pm 3{,}93°)$ very similar to spiked surfaces, $C.A\ (spikes, oil, dry) = (22{,}78 \pm 2{,}75°)$. Similarly, surfaces decorated with microgrooves show an enhanced oleophilic behavior reaching contact angle as low as $C.A\ (grooves, oil, dry) = (5{,}68 \pm 0{,}17°)$. In this case the oil droplet spread on the surface almost instantly covering the surface completely. On the contrary, rippled surfaces are significantly more oleophobic than all other microstructured surfaces, although still oleophilic in nature with $C.A\ (ripples, oil, dry) = (38{,}51 \pm 3{,}28°)$. This indicates that structured surfaces lead to an increase of the already high oleophilic character of stainless steel. The only exception is microgrooves which enhance oleophobicity.

Fig. 42 demonstrates CA measurement of underwater laser treated samples. Water wettability of structures assembled underwater shows a similar enhancement towards more hydrophobicity as those assembled during dry treatment. $C.A\ (water,\ ripples,\ liquid) = (104{,}2 \pm 4{,}73)°$. $C.A\ (water,\ grooves,\ liquid) = (116{,}87 \pm 5{,}30)°$. On the contrary, high roughness surfaces decorated with micromushrooms do not seem to affect wettability.

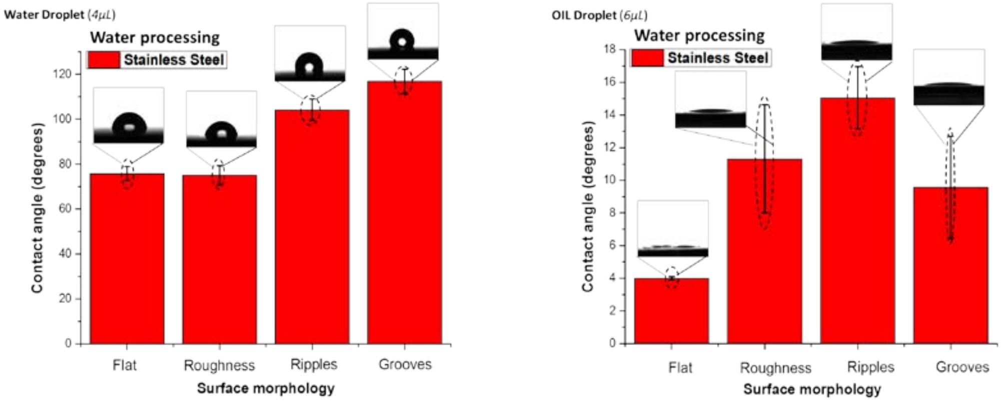

Figure 42: Contact angle measurements on the surface of stainless steel featuring various structures after underwater treatment. Angles measured after applying a water droplet (left), oil droplet (right).

Measurements with oil droplets for underwater structures also exhibit high oleophilicity as the untreated surface. Rippled surfaces show a mild increase in oleophobicity as it was observed during dry treatment.

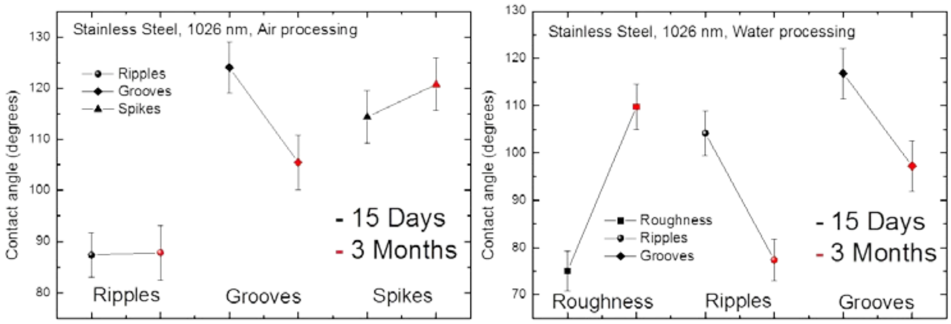

Figure 43: Contact angle measurements after 15 Days (black) 3 Months (red) demonstrating durability of the wetting properties for air processing (left) and water processing (right).

Wetting features of the fabricated surfaces appear to be durable against time. Fig. 43 presents initial contact angle measurements 15 days after irradiation (after surface stabilization) and 3 months after irradiation. Surfaces fabricated in dry experiment demonstrate a small variance of contact angle but the wetting character of the fabricated surfaces appear to be durable. The surfaces fabricated under water show a more pronounced variation of CA demonstrating both an increase (Roughness), and a decrease (Ripples, Grooves).

1.7131 Steel

Spiked surfaces were more extensively investigated on 1.7131 steel. Surfaces were fabricated using slightly different laser conditions to investigate spike diversity and possible control mechanisms.

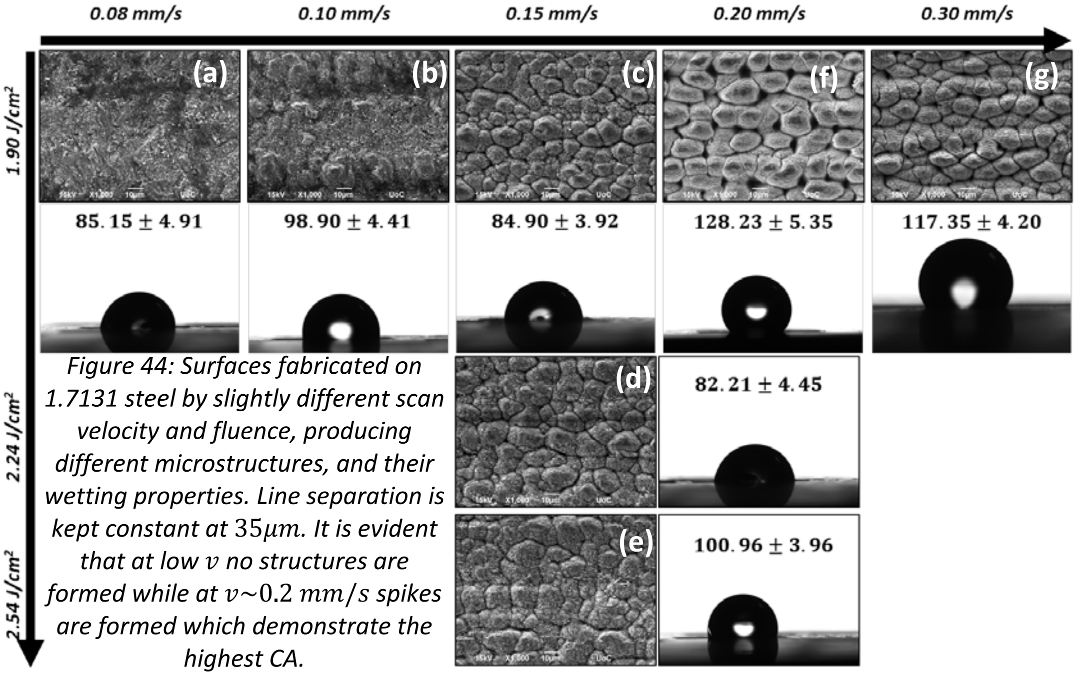

Figure 44: Surfaces fabricated on 1.7131 steel by slightly different scan velocity and fluence, producing different microstructures, and their wetting properties. Line separation is kept constant at $35\mu m$. It is evident that at low v no structures are formed while at $v \sim 0.2\ mm/s$ spikes are formed which demonstrate the highest CA.

Fig. 44 and Fig. 45 present different surfaces produced by slight adjustment of experiment parameters, while structure morphology varies accordingly. By decreasing scan speed we increase the effective number of pulses, as a consequence while at low v surfaces of high roughness are observed Fig. 44 (a), (b), increasing v leads to the formation of spikes Fig. 44 (c), (f), (g) and Fig. 45 (a), (b), (c), (f) and (g). It is also evident that spike formation is possible for a wide fluence window Fig. 44 (c), (d), (e), Fig. 45 (d) and (c). Fig. 45 (e) presents a surface produced by further decreasing peak fluence of the laser beam, in this case the fluence at the edges of the beam is not sufficient to induce surface modification thus the surface which was created is not uniform with higher modification and structure formation evident at

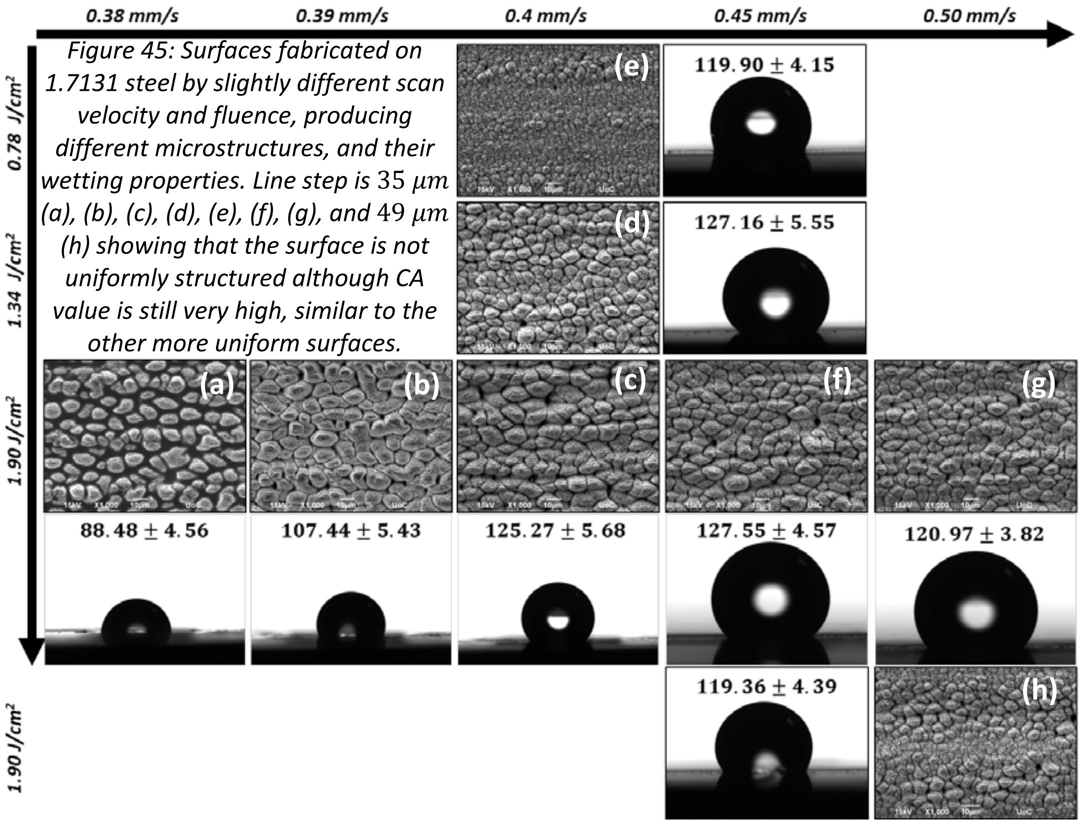

Figure 45: Surfaces fabricated on 1.7131 steel by slightly different scan velocity and fluence, producing different microstructures, and their wetting properties. Line step is $35\ \mu m$ (a), (b), (c), (d), (e), (f), (g), and $49\ \mu m$ (h) showing that the surface is not uniformly structured although CA value is still very high, similar to the other more uniform surfaces.

the region where the central region of the beam scans the surface. CA on the contrary shows similar value as the more uniform surfaces Fig. 45 (d), (c). The same effect can be seen by comparing Fig. 45 (g) with Fig 45 (h) which differ only in line separation $35\ \mu m$ (g) and $49\ \mu m$ (h). It is evident that (g) is much more uniformly structured while in (h) there are regions of high modification featuring spikes and regions in between with almost no structures. While these two surfaces differ morphologically their contact angles are similar.

3.5 Spike controllability

As it was discussed in chapter 3.3.1, spike morphology has a certain degree of tunability. One way to fine tune spike formation was found to be the *multi scan process* i.e. the laser-scan of a surface with multiple passes at the exact same laser scan parameters each of time. Two individual experiments were conducted on 1.7131 steel by this method to investigate the range of structural controllability this method can provide.

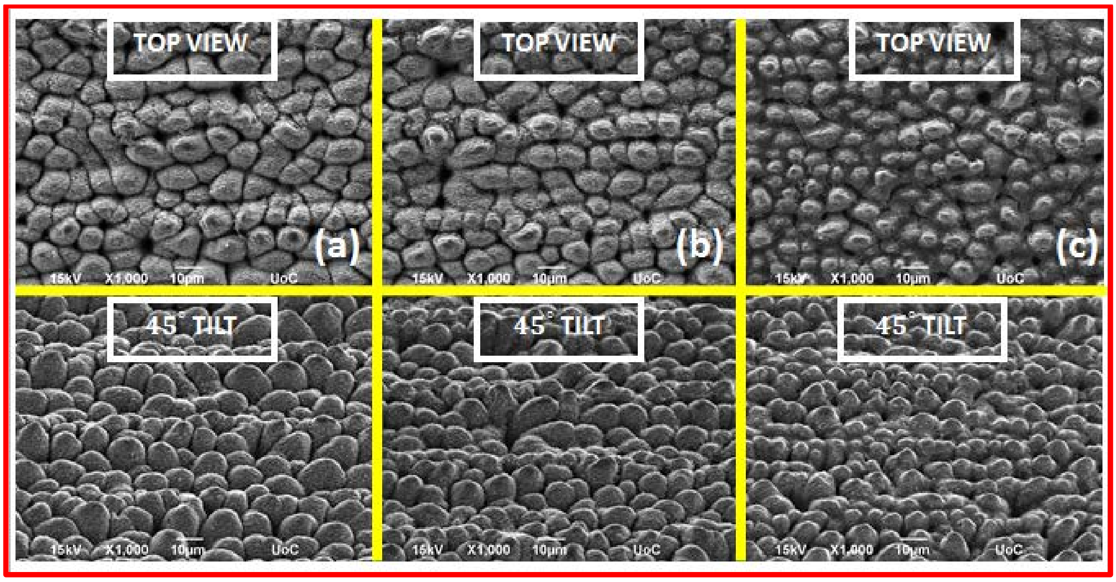

Figure 46: Self-assembled spike formation on the surface of 1.7131 steel, after laser irradiation showing structural variety. Line step is $\mathbf{35\ \mu m}$ *(a)* $\mathbf{1.9\ J/cm^2}$, $\mathbf{v = 0.4\ mm/s}$, $\mathbf{N_{eff,2D} = 741}$, *(b)* $\mathbf{1.9\ J/cm^2}$, $\mathbf{v = 0.45\ mm/s}$, $\mathbf{N_{eff,2D} = 659}$, *(c)* $\mathbf{1.3\ J/cm^2}$, $\mathbf{v = 0.4\ mm/s}$, $\mathbf{N_{eff,2D} = 741}$.

It can be seen in Fig. 46 that spikes formed vary in micro-topography depending on the individual laser condition during irradiation. Spikes in Fig. 46 (a) and (c) were fabricated with almost identical conditions using a different fluence. Higher fluence (Fig. 46 (a)) seems to lead to greater spikes and less densely packed while a reduction in fluence (Fig. 46 (c)) induces the formation of smaller sized spikes more closely arranged. Fig. 46 (b) demonstrates spikes being formed with a slightly lower $N_{eff,2D}$ which are identical to those shown in Fig. 46 (a) indicating that spike small adjustments in $N_{eff,2D}$ does not affect spike micro-topography.

Periodicity of self-assembled called microgrooves is presented on table 2.

Experimental conditions	Stainless steel	100CR6 steel
1026 nm, Air	$(1481\ \pm 89) nm$	$(1640\ \pm 134) nm$
1026 nm, Water	$(1303\ \pm 205) nm$	$(1201\ \pm 32) nm$
513 nm, Air	$(862\ \pm 339) nm$	$(2040\ \pm 36) nm$

Table 2: Microgroove periodicity calculated for two different types of steel and various fabrication conditions.

Ripples periodicity as shown previously was extensively explored, as well as spike periodicity and density. In the case of microgrooves because of their, relative to the NP range step used during experimentation, narrow existence window, their periodicity was not investigated thoroughly. Table 2 presents the microgroove periodicity for two types of steel and various fabrication methods. It appears that microgroove period is lower in the water experiment as it was found for ripples as well. On the contrary, 513 nm irradiation produced grooves with a much higher period for 100CR6 steel as opposed to those observed for 1026 nm irradiation.

MULTI-PASS LASER SCAN

Multi-pass laser scan study was conducted to investigate the range of spike micro-topography control that could be achieved. Multi-pass laser scan is realized by adjusting Eqs. 13 and 14 accordingly, to account for multiple laser scan over the same region. More specifically, we multiply the scan speed velocity calculating the effective number of pulses $N_{eff,one\ scan} = \frac{\pi \times r^2 \times f}{(n \times v) \times y}$ with the desired number of multi-scans (n), thus dividing the effective number of pulses into consecutive scan steps. After the multi-scan process the total effective number of pulses will be $n \times Neff, one\ scan = \frac{\pi \times r^2 \times f}{v \times y} = Neff$.

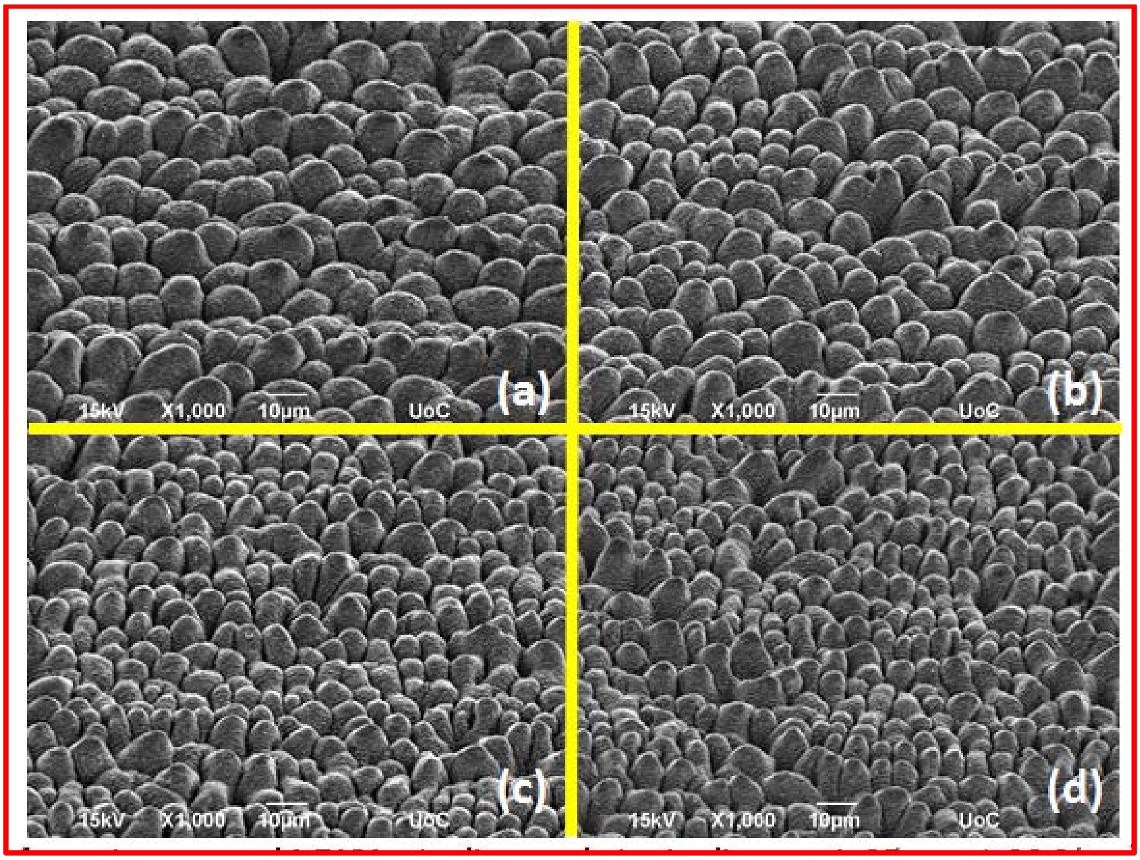

Figure 47: Spike formations on steel 1.7131 with a multi-scan process. Line separation is $35\ \mu m$*, laser beam fluence* $1.90\ J/cm^2$*. The effective number of pulses is kept constant at* $N_{eff,2D} = 741$*. (a) one step process (*$n = 1$*,* $v = 0{,}4mm/s$*), (b) double pass (*$n = 2$*,* $v = 0{,}8mm/s$*), (c) triple pass (*$n = 3$*,* $v = 1{,}2mm/s$*), (d) quadruplicate pass (*$n = 4\ \ v = 1{,}6mm/s$*). All pictures are taken with a 45 degree tilt.*

This tunability in spiked structures was further characterized demonstrating tunability towards spike periodicity, resulting in smaller sized spikes and more closely packed as the number of passes n, increases. Fig. 47 (left) shows the calculated spike period calculated as a function of number of laser passes n. It is evident that as n increases spike period decreases almost linearly. Spike height was estimated from the acquired tilted SEM images which qualitatively demonstrate a decrease in spike height, thus Fig. 47 (right) is a rough estimation of spike height and cannot be used to extract certain quantitative conclusions, although spike height shows a sharp drop with increasing number of passes.

The formation of micro-cones (spikes) has been reported repeatedly on the surface of steel types [65, 68, 50]. Contrawise, the multi-pass process can be found in a few works in the literature [12], where is was found that increasing the effective number of pulses with a multi-scan procedure or splitting the effective number of pulses into separate laser scan passes, both resulted in a tunability in spike micro-topography.

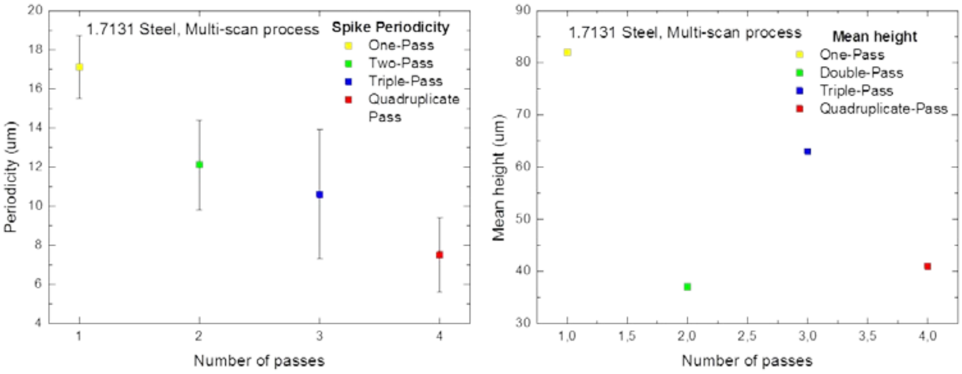

Figure 48: Spike features after multi-pass process. (Left) Spike periodicity calculated for one pass, double pass, triple pass and quadruplicate pass demonstrating a constant drop in spike periodicity. (Right) Spike mean height estimation showing a sharp drop as the number of passes increased. Since spike height is calculated from SEM images this calculation is mostly qualitative.

Surfaces created with the multi scan procedure demonstrate an increased hydrophobic trait compared to the untreated material. It is shown that contact angle obtained does not vary as n increases but all surfaces created this way have similar CA.

Two different experiments were conducted fabricating surfaces implementing the multi-scan procedure. Experiment #1 presented in Fig. 49 and Experiment #2 Fig. 50.

Results between the two individual experiments appear similar although surfaces fabricated in the second experiment appear more uniform.

Laser conditions uses in order to create these surfaces are presented in Fig 47. It is evident that multi-scan process although affects spike periodicity and spike height, contact angles seem to be unaffected with this method.

Oil wetting properties remain mostly unaffected with laser treatment implying that oleophobicity/oleophilicity contrarily to hydrophobicity/hydrophilicity cannot be controlled by corrugating surfaces and inducing surface structures the same way.

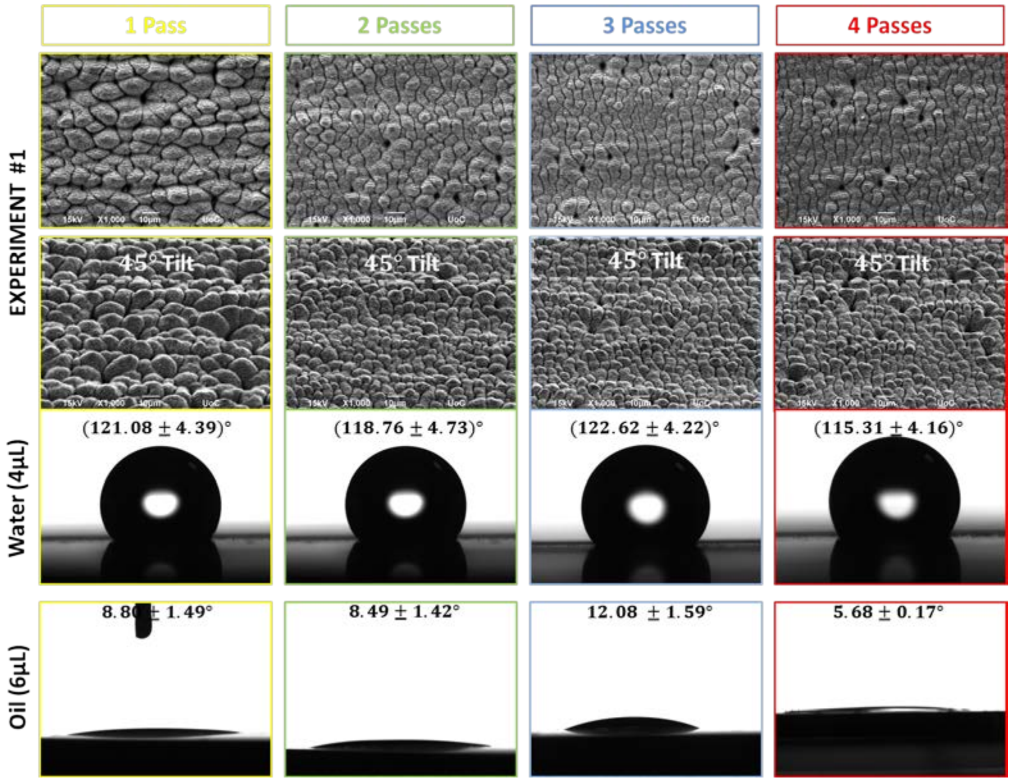

Figure 49: Experiment #1: *Multi-pass surfaces fabricated with the laser condition presented in Fig. 47, and their wetting properties with water and oil droplets presenting high water contact angles and very low oil contact angles.*

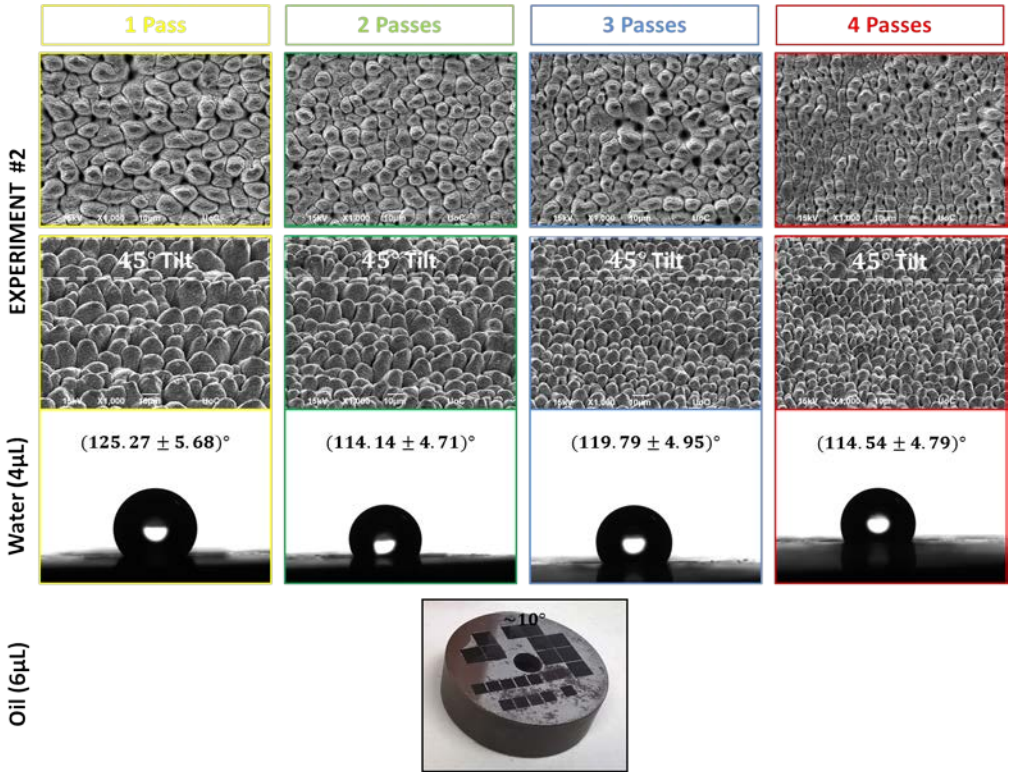

Figure 50: Experiment #2: *Multi-pass surfaces fabricated and their wetting properties with water and oil droplets presenting high water contact angles and very low oil contact angles, as it was observed on the surfaces of Experiment #1.*

It is noteworthy that spikes formed on the fabricated surfaces exhibit smaller scale structures on their body, featuring ripple-like formations and small protrusions, thus creating hierarchical structures both at the micro (spikes) and nano (protrusions) scale. Both of these formations contribute to the total roughness of the surface. Fig. 51 presents SEM images of spiked surfaces demonstrating hierarchical structures at low (a), (c) and at high (b), (d) magnification. These nano-scale formations appear on spikes both after single step laser scanning Fig. 51 (a), (b) and multiple scanning process (c), (d).

Figure 51: Spiked surfaces fabricated in single step (a), and multiple scan step (c) process. High magnification images (b), (d) demonstrate nano-scale structures on individual spikes.

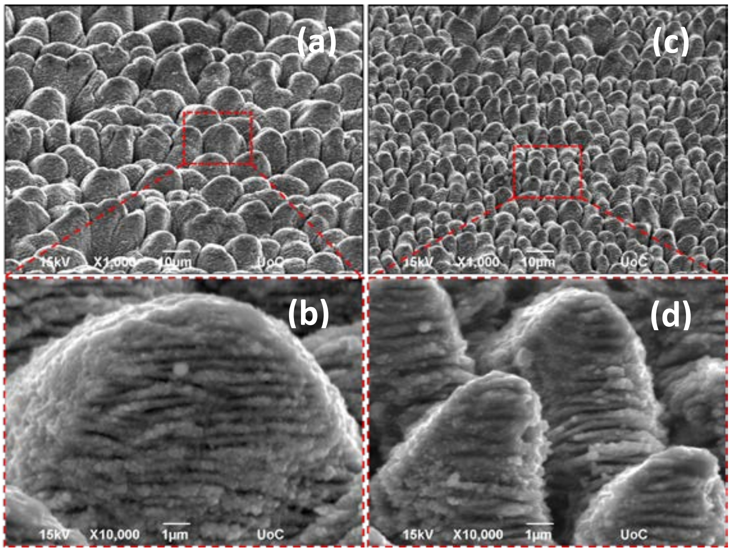

CA measurements on 1.7131 steel were conducted 15 days and 3 months after irradiation to test the stability of the wetting properties. Contrary to stainless steel, hydrophobic surfaces on 1.7131 seem to deteriorate with time.

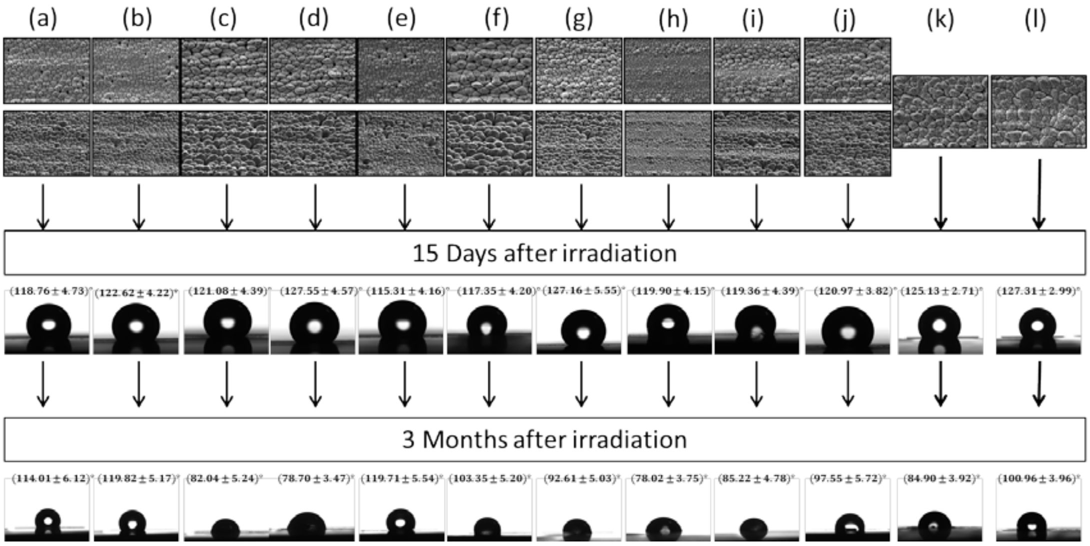

Figure 52: Wetting properties on the surfaces of 1.7131 measured after 15 days and 3 months after irradiation. Contact angles after 3 months are significantly lower on all but one (e) of the surfaces. Surfaces (a), (b), (e) are created with the multiple-scan process.

A possible explanation is the appearance of signs of corrosion on material, with clear marks of rust.

Fig. 52 presents CA measurements showing a significant drop in angles measured after 3 months. It is evident that CA decrease is profound for most surfaces (c), (d), (f), (g), (h), (i), (j), (k) and (l) while there is a slight decrease (a), (b) and increase (e). The surfaces which demonstrate the greatest durability are the ones fabricated using the multi-scan procedure. Fig. 53 presents CA durability as a function of n showing

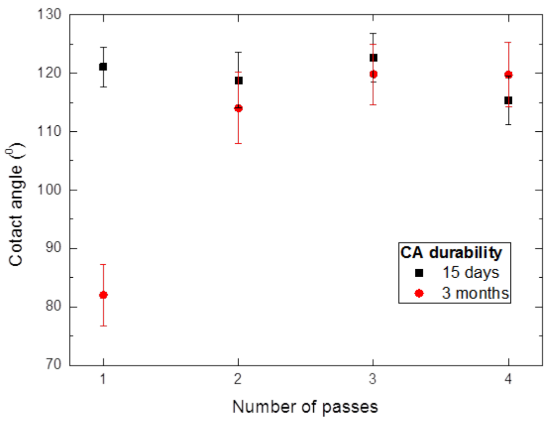

Figure 53: CA durability 3 months after irradiation for surfaces treated with multi –pass laser scan. Treated surfaces with more than one passes show greater durability compared to the single step process.

That multiple-scan procedure fabricated surfaces demonstrate very good durability against time compared to the single step fabrication process.

3.6 Tilted incidence processing

A set of experiments was conducted with various angles other than normal incidence. This set of experiments was done on stainless steel and 100CR6 steel to test the possible similarities and differences of this fabrication method and to check the variance of the periodicity of the produced structures as well. Spot by spot and line scanning procedures were implemented and the formed structures were compared to those formed after normal incidence irradiation both qualitatively (morphological comparison) and quantitatively (periodicity study).

3.6.1 Spot by spot processing

Stainless steel samples were irradiated with a varying train of pulses for different incident angles. As for normal incidence microstructures form spontaneously on the irradiated surfaces featuring both ripples, grooves and spikes.

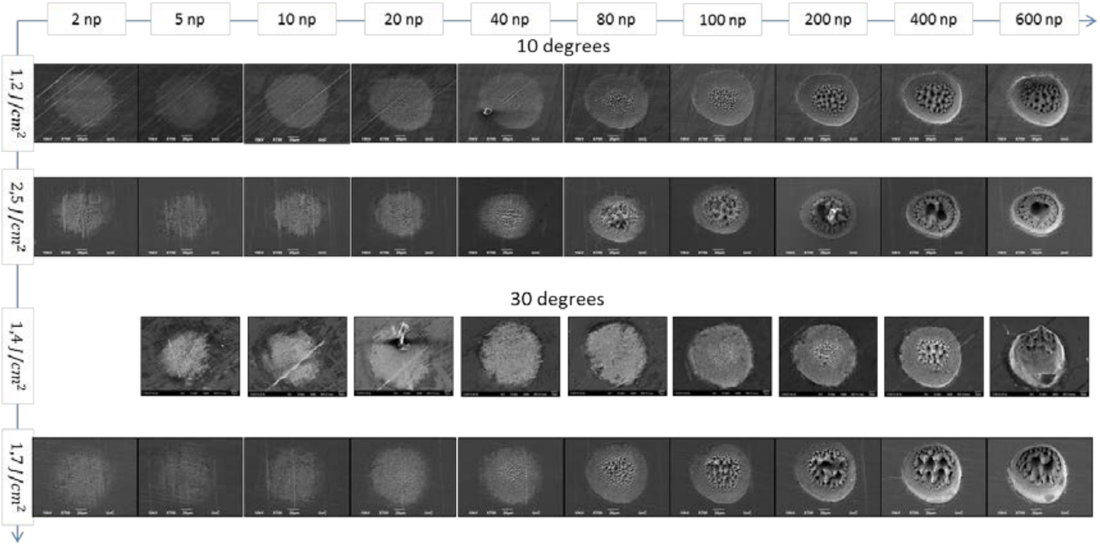

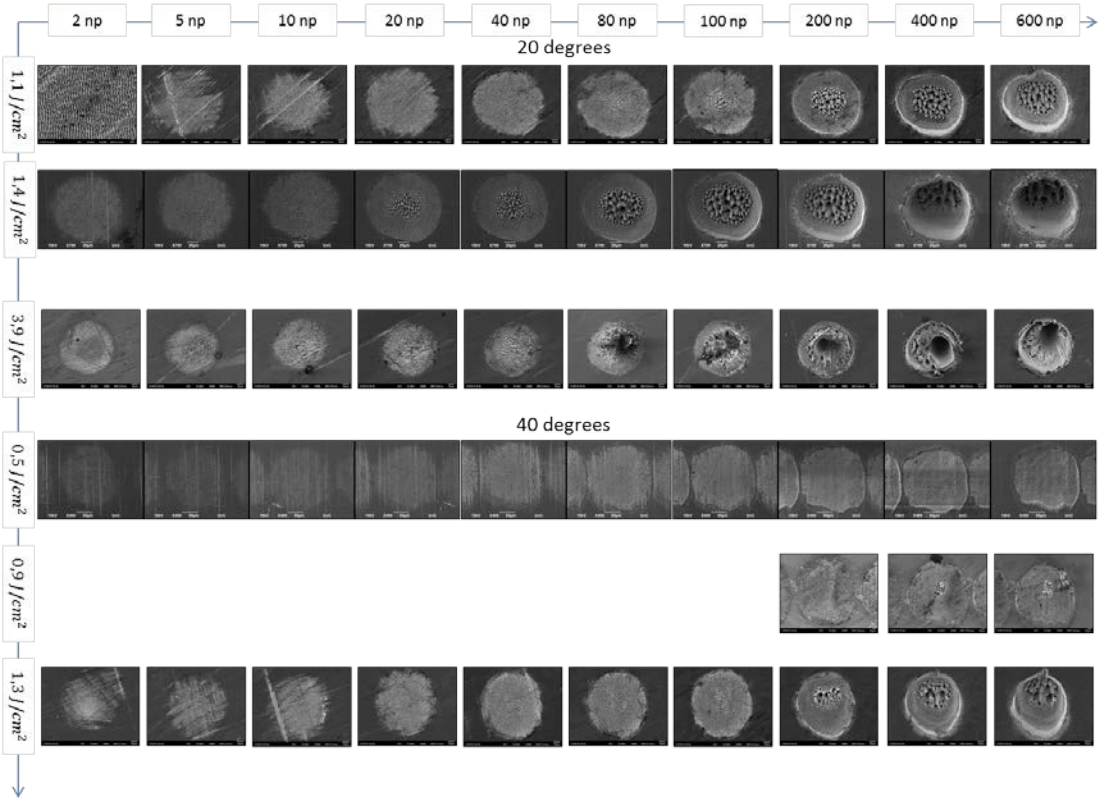

Figure 54: Laser spots on the surface of stainless steel after irradiation with 10, 20, 30 and 40 incident angle tilt. Microstructures form on the surface of the material as it was observed after normal incidence. On the contrary, formation of periodic structures becomes slower as the incidence angle becomes shallower. Furthermore, the beam spot obtained after irradiation with shallow angles acquires an elliptical shape compared to normal incidence.

Fig. 54 presents laser spots obtained for $10^{\circ}, 20^{\circ}, 30^{\circ}$ and 40° incidence angles for various number of pulse packets and fluencies. Periodic formations observed after normal incidence irradiation are now formed as well. It is evident that as the angle of incidence increases higher fluence and NP is needed to induce the formation of microgrooves/microspikes. This is reported in the literature [12] and is explained because of the deformation of the beam fluence due to the varying distance between the lens and each point of the target in the laser spot area. This variance becomes greater as the angle becomes shallower leading to a decrease of the beam fluence.

It is also noted that the microstructes formed (grooves, spikes) tend to align themselves to the incident beam direction which is shown in Fig. 55. This has also been reported previously in reff [12]. While this effect is evident for spikes and microgrooves, it is not seen in the formation of ripples.

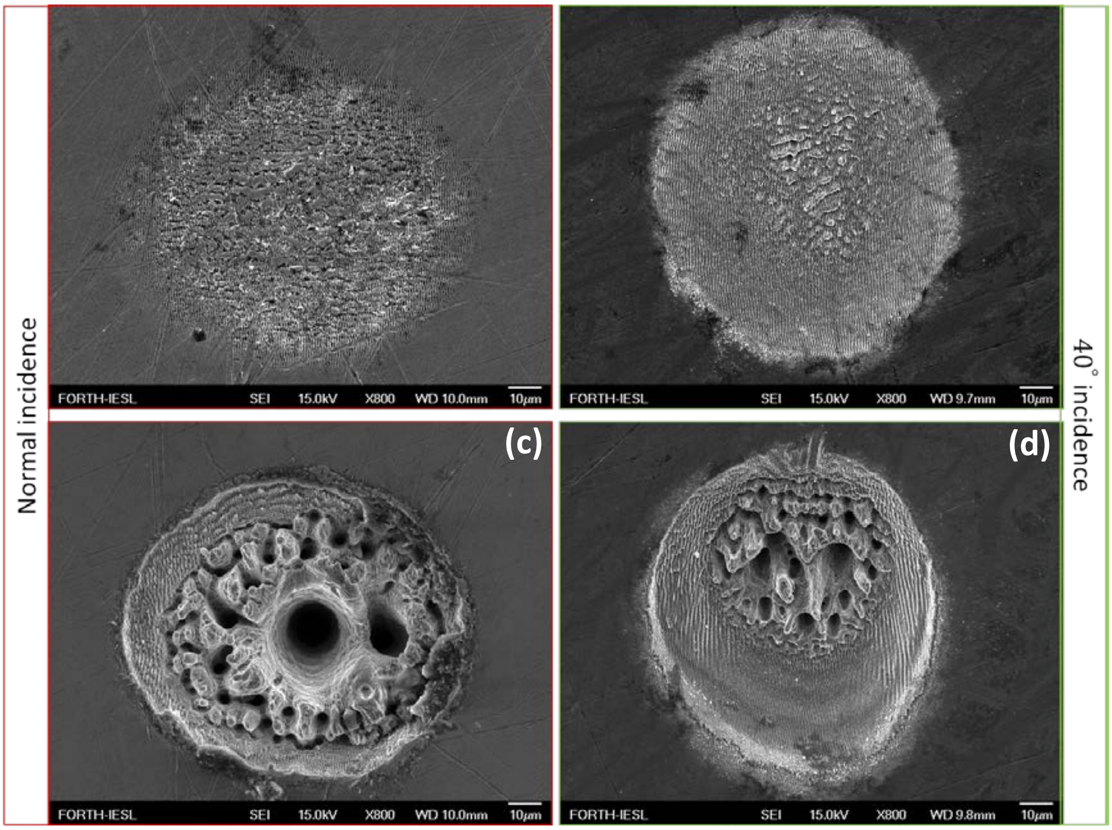

Figure 55: SEM images demonstrating *spots on stainless steel after irradiation with normal incidence (b), (d) and* 40° *incidence (a), (c). Comparing microstructures in the two individual fabrication procedures demonstrates the alignment of the produced structures with the incident beam direction for both spikes (c), (d) and microgrooves (a), (b).*

This is presented in Fig. 55 for microspikes (c), (d) and microgrooves (a), (b). Ripple's hill compared to spike's peak, is much less high making it more difficult to observe if ripples also align to the incident beam (Fig. 56, 58).

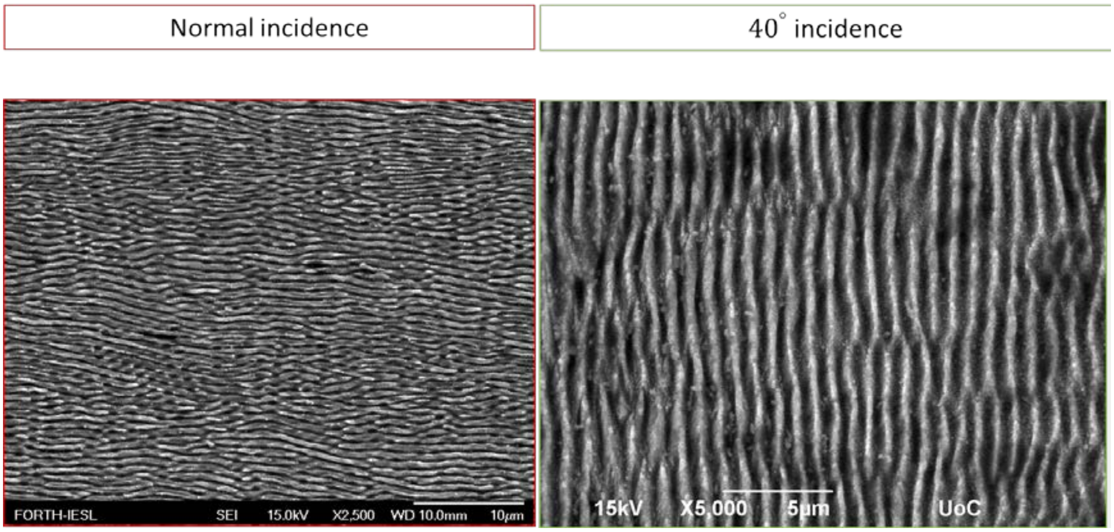

Figure 56: SEM images comparing ripples formed after normal incidence and 40° incidence.

Moreover, laser spots obtained after angled irradiation resemble the shape of an ellipse compared to the circular shape of laser spots after normal incidence as mentioned before. This elliptic character becomes more pronounced as ϑ increases.

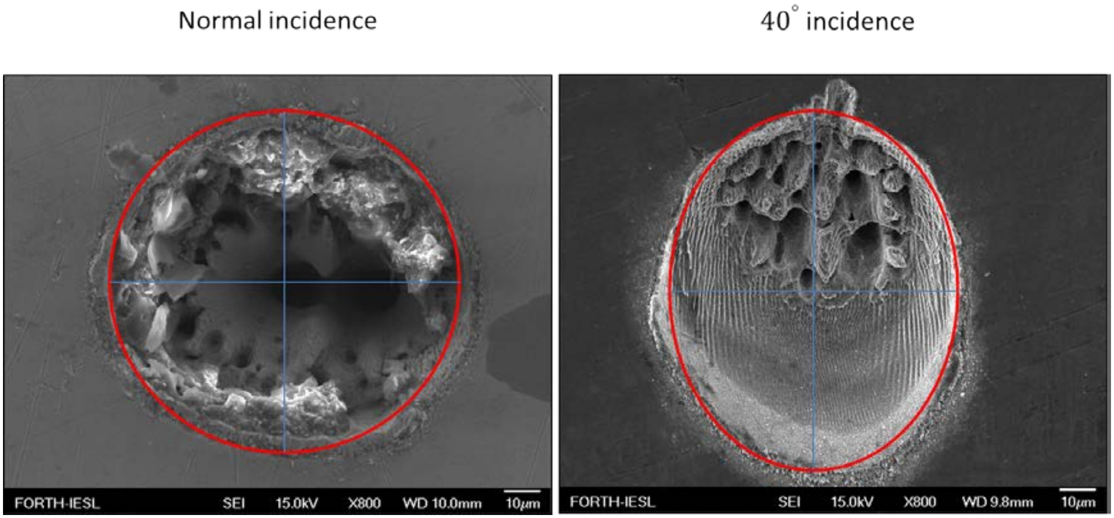

Figure 57: Laser spot shape obtained after irradiation under normal incidence (left), and 40° angled incidence (right).

Fig. 57 Presents laser spots taken after 600 pulses with normal incidence and 40° angled incidence which corresponds to the two extreme conditions in this set of experiments. To measure the deformation of the spot, the diameter of each spot was measured two times in perpendicular directions. For the elliptic spot the major and minor axes were selected. The ratio of the two diameters was then calculated as quantification of the degree of ellipticity of each spot. Thus, a value of 1 would be a perfectly circular spot. Table 3 summarizes the calculations for the two laser spots indicating an increase in ellipticity for the angled spot compared to the normal incidence spot.

Normal incidence			**40° incidence**		
$R_{parallel}$	$R_{perpendicular}$	$\frac{R_{perpendicular}}{R_{parallel}}$	$R_{parallel}$	$R_{perpendicular}$	$\frac{R_{parallel}}{R_{perpendicular}}$
104.2 μm	92.4 μm	0.89	84.2 μm	103.3 μm	0.82

Table 3: Degree of ellipticity calculated for 0 and 40 degrees of angle of incidence.

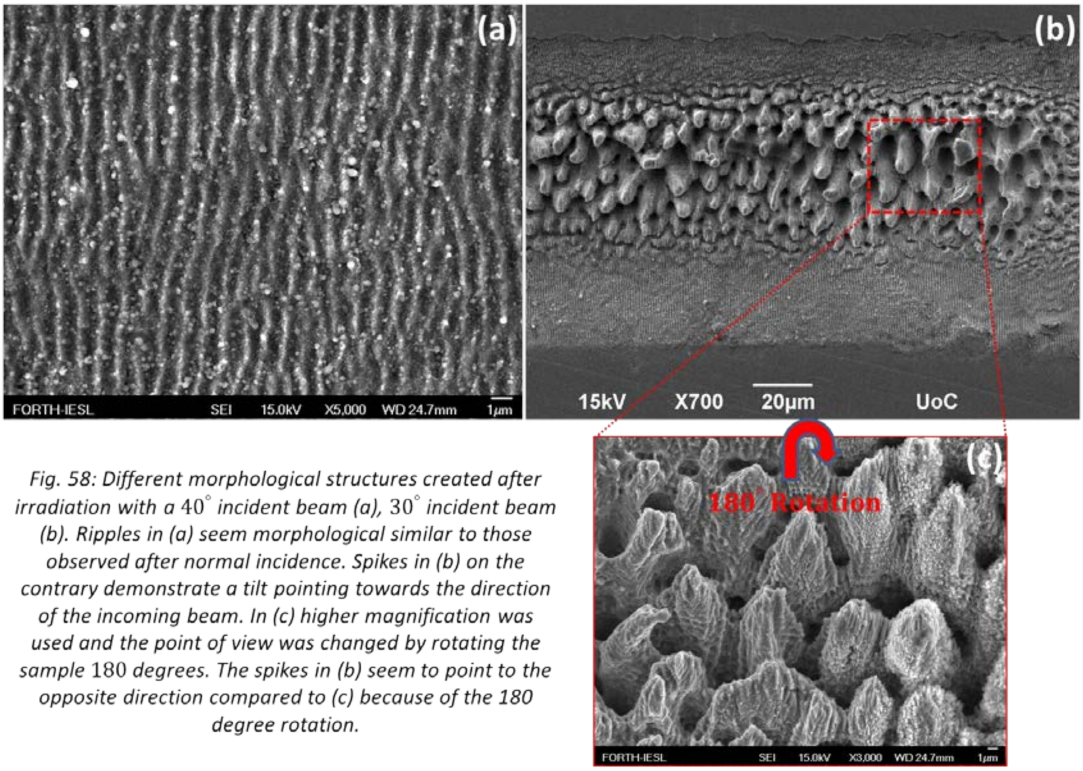

Fig. 58: Different morphological structures created after irradiation with a 40° *incident beam (a),* 30° *incident beam (b). Ripples in (a) seem morphological similar to those observed after normal incidence. Spikes in (b) on the contrary demonstrate a tilt pointing towards the direction of the incoming beam. In (c) higher magnification was used and the point of view was changed by rotating the sample* 180 *degrees. The spikes in (b) seem to point to the opposite direction compared to (c) because of the 180 degree rotation.*

Spot by spot analysis also reveals that LIPPS period is affected by incidence angle ϑ which is discussed from a theoretic point of view, and its effect on LIPPS period is given by Eq. 1. This modulation of LIPSS period has been reported earlier in the literature [90, 91].

Fig. 59 presents period measurements for the spots presented in fig. 54. LIPPS Period tends to increase as the angle of incidence increases beyond zero degrees. Nonetheless LIPPS period still decreases as NP increases but this effect seems to be less profound for steeper angles. Fig. 59 (a) demonstrates period as a function of NP for 10 degrees incidence angle. It can be seen that period drops sharply as NP starts to increase progressively from 2 to 80. A similar effect can be seen for 20 degrees, on the contrary this effect in not so profound for 30 and even less for 40 degrees where period seems to be unaffected by NP and LIPSS period remains fixed. This is also evident in Fig. 60.

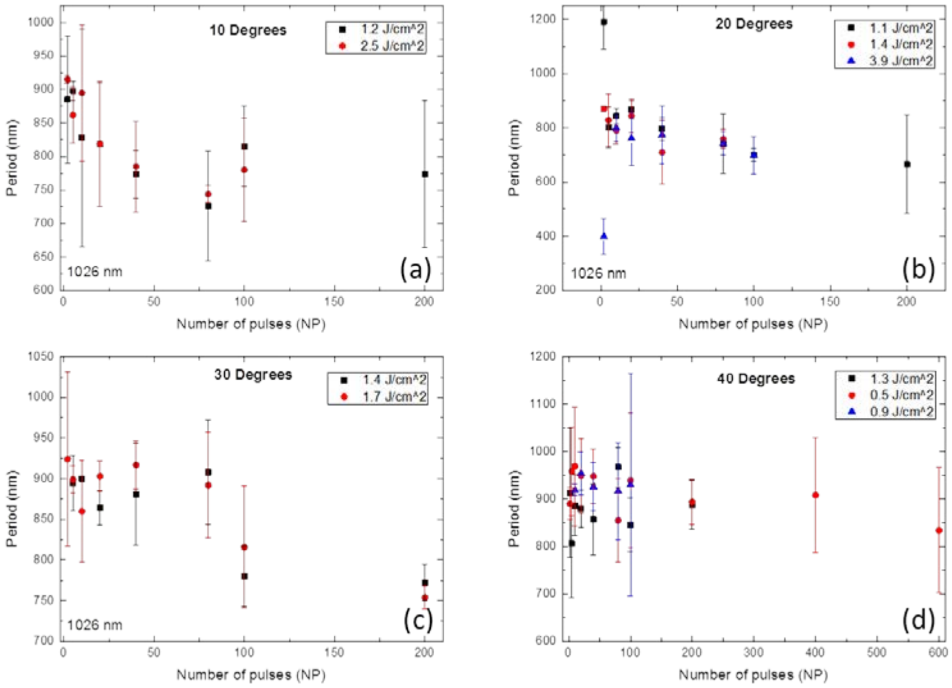

Figure 59: LIPSS periodicity for different angles of incidence as a function of NP. 10 (a), 20 (b), 30 (c) and 40 (d) degrees are shown.

It is also evident that as θ increases, LIPPS period increases. This is demonstrated in Fig. 60 where LIPSS period is plotted for 0, 10, 20, 30 and 40 degrees.

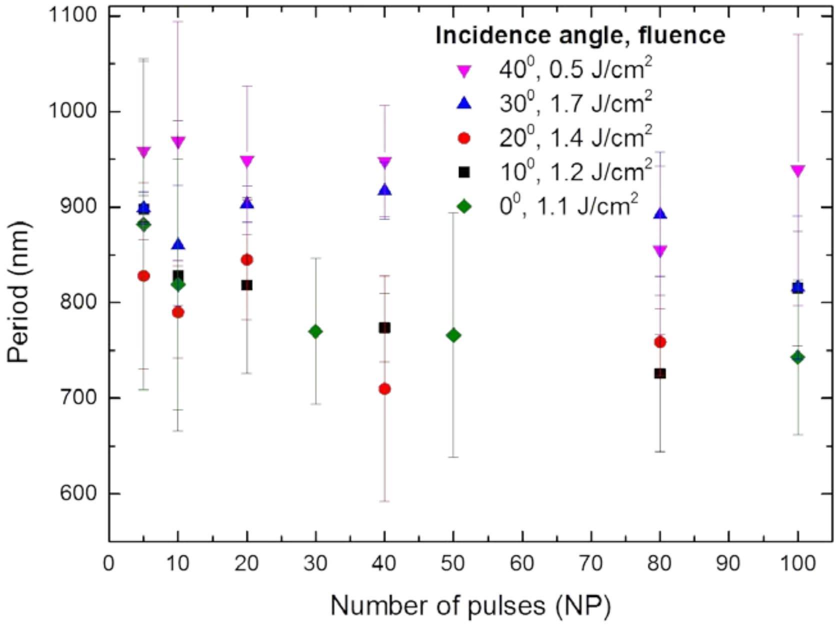

Figure 60: LIPPS periodicity comparison after irradiation with 0, 10, 20, 30 and 40 degrees of incident angle. It can be observed that period increases as θ increases.

3.6.2 Line scanning processing

Lines were scanned with various laser scan velocities and at various angles of incidence for both types of steel.

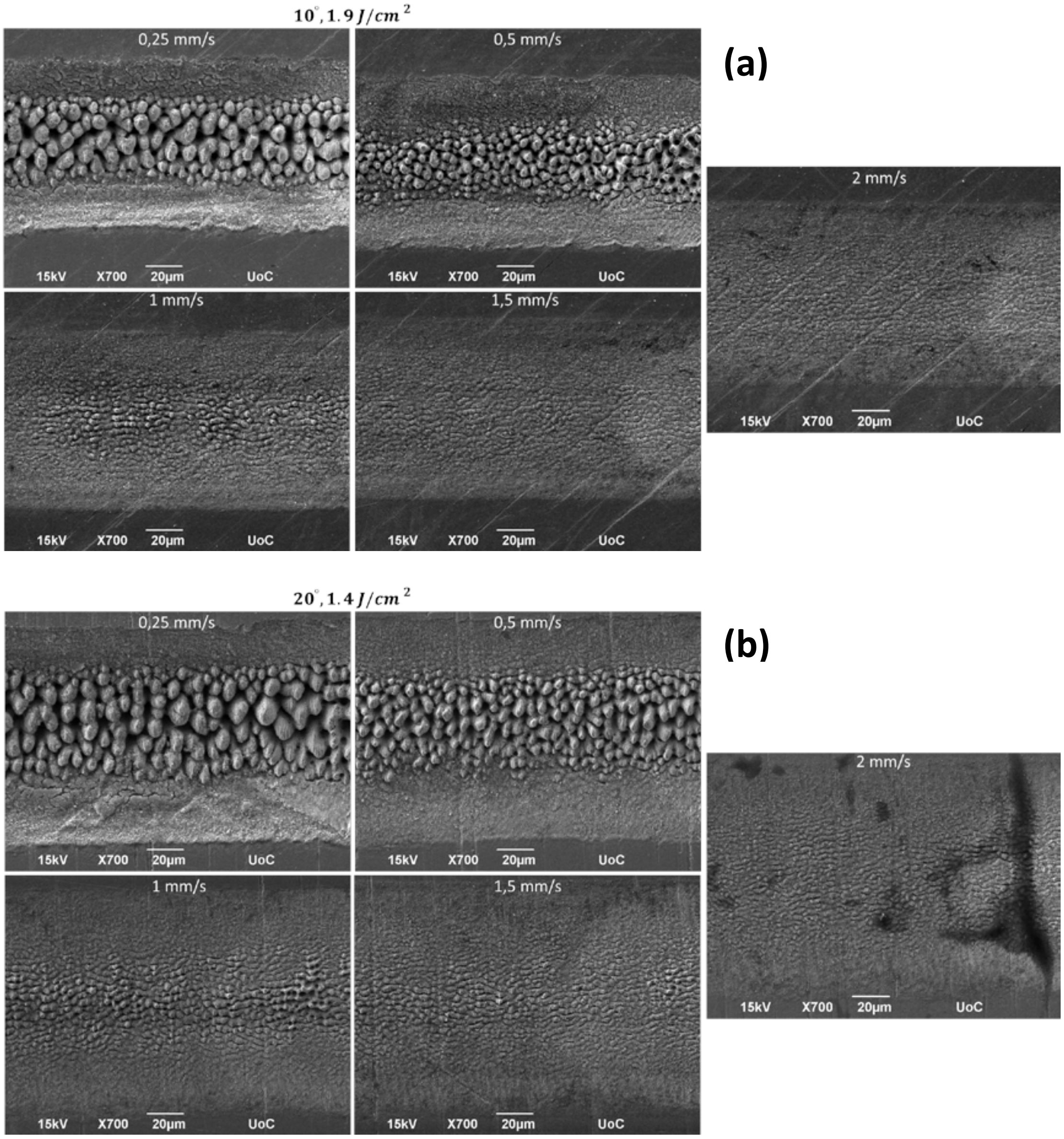

Figure 61: Line scans on the surface of stainless steel at 10 and 20 degrees of incidence. Three morphological features are realized, ripples, grooves and spikes.

At 10, 20 and 30 degrees all known morphological features can be easily produced by varying the laser scan velocity. Spikes and ripples are tilted to coincide with the incident beam direction as was observed during static irradiation. For 40 degrees inclination morphological features are harder and slower to form thus the largest space of the irradiated area is covered with non-periodic high roughness features instead of LIPSS. Cracks also appear after irradiation with a lowest scan speed

($0.25\ mm/s$) possibly indicating the appearance of crystal defects. These cracks also appear after repetitive irradiation with a great number of pulses but are confined to a lesser area (fig. 61 (a) $0{,}25\ mm/s$).

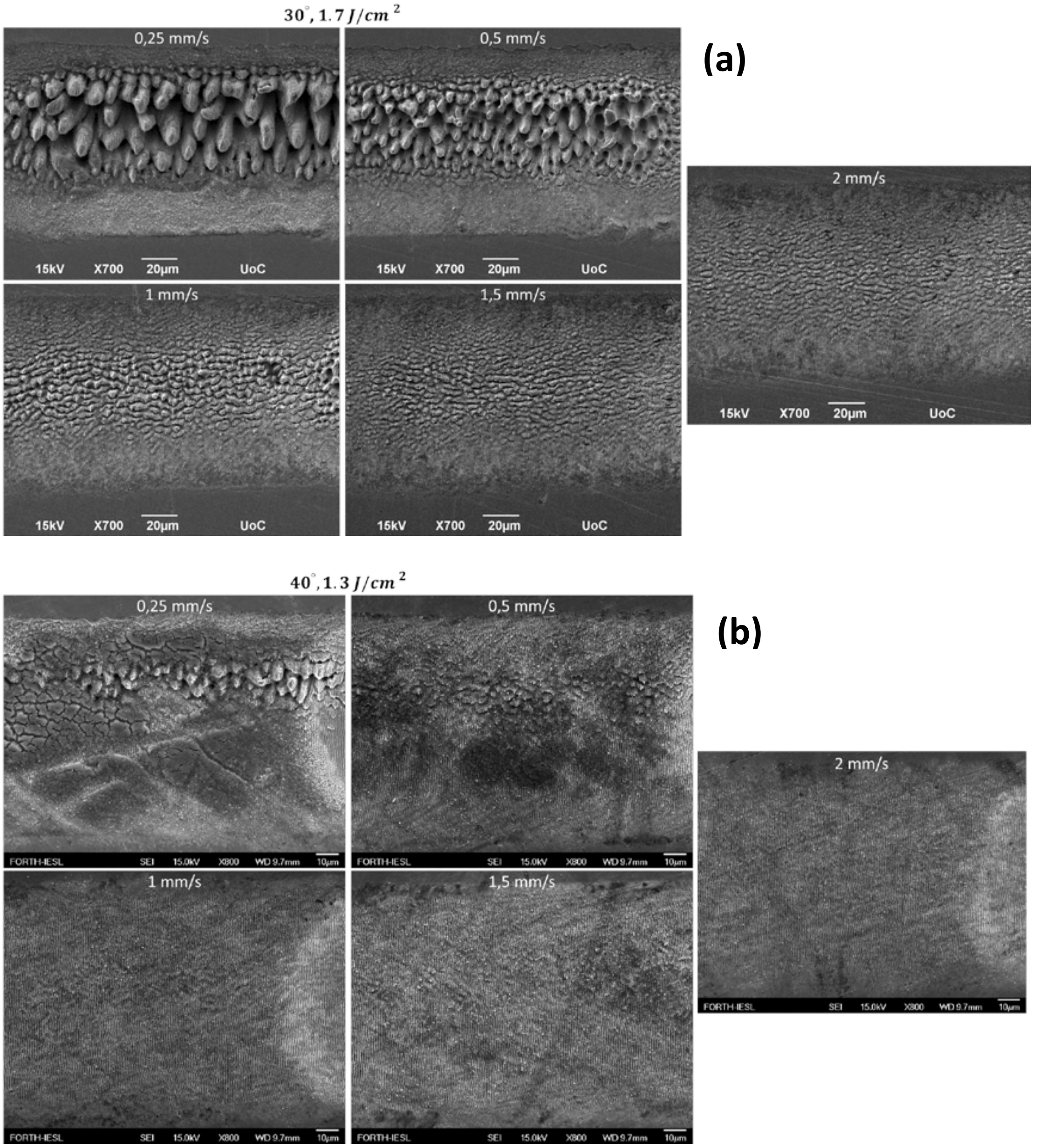

Figure 62: Line scans on the surface of stainless steel at 30 and 40 degrees of incidence. The same three morphological features are realized, ripples, grooves and spikes. It can be seen that spikes hardly form and are located at a very confined area.

On the surface of 100CR6 steel, even shallower angles were used during one dimensional laser scan procedure. Fig. 63 presents morphological comparison between grooves and ripples formed after laser scanning with 0, 20, 40 and 60 degrees of angle of incidence. It can be seen that periodicity is affected as the angle of incidence increases from 0 degrees to 60, as it was observed for stainless steel samples.

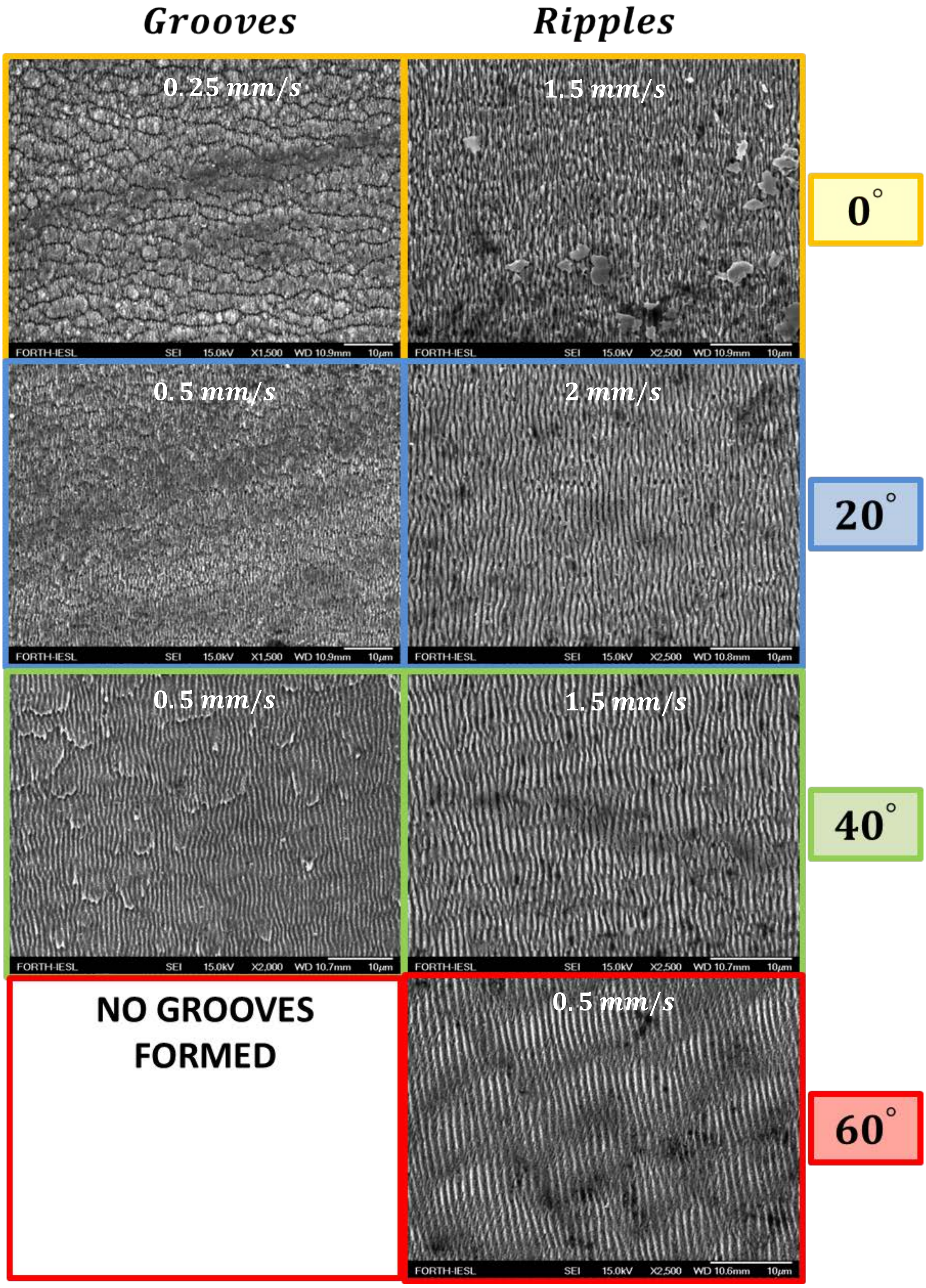

Figure 63: Line scans on the surface of 100CR6 steel at 0, 20, 40 and 60 degrees of incidence. Ripples are formed each of the times while grooves don't appear after the sample is tilted at 60 degrees. A significant shift in LIPPS periodicity can be realized.

By reducing even more the laser scan speed, a greater effective number of pulses is achieved thus inducing the formation of well-formed periodic spikes even at 40 degrees. At higher angles no such structures can be observed.

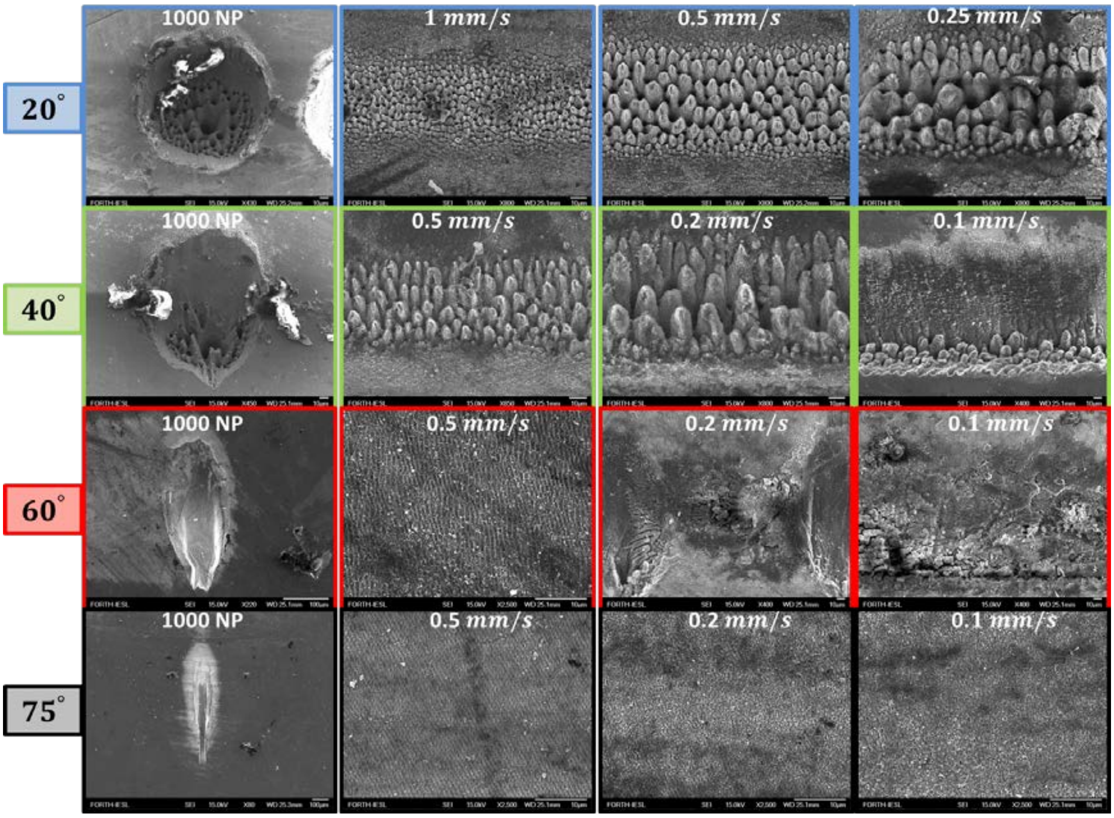

Figure 64: Laser spots after irradiating with a train of 1000 pulses and line scans on the surface of 100CR6 steel at 20, 40, 60 and 75 degrees of incidence at slow laser scan velocities. The laser spot is deformed and becomes an ellipse as ϑ increases.

Fig. 64 presents laser spots after 1000 shots at various angles of incidence. It can be seen that the damage pattern becomes elliptical which can be seen for θ=40. This effect becomes more profound at θ=60. At the most steep angle θ=75 the damage pattern resembles a line. It is noteworthy that the ablation mark shifted from the center of the spot and is limited to the edge of the spot which indicates local fluence fluctuation; also the intensity profile is distorted compared to normal incidence.

Conclusions

In this Thesis various types of steel were experimented upon. At first each target was irradiated with a preset pattern of number of pulses at various fluences and the induced microstructures were mapped as a function of NP and fluence. The period of laser induced periodic surface structures observed was studied and found to be dependent on the number of pulses used to induce their formation and angle of incidence. Furthermore large surfaces featuring each of previously observed morphological structures were fabricated. Wetting experiments on the fabricated surfaces demonstrated an acquired biomimetic augmentation of hydrophobicity of the treated surfaces compared to the flat surface. Oil measurement showed an increase towards oleophobicity only for rippled surfaces. Finally, a method to manipulate spike micro-topography was presented and investigated, which showed an increase in spike periodicity as the total effective number of pulses was split to individual laser scan procedures while CA measurements between such surfaces were similar.

Acknowledgements

Firstly, I would like to express my special thanks to my supervisors Dr. Stratakis Emmanuel and Associate Professor George Kioseoglou, for giving me the opportunity to work on this project and for guiding my experimental work. I also owe gratitude to Prof. Dimitris Papazoglou, and Dr. Panagiotis Loukakos for agreeing to evaluate this work.

Also, special thanks to Evangelos Skoulas for training me to begin with, and for providing invaluable insight to my experiments. Dr. George Tsibidis who develops the theoretical framework to explain our experimental results, Alexandra Manousaki for the endless hours in Scanning Electron Microscopy, Andreas Lemonis for his technical expertise that made everything possible, and Antonis Papadopoulos for the collaboration we had especially on our early experiments and during the long hours of studying.

I would also like to thank the academic staff of the Materials Science & Technology department and all the *Ulmnp-lab* individuals for the beautiful collaboration we had during this productive and challenging time.

Furthermore, I want to express my gratitude to my friends and family for the support, understanding, and happy moments.

Finally, I would like to thank Eva for bringing color to my life during this special period.

List of Figures

List of Tables

References

1. S.I. Dolgaev, J.M. Fernandez-Pradas, J.L. Morenza, P. Serra, G.A. Shafeev, Appl. Phys. A **83**, 417 (2006)
2. P.V. Kazakevich, A.V. Simakin, G.A. Shafeev, Appl. Surf. Sci. **252**, 4457 (2006)
3. A. Bensaoula, C. Boney, R. Pillai, G.A. Shafeev, A.V. Simakin, D. Starikov, Appl. Phys. A **79**, 973 (2004)
4. S.I. Dolgaev, N.A. Kirichenko, A.V. Simakin, G.A. Shafeev, Appl. Surf. Sci. **253**, 7987 (2007)
5. S.I. Dolgaev, S.V. Lavrishev, A.A. Lyalin, A.V. Simakin, V.V. Voronov, G.A. Shafeev, Appl. Phys. A **73**, 117 (2000)
6. P.E. Dyer, S.D. Jenkins, J. Sidhu, Appl. Phys. Lett. **49**, 453 (1986)
7. N.S. Murthy, R.D. Prabhu, J.J. Martin, L. Zhou, R.L. Headrick, J. Appl. Phys. **100**, 023538 (2006)
8. Peto G, Karacs A, Paszti Z ,Guczi L,Divinyi T, Joob A. Appl Surf Sci 2002;186:7–13
9. Bereznai M, Pelsoczi I, Toth Z, Turzo K, Radnai M, Bor Z, et al. Biomaterials 2003;24:4197–203
10. Chichkov, B. N., Momma, C., Nolte, S., von Alvensleben, F. & Tunnermann, A. Femtosecond, picosecond and nanosecond laser ablation of solids. *Appl. Phys. A Mater. Sci. Process.* **63,** 109–115 (1996).
11. J. E. Sippe, J.F. Young, J.S. Preston, H.M. van Driel, Phys. Rev. B **27**, 1141 (1983)
12. Lloyd, R., Abdolvand, A., Schmidt, M. et al. Appl. Phys. A (2008) 93: 117.
13. Yoann Levy, Relaxation dynamics of femtosecond-laser-induced temperature modulation on the surfaces of metals and semiconductors, Thibault J.-Y. Derrien, Nadezhda M. Bulgakova, Evgeny L. Gurevich, Toma´s Mocek, Applied Surface Science (2015), http://dx.doi.org/10.1016/j.apsusc.2015.10.159
14. Evgeny L. Gurevich, Mechanisms of femtosecond LIPSS formation induced by periodic surface temperature modulation, Applied Surface Science (2015), http://dx.doi.org/10.1016/j.apsusc.2015.09.091
15. George D. Tsibidis, C. Fotakis,1,2 and E. Stratakis, Physical review B **92**, 041405(R) (2015)
16. A. Kruusing, Opt. Lasers Eng. 41 (2004) 307.
17. A. Kruusing, Opt. Lasers Eng. 41 (2004) 329.
18. J. Noack. A. Vogel, IEEE J. Quantum Electron. 35 (1999) 1156.
19. W. Liu, O. Kosareva, I.S. Golubtsov, A. Iwasaki, A. Becker, V.P. Kandidov, S.L. Chin, Appl. Phys., B 76 (2003) 215.

20. A. Vogel, J. Noack, K. Nahen, D. Theisen, S. Busch, U. Parlitz, D.X. Hammer, G.D. Noojin, B.A. Rockwell, R. Bringruger, Appl. Phys., B 68 (1999) 271.
21. Zinger O, Zhao G, Schwartz Z, Simpson J, Wieland M, Landolt D, et al. Differential regulation of osteoblasts by substrate microstructural features. Biomaterials 2005;26:1837–47.
22. Wennerberg A, Albrektsson T, Johansson C, Andersson B. Experimental study of turned and grit-blasted screw-shaped implants with special emphasis on effects of blasting material and surface topography. Biomaterials 1996;17:15–22.
23. Bathomarco R, Solorzano G, Elias C, Prioli R. Atomic force microscopy analysis of different surface treatments of Ti dental implant surfaces. Appl Surf Sci 2004;233:29–34.
24. Gaggl A, Schultes G, Muller W, K ¨ archer H. Scanning electron microscopical ¨ analysis of laser-treated titanium implant surfaces—a comparative study. Biomaterials 2000;21:1067–73.
25. Madore C, Piotrowski O, Landolt D. Through-mask electrochemical micromachining of titanium. J Electrochem Soc 1999;146:2526–32.
26. Stratakis E, Ranellaa A, Farsaria M, Fotakis C. Laser-based micro/nanoengineering for biological applications. Prog Quantum Electron 2009;33: 127–63.
27. Joshua R. Bush, Barada K. Nayak, Lakshmi S. Nair, Mool C. Gupta, Cato T. Laurencin, Improved bio-implant using ultrafast laser induced self-assembled nanotexture in titanium. Journal of Biomedical Materials Research: Applied Biomaterials. Submitted for publication.
28. Wu C, Crouch H, Zhao L, Carey J, Younkin R, Levinson J, et al. Near-unity below-band gap absorption by microstructured silicon. Appl Phys Lett 2001;78:1850–2.
29. Zorba V, Stratakis E, Barberoglou M, Spanakis E, Tzanetakis P, Anastasiadis S, et al. Biomimetic artificial surfaces quantitatively reproduce the water repellency of a lotus leaf. Adv Mater 2008;20:4049–54.
30. Kietzig A, Hatzikiriakos S, Englezos P. Patterned superhydrophobic metallic surfaces. Langmuir 2009;25:4821–7.
31. Baldacchini T, Carey J, Zhou M, Mazur E. Superhydrophobic surfaces prepared by microstructuring of silicon using a femtosecond laser. Langmuir 2006;22:4917–9.
32. Nayak B, Iyengar V, Gupta M. Ultrafast laser textured silicon solar cells. Mater Res Soc Symp Proc 2009;1123:P07–09.
33. Nayak B, Iyengar V and Gupta M, Efficient light trapping in silicon solar cells by ultrafast-laser-induced self-assembled micro/nano structures, Progress in Photovoltaics: Research and Applications. submitted for publication.

34. Richard M, Richard F, Karger A, Carey J, Mazur E. Enhancing near-infrared avalanche photodiode performance by femtosecond laser microstructuring. Appl Opt 2006;45:8825–31.
35. Carey J, Crouch C, Shen M, Mazur E. Visible and near-infrared responsivity of femtosecond-laser microstructured silicon photodiodes. Opt Lett 2005;30: 1773–5.
36. Zorba V, Tzanetakis P, Fotakis C, Spanakis E, Stratakis E, Papazoglou D, et al. Silicon electron emitters fabricated by ultraviolet laser pulses. Appl Phys Lett 2006;88:081103–5.
37. Li J, Xiong D, Wu H, Huang J, Dai J, Tyagi R. Tribological properties of laser surface texturing and molybdenizing Duplex-Treated Ni-Base alloy. Tribol Trans 2010;53:195–202.
38. S. I. Anisimov, B. S. Luk'yanchuk, Selected problems of laser ablation theory, Physic Uspekhi 45 (2002) 293-324.
39. D. Bauerle, Laser processing and chemistry, Springer, 2011.
40. Emmony, D. C.; Howson, R. P.; Willis, L. J. Laser Mirror Damage in Germanium at 10.6 _m. *Appl. Phys. Lett.* **1973**, *23*, 598–600.
41. J. Z. P. Skolski, G. R. B. E. Romer, A. J. Huis in't Veld, V. S. Mitko, J. V. Obona, V. Ocelik1, J. T. M. De Hosson Modeling of Laser Induced Periodic Surface Structures JLMN ***Vol. 5, No. 3, 2010***.
42. R. W. Wood, On a remarkable case of uneven distribution of light in a diffraction grating spectrum, Proc. Phys. Soc. London 18 (1902) 269– 275.
43. V. V. Klimov, Nanoplasmonics, Pan Stanford Publishing, 2011.
44. S. A. Akhmanov, V. I. Emel'yanov, N. I. Koroteev, V. N. Seminogov, Interaction of powerful laser radiation with the surfaces of semiconductors and metals: nonlinear optical effects and nonlinear optical diagnostics, Sov. Phys. Uspekhi 28 (1985) 1084–1124.
45. Taylor, R., Hnatovsky, C. & Simova, E. Applications of femtosecond laser induced self-organized planar nanocracks inside fused silica glass. *Laser Photonics Rev.* **2,** 26–46 (2008).
46. J. Appl. Phys. 106, 104910 (2009); doi: 10.1063/1.3261734
47. E.L. Gurevich, On the influence of surface plasmon-polariton waves on pattern formation upon laser ablation, Appl. Surf. Sci. (2013), http://dx.doi.org/10.1016/j.apsusc.2013.01.103
48. Tsibidis, G. D., Barberoglou, M., Loukakos, P. A., Stratakis, E. & Fotakis, C. Dynamics of ripple formation on silicon surfaces by ultrashort laser pulses in subablation conditions. *Phys. Rev. B* **86,** 115316 (2012).
49. Craig A. Zuhlke ; Troy P. Anderson ; Dennis R. Alexander; Understanding the formation of self-organized micro/nanostructures on metal surfaces from femtosecond laser ablation using stop-motion SEM imaging. Proc. SPIE 8968,

Laser-based Micro- and Nanoprocessing VIII, 89680C (March 6, 2014); doi:10.1117/12.2040348.

50. C.Y. Lin, C.W. Cheng, K.L. Ou, Micro/Nano-Structuring of Medical Stainless Steel using Femtosecond Laser Pulses, Physics Procedia, Volume 39, 2012, Pages 661-668, ISSN 1875-3892.
51. Barada K. Nayak, Mool C. Gupta, Self-organized micro/nano structures in metal surfaces by ultrafast laser irradiation, Optics and Lasers in Engineering, Volume 48, Issue 10, October 2010, Pages 940-949, ISSN 0143-8166.
52. Bonse, J., Höhm, S., Rosenfeld, A. & Krüger, J. Sub-100-nm laser-induced periodic surface structures upon irradiation of titanium by Ti:sapphire femtosecond laser pulses in air. *Appl. Phys. A* **110,** 547–551 (2013).
53. Bonse, J. *et al.* Femtosecond laser-induced periodic surface structures on steel and titanium alloy for tribological applications. *Appl. Phys. A* **117,** 103–110 (2014).
54. G. D. Tsibidis, C. Fotakis and E. Stratakis, From ripples to spikes: A hydrodynamical mechanism to interpret femtosecond laser-induced self-assembled structures Physical Review B **92**, 041405(R) (2015).
55. G. Daminelli, J. Kruger, and W. Kautek, Thin Solid Films 467, 334 (2004).
56. G. Miyaji, K. Miyazaki, K. Zhang, T. Yoshifuji, and J. Fujita, Opt. Express 20, 14848 (2012).
57. C. Albu, A. Dinescu, M. Filipescu, M. Ulmeanu, and M. Zamfirescu, Appl. Surf. Sci. 278, 347 (2013).
58. T. J.-Y. Derrien, R. Koter, J. Krüger, S. Höhm, A. Rosenfeld, and J. Bonse Journal of Applied Physics **116**, 074902 (2014).
59. C. Wang, H. Huo, M. Johnson, M. Shen, and E. Mazur, Nanotechnology **21**, 075304 (2010).
60. S. A. Maier, Plasmonics, Fundamentals and Applications (Springer, 2007).
61. Markovic M I and Rakic A D 1990 Determination of the reflection coefficients of laser light of wavelengths $\lambda \in (0.22\mu\text{m}, 200\mu\text{m})$ from the surface of aluminum using the Lorentz–Drude model *Appl. Opt.* **29** 24.
62. C. Sarpe, J. Kohler, T. Winkler, M. Wollenhaupt, and T. Baumert, New. J. Phys. 14, 075021 (2012).
63. M. Weber, Handbook of Optical Materials (CRC Press, 2003).
64. E. D. Palik, Handbook of Optical Constants of Solids (Academic Press, 1985).
65. Yanyan Huo, Tianqing Jia, Donghai Feng, Shian Zhang, Jukun Liu, Jia Pan, Kan Zhou and Zhenrong Sun, Formation of high spatial frequency ripples in stainless steel irradiated by femtosecond laser pulses in water Laser Phys. 23 (2013) 056101 (7pp).
66. Huang M, Zhao F L, Cheng Y, Xu N S and Xu Z Z 2009 ACS Nano **3** 4062–70
67. Vorobyev A, Makin V and Guo C L 2007 Periodic ordering of random surface nanostructures induced by femtosecond laser pulses on metals *J. Appl. Phys.* **101** 034903.
68. Shuangshuang Hou, Yanyan Huo, Pingxin Xiong, Yi Zhang, Shian Zhang, Tianqing Jia, Zhenrong Sun, Jianrong Qiu and Zhizhan Xu, Formation of long- and short-periodic nanoripples on stainless steel irradiated by femtosecond laser pulses, J. Phys. D: Appl. Phys. **44** (2011) 505401 (7pp).

69. A. E. Siegman and P. M. Fauchet, IEEE J. Quantum Electron. **QE-22**, 1384 (1986).
70. R. N. Wenzel, Resistance of solid surface to wetting by water, *Industrial & Engineering Chemistry*, 1936, **28**, 988-994.
71. A. B. D. Cassie and S. Baxter, Wettability of porous surfaces, *Transactions of the Faraday Society*, 1944, **40**, 546-551.
72. X. J. Feng and L. Jiang, Design and Creation of Superwetting/Antiwetting Surfaces, *Advanced Materials*, 2006, **18**, 3063-3078.
73. L. Feng, Y. Zhang, J. Xi, Y. Zhu, N. Wang, F. Xia and L. Jiang, Petal effect: A superhydrophobic state with high adhesive force, *Langmuir*, 2008, **24**, 4114-4119.
74. C. Dorrer and J. Rühe, Some thoughts on superhydrophobic wetting, *Soft Matter*, 2009, **5**, 51.
75. M. Nosonovsky and B. Bhushan, Biomimetic Superhydrophobic Surfaces: Multiscale Approach, *Nano Letters*, 2007, **7**, 2633-2637.
76. P. G. de Gennes, F. Brochard-Wyart and D. Quéré, *Capillarity and wetting phenomena: drops, bubbles, pearls, waves*, 2004.
77. P. B. Johnson and R. W. Christy Optical Constants of the Noble Metals Phys. Rev. B **6**, 4370.
78. Neil W. Ashcroft, N. David Mermin, Solid State Physics (Cengage Learning, 2011).
79. Michael P. Marder, Condensed Matter Physics (Willey, 2000).
80. Charles Kittel, Introduction to Solid State Physics (Willey, 1996).
81. T. Morimoto, Y. Sanada and H. Tomonaga, Wet chemical functional coatings for automotive glasses and cathode ray tubes, *Thin Solid Films*, 2001, **392**, 214-222.
82. L. Carrino, G. Moroni and W. Polini, Cold plasma treatment of polypropylene surface: a study on wettability and adhesion, *Journal of Materials Processing Technology*, 2002, **121**, 373-382.
83. K. Bobzin, N. Bagcivan, N. Goebbels, K. Yilmaz, B. R. Hoehn, K. Michaelis and M. Hochmann, Lubricated PVD CrAlN and WC/C coatings for automotive applications, *Surface & Coatings Technology*, 2009, **204**, 1097-1101.
84. J. Genzer and K. Efimenko, Recent developments in superhydrophobic surfaces and their relevance to marine fouling: a review, *Biofouling*, 2006, **22**, 339-360.
85. X. Wang, L. Zhi and K. Mullen, Transparent, Conductive Graphene Electrodes for Dye-Sensitized Solar Cells, *Nano Letters*, 2007, **8**, 323-327.
86. W. Barthlott and C. Neinhuis, Purity of the sacred lotus, or escape from contamination in biological surfaces, *Planta*, 1997, **202**, 1-8.
87. L. Feng, S. Li, Y. Li, H. Li, L. Zhang, J. Zhai, Y. Song, B. Liu, L. Jiang and D. Zhu, Super-hydrophobic surfaces: from natural to artificial, *Advanced Materials*, 2002, **14**, 1857-1860.
88. X. Feng, L. Feng, M. Jin, J. Zhai, L. Jiang and D. Zhu, Reversible super-hydrophobicity to super-hydrophilicity transition of aligned ZnO nanorod films, *Journal of the American Chemical Society*, 2004, **126**, 62-63.

89. G. B. Sigal, M. Mrksich and G. M. Whitesides, Effect of Surface Wettability on the Adsorption of Proteins and Detergents, *Journal of the American Chemical Society*, 1998, **120**, 3464-3473.
90. Daniel Puerto *et al* 2016 *Nanotechnology* **27** 265602.
91. Jincheng Wang and Chunlei Guo, Journal of Applied Physics **100**, 023511 (2006).
92. S. Schreck, K.-H. Zum Gahr, Laser-assisted structuring of ceramic and steel surfaces for improving tribological properties, Applied Surface Science, Volume 247, Issues 1–4, 15 July 2005.
93. J. Reif, F. Costache, M. Henyk, S.V. Pandelov, Ripples revisited: non-classicalmorphology at the bottom of femtosecond laser ablation craters intransparent dielectrics, Appl. Surf. Sci. 197–198 (2002) 891–895, http://dx.doi.org/10.1016/S0169-4332(02)00450-6, pii: S0169433202004506.
94. J. Bonse, J. Krüger, S. Höhm, A. Rosenfeld, Femtosecond laser-induced periodic surface structures, J. Laser Appl. 24 (4) (2012), http://dx.doi.org/10.2351/1.4712658.
95. G.D. Tsibidis, E. Skoulas, A. Papadopoulos, E. Stratakis, Convection roll-driven generation of supra-wavelength periodic surface structures on dielectrics upon irradiation with femtosecond pulsed lasers, Physical Review B, 94 (2016) 081305.